

The Pennsylvania State University
The Graduate School
Department of Engineering Science and Mechanics

MICROELECTROMECHANICAL SYSTEMS (MEMS) SENSORS
BASED ON LEAD ZIRCONATE TITANATE (PZT) FILMS

A Thesis in
Engineering Science and Mechanics

by
Li-Peng Wang

© 2001 Li-Peng Wang

Submitted in Partial Fulfillment
of the Requirements
for the Degree of

Doctor of Philosophy

May 2001

UMI Number: 3014720

UMI[®]

UMI Microform 3014720

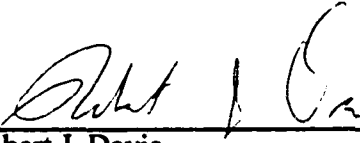
Copyright 2001 by Bell & Howell Information and Learning Company.

All rights reserved. This microform edition is protected against
unauthorized copying under Title 17, United States Code.

Bell & Howell Information and Learning Company
300 North Zeeb Road
P.O. Box 1346
Ann Arbor, MI 48106-1346

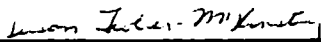
We approve the thesis of Li-Peng Wang.

Date of Signature



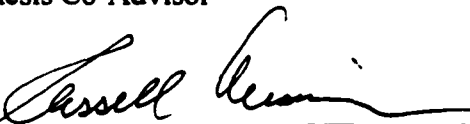
Robert J. Davis
Research Associate of Engineering Science
and Mechanics
Thesis Co-Advisor
Co-Chair of Committee

1 March 2001



Susan Trolier-McKinstry
Associate Professor of Ceramic Science and
Engineering
Thesis Co-Advisor

March 1, 2001



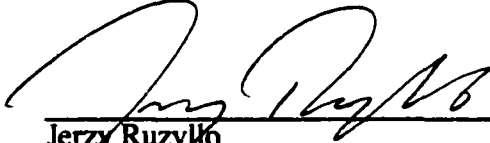
Russell Messier
Professor of Engineering Science and
Mechanics
Co-Chair of Committee

March 1, 2001



Osama O. Awadelkarim
Professor of Engineering Science and
Mechanics

March 1, 2001



Jerzy Ruzylko
Professor of Electrical Engineering

March 1, 2001



Richard P. McNitt
Professor of Engineering Science and
Mechanics
Head of Department of Engineering Science
and Mechanics

March 1, 2001

ABSTRACT

In this thesis, modeling, fabrication and testing of microelectromechanical systems (MEMS) accelerometers based on piezoelectric lead zirconate titanate (PZT) films are investigated. Three different types of structures, a cantilever beam, a trampoline, and an annular diaphragm, were studied. The resulting accelerometers are high-performance, miniature, mass-production-compatible, and potentially circuitry-integratable piezoelectric PZT MEMS devices.

Theoretical models of the cantilever-beam and trampoline accelerometers were derived via structural dynamics and the constitutive equations of piezoelectricity. The time-dependent transverse vibration equations, mode shapes, resonant frequencies, and sensitivities of the accelerometers were calculated through the models. Optimization of the silicon and PZT thickness was achieved considering the effects of structural dynamics, material properties, and manufacturability for different accelerometer specifications.

This work is the first demonstration of the fabrication of bulk-micromachined accelerometers combining a deep-trench reactive ion etching (DRIE) release strategy and thick piezoelectric PZT films deposited using a sol-gel method. Processing challenges which were overcome included materials compatibility, metallization, processing of thick layers, double-side processing, deep-trench silicon etching, post-etch cleaning and process integration. In addition, the processed PZT films were characterized by

dielectric, ferroelectric (polarization electric-field hysteresis), and piezoelectric measurements and no adverse effect of the processing on the properties was found.

Dynamic frequency response and impedance resonance measurements were performed to ascertain the performance of the MEMS accelerometers. The results show high sensitivities and broad usable frequency ranges for the piezoelectric PZT MEMS accelerometers; the sensitivities range from 0.1 to 7.6 pC/g for resonant frequencies ranging from 44.3 kHz to 3.7 kHz. The sensitivities were compared to theoretical values and a reasonable agreement (~ 36% difference) was obtained.

TABLE OF CONTENTS

LIST OF FIGURES.....	viii
LIST OF TABLES.....	xiii
ACKNOWLEDGMENTS	xiv
Chapter 1 Introduction	1
1.1 Overview.....	1
1.2 Review of Previous Work.....	2
1.2.1 Piezoelectric Films for MEMS Applications	2
1.2.2 MEMS Accelerometers	4
1.3 Technical and Theoretical Background	10
1.3.1 Silicon Micromachining for Accelerometers.....	10
1.3.2 Ferroelectric Material Systems.....	15
1.3.3 Perovskite Structure of Lead Zirconate Titanate	17
1.3.4 Piezoelectricity	20
1.3.5 Interface Circuit.....	21
1.4 Research Objectives.....	24
Chapter 2 Processing and Characterization of PZT Films For MEMS Applications ..	26
2.1 Introduction.....	26
2.2 PZT Film Patterning Using Microlithography Processes.....	27
2.2.1 Lithography.....	28
2.2.2 Patterning of PZT Thick Films.....	28
2.2.3 Residue Analysis	32
2.2.4 Two-step Etching Process	32
2.3 Characterization of Processed PZT Films	37
2.3.1 Film Thickness and Uniformity.....	37
2.3.2 Measurement of Dielectric Properties	39
2.3.3 Measurement of Ferroelectric Properties.....	40
2.3.4 Measurement of the Transverse Piezoelectric Constant.....	42
Chapter 3 MEMS Accelerometer Design I: Cantilever-Beam Structure	44

3.1 Device Design and Model.....	44
3.1.1 Device Structure and Design	44
3.1.2 Derivation of Structure Dynamics.....	48
3.1.3 Analytical Solution of Charge Sensitivity	54
3.1.4 Optimization of PZT and Silicon Beam Thickness.....	58
3.1.5 Sensitivity and Bandwidth.....	63
3.2 Processing Development.....	63
3.2.1 Overview	63
3.2.2 Front-to-backside Alignment.....	64
3.2.3 Metallization.....	65
3.2.4 Thick-resist Photolithography	66
3.2.5 Deep Reactive Ion Etching	69
3.2.6 Processing Procedures	70
Chapter 4 MEMS Accelerometer Design II: Trampoline and Diaphragm Structures	77
4.1 Device Design and Modeling of Trampoline-type Accelerometers	77
4.1.1 Device Structure and Design	77
4.1.2 Derivation of Structure Dynamics.....	80
4.1.3 Analytical Solution of Charge Sensitivity.....	85
4.2 Device Design and Finite Element Analysis (FEA) Model of Diaphragm- type Accelerometers	87
4.2.1 Device Structure and Design	87
4.2.2 FEA Simulation using ANSYS software.....	88
4.3 Process Development.....	90
4.3.1 Photomask Design	91
4.3.2 Metallization.....	96
4.3.3 Backside Processing	98
4.3.4 DRIE.....	99
4.3.5 Processing Procedures	102
Chapter 5 Characterization of MEMS Accelerometers	109
5.1 Frequency Response Measurement.....	109
5.1.1 Introduction	109
5.1.2 Equipment Setup and Measurement Procedure.....	110
5.1.3 Tested Results.....	114
5.2 Impedance Resonance Measurements	117
5.3 Comparison of Theoretical and Measured Results	118
5.3.1 Comparison of Analytical and FEA Results.....	118
5.3.2 Comparison of Measured and FEA Results	120
Chapter 6 Conclusions and Future Work.....	125

6.1 Conclusions	125
.....	
6.1.1 Design and Modeling	125
6.1.2 Fabrication	126
6.1.3 Measurement and Results	127
6.2 Future Work	128
BIBLIOGRAPHY	131

LIST OF FIGURES

<i>Figure 1.1:</i> Cross section of the accelerometer designed by Chen et al. [19].....	6
<i>Figure 1.2:</i> Cross section of a surface micromachined accelerometer fabricated by DeVoe and Pisano [21].....	7
<i>Figure 1.3:</i> (a) and (c) show the electrode configurations for sensing a vertical-direction acceleration; (b) and (d) show the electrode configurations for sensing horizontal-direction accelerations [22]	7
<i>Figure 1.4:</i> Dimensions of the accelerometer reported by Beeby et al. [28]; inertial mass 4mm^2 ; beam $975\ \mu\text{m}$ long, $750\ \mu\text{m}$ wide; PZT $900\ \mu\text{m}$ long, $660\ \mu\text{m}$ wide; top electrode $800\ \mu\text{m}$ long, $420\ \mu\text{m}$ wide.....	9
<i>Figure 1.5:</i> SEM showing that the top electrodes are continuous over the beams [28].....	10
<i>Figure 1.6:</i> Planes occurring at convex corners during KOH etching of Si [41].....	13
<i>Figure 1.7:</i> Etched profiles of isotropic and anisotropic etching.....	15
<i>Figure 1.8:</i> Polarization electric-field (P-E) hysteresis loop of a ferroelectric material [51].....	16
<i>Figure 1.9:</i> Perovskite structure of PZT; the corner atoms are Pb^{2+} , the face centered atoms are O^{2-} , and the central atom is either Zr^{4+} or Ti^{4+} [52].....	17
<i>Figure 1.10:</i> Phase diagram of PZT [53].....	19
<i>Figure 1.11:</i> Coupling coefficient and permittivity values of PZT compositions [53]; k is coupling coefficient and ϵ_r is the relative permittivity	19
<i>Figure 1.12:</i> Schematics of d_{33} and d_{31} operation modes; the dashed areas show that changes in dimensions due to an applied stress lead to induced polarizations [53].....	21
<i>Figure 1.13:</i> Electrical circuit configuration of a piezoelectric film connected to a charge amplifier.....	23

Figure 2.1: General lithography and etching processes.....	29
Figure 2.2: SEM micrograph showing residue in the etched area after etching a 4 μm PZT film in 0.34%HF:5%HCl:94.66%H_2O for 40 minutes.....	30
Figure 2.3: A 50 by 50μm pixel can not be well patterned using HCl etching solution; the photoresist was stripped.....	31
Figure 2.4: XRD showing residues consisting of metal fluorides; this sample was etched with an HF-based solution only.....	34
Figure 2.5: XRD pattern showing no residue on a sample which was incompletely etched in HF and then quickly dipped in HCl.....	34
Figure 2.6: SEM micrograph showing well patterned 2 μm PZT films and a clean etched surface resulting from two-step etching	35
Figure 2.7: Etched profile of a 2 μm PZT film from lateral view	36
Figure 2.8: Surface etched by two-step etch examined by XRD; no residue was found. Pt is the bottom electrode	36
Figure 2.9: Uniformities of PZT films across 4" wafers	38
Figure 2.10: Permittivity and dielectric loss of etched 6 μm PZT films across a 4' wafer	39
Figure 2.11: Average P-E hysteresis loop of a processed 5.95 μm PZT film across a 4" wafer.....	41
Figure 2.12: Coercive field and remanent polarization of a processed 5.95 μm PZT film.....	41
Figure 2.13: The pressure jig for d_{31} measurement [77]	43
Figure 2.14: Equipment setup for measuring the transverse piezoelectric constant [78].....	43
Figure 3.1: Transverse sensitivity cancellation in the x direction	45
Figure 3.2: Schematic of PZT MEMS accelerometer; it consists of four cantilever beams with a proof mass at the end	46
Figure 3.3: Charge cancellation in the z direction.....	47

Figure 3.4: Boundary condition of a cantilever beam with a proof mass on the free end; M and V are the bending moment and shear force generated from the proof mass	49
Figure 3.5: Eigenvalues corresponding to the first and second modes of a cantilever beam (1.27mm in length) with a proof mass at the free end.....	53
Figure 3.6: Mode shape of a cantilever beam (1.27mm in length) with a proof mass on the free end.....	54
Figure 3.7: Stress distribution of the PZT and silicon composite beam along the y axis.....	56
Figure 3.8: The distribution of the normal stress in the middle of the PZT layer for a cantilever beam beam (1.27mm in length) with a proof mass on the free end.....	57
Figure 3.9: Thickness dependence of piezoelectric constant of PZT film [68].....	59
Figure 3.10: Optimized PZT thickness for a 50 thick silicon beam (a) without (b) with considering the thickness-dependent piezoelectric constant	60
Figure 3.11: Sensitivity of MEMS accelerometers for different thickness of silicon layers; the thickness of the PZT layer is fixed at 6 μm	62
Figure 3.12: The mechanical jig for the front-to-backside alignment	65
Figure 3.13: Spin curve of AZ4620 photoresist	68
Figure 3.14: Fabrication Process flow of PZT MEMS accelerometers.....	74
Figure 3.15: Frontside process: patterned top electrode/PZT and bottom electrode... 	75
Figure 3.16: SEM graph showing one of the cantilever beam and proof mass of the accelerometer; the tapered profile resulted from heating and loading effects.....	76
Figure 4.1: Schematic of a trampoline-type accelerometer	78
Figure 4.2: Gain-bandwidth (GWB) of an ASIC amplifier.....	80
Figure 4.3: Boundary conditions for the trampoline-type beam.....	83
Figure 4.4: Eigenvalues corresponding to the first and second modes of the trampoline structure	84

Figure 4.5: First and second mode shapes of one arm of the trampoline structure; beam length is 1.1 mm	85
Figure 4.6: The distribution of the normal stress in the middle of the PZT layer under one g acceleration; beam length is 1.1 mm.....	86
Figure 4.7: Schematic showing half of the diaphragm accelerometer.....	87
Figure 4.8: Stress distribution of a diaphragm accelerometer along the radial direction; the solid line is radial stress and the dashed line is tangential stress....	89
Figure 4.9: Top view of the diaphragm accelerometer showing the definitions of the dimensions	89
Figure 4.10: The second photomask set includes trampoline-type, diaphragm-type accelerometers and testing patterns	91
Figure 4.11: SEM showing contact of top and bottom electrodes causing an electrical short.....	92
Figure 4.12: Etched through area of the trampoline design.....	93
Figure 4.13: The accuracy of front-to-backside alignment using the mechanical jig was measured from this pattern; the misalignment is 9.5 μm in the x direction and 17.5 μm in the z direction, typical for this jig.....	95
Figure 4.14: The improved metallization of the top electrodes for (a) diaphragm type and (b) trampoline type accelerometers	97
Figure 4.15: The improved backside processing including the well patterned silicon oxide and thick photoresist layers.....	98
Figure 4.16: Etched profiles of the proof mass for first (a) and second-generation (b) accelerometers; the proof mass in (b) was cut from its supporting trampoline structure	100
Figure 4.17: Etching rate uniformity over 4" wafers for STS and PTI etchers; the higher etching rate results in a higher non-uniformity.....	102
Figure 4.18: Fabrication process flow for second-generation MEMS accelerometers	106
Figure 4.19: A diaphragm-type accelerometer compared to a penny after finishing the processing steps	108

Figure 5.1: Schematic of the equipment setup for the frequency response measurement	111
Figure 5.2: Aluminum holder designed for frequency response measurement of the MEMS accelerometer sensitivity	112
Figure 5.3: Frequency response of the diaphragm-type MEMS accelerometer; the resonant frequency is 3.7 kHz and sensitivity is 7.6 pC/g.....	115
Figure 5.4: Frequency response of the diaphragm type MEMS accelerometer; the resonant frequency is 22.06 kHz and sensitivity is 0.47 pC/g.....	115
Figure 5.5: Frequency response of the trampoline type MEMS accelerometer; the resonant frequency is 44.3 kHz and sensitivity is 0.10 pC/g.....	116
Figure 5.6: Sensitivity vs. resonant frequency for each type of MEMS accelerometer	116
Figure 5.7: The impedance measurement of the diaphragm type MEMS accelerometer showing the resonant peak at 12.27 kHz; Z is the impedance and θ is the phase.....	117
Figure 5.8: The average tested sensitivity is 36.3% below the FEA value.....	122
Figure 5.9: Etched profile of the proof mass (diaphragm type) showing an imperfect vertical wall	122
Figure 5.10: The ratio of the measured sensitivities to the theoretical ones plotted as a function of the silicon thickness; the PZT thickness is 5.6 μm	124
Figure 6.1: Interlayer electrodes for a high-sensitivity accelerometer design.....	130

LIST OF TABLES

<i>Table 1.1: Properties of piezoelectrics [5]</i>	3
<i>Table 2.1: Comparison of different etching recipes for PZT thick films.....</i>	31
<i>Table 2.2: Two-step etching processes for thick PZT film patterning.....</i>	35
<i>Table 3.1: Dimension of cantilever-beam accelerometers.....</i>	47
<i>Table 3.2: AZ4620 photolithography steps.....</i>	68
<i>Table 4.1: Dimensions of the trampoline-type accelerometers.....</i>	79
<i>Table 4.2: Dimensions of diaphragm accelerometers.....</i>	90
<i>Table 5.1: Comparison of analytic and FEA results</i>	119
<i>Table 5.2: Comparison of FEA and measured results</i>	120

ACKNOWLEDGMENTS

I would like to express my appreciation to Dr. Robert J. Davis for the invaluable support, guidance, and advice during my study. He also opened a new door for me into the MEMS world.

I am grateful to Dr. Susan Trolier-McKinstry for the invaluable guidance and advice on this thesis, and for helping me get through the toughest time of my study.

I would like to thank Dr. Russell Messier, Dr. Osama O. Awadelkarim, and Dr. Jerzy Ruzyllo for their advice and suggestions on this thesis.

I would like to thank Yu Wang for his valuable discussions during the research and his cooperation on the accelerometer project during the first year. I am grateful to Rich Wolf for preparing the PZT films. I also thank my colleagues, Kuo-Liang Chen, Hong Zhu, Handong Li and Joe Cuiffi for their help in different ways. I am also grateful to the staff at EMPRL for their help in the experiment.

I thank the Office of Naval Research (ONR) and National Institute of Standards and Technology (NIST) for supporting this research. I also thank Wilcoxon Research for their cooperation in the PZT accelerometer project. I thank Kan Deng for his valuable discussions about the accelerometer designs. I thank Cornell Nanofabrication Facility (CNF) for providing the DRIE etcher.

Finally, I am deeply grateful to my parents, my wife, Chi-Yueh, and my son, Ryan. Without their entire support and encouragement, this work would not have been done.

Chapter 1

Introduction

1.1 Overview

Microelectromechanical systems (MEMS), a technology which permits the integration of micromachined mechanical structures with integrated circuits (IC), has been a growing area of research in the last two decades [1,2]. MEMS have a wide range of applications including automotive, industrial, biomedical, and information processing [3,4]. Silicon micromachining, taking advantages of well-established processes and materials in microelectronics, is commonly used to fabricate mechanical microstructures. As a result, in the early work, the materials used in MEMS area were limited to those used in microelectronics. In particular, materials with fast diffusing ions were forbidden because of contamination and compatibility issues.

There are wide varieties of functional materials that did not fit within the initial set of materials explored for MEMS. One example of this is ferroelectric lead zirconate titanate (PZT) films, which are attractive because of their high sensitivity in sensor applications and high force output in actuator applications. In the beginning, the usage of PZT films in MEMS was delayed by integration difficulties [5]. During recent years, much progress in integration has been made. However, this was driven mainly by ferroelectric random access memory (FRAM) applications [6]. In part as a result of that

work, PZT films are now integrated with silicon micromachining techniques to fabricate piezoelectric MEMS devices [5]. In this chapter, the previous work on piezoelectric materials and piezoelectric MEMS accelerometers will be reviewed first, followed with an overview of the techniques and theoretical background applied in this thesis. Finally, the research objectives will be described.

1.2 Review of Previous Work

1.2.1 Piezoelectric Films for MEMS Applications

Of the available piezoelectric materials, the three most widely studied piezoelectric films for MEMS have been zinc oxide (ZnO), aluminum nitride (AlN), and PZT [7]. The main considerations for piezoelectric materials to be used in MEMS are their processing compatibility with silicon and their piezoelectric response. The properties of these three materials are compared in *Table 1.1*.

ZnO was the first piezoelectric film used in commercialized TV surface-acoustic-wave (SAW) filters because of its high piezoelectric coefficient (compared to non-ceramic materials) and simplicity of preparation [8]. AlN, another promising piezoelectric material, has a piezoelectric coefficient that is lower than ZnO, but its high acoustic velocity makes it attractive for high frequency devices (in the GHz range). In addition, its stability at high temperatures and humidities make it compatible with silicon

and GaAs monolithic processing, in which diffusion, annealing, and implantation are required.

PZT was first developed in bulk ceramics and was primarily used in sensor and actuator applications. During the past decade, the fabrication and characterization of PZT films have been investigated by many researchers [7]. Its high electromechanical coupling and piezoelectric constant, which are an order of magnitude larger than ZnO and AlN, have drawn great attention for MEMS sensor and actuator applications. MEMS devices based on PZT films, such as force sensors [9], pressure sensors [10], accelerometers [11], micropositioning actuators [12], micromotors [13], and micropumps [14], can be found in the literature.

Table 1.1: Properties of piezoelectrics [5]

	ZnO	AlN	PZT
Form	single crystal	single crystal	polycrystalline film
piezoelectric constant: d_{33} (pC/N)	12	3.9	117
Force, current response: $e_{31, r}$ (C/m ²)	-0.7	-1.0	-12
coupling coefficient: k^2 (%)	6	11	19

1.2.2 MEMS Accelerometers

Accelerometers have been used in many fields, including for activation of automotive safety systems (airbags, electronic suspension), for machine and vibration monitoring, and in biomedical applications for activity monitoring. Micromachined accelerometers have the second largest yearly sales (after pressure sensors) among all MEMS devices, mainly driven by demand from the automotive industry, because of their low cost, small size, and broad frequency response [3].

Three sensing mechanisms, piezoresistive, capacitive, and piezoelectric are commonly utilized for MEMS accelerometers. Each one has limitations and advantages [15] and there are no universal guidelines for comparison. In general, piezoresistive accelerometers have advantages in simplicity of fabrication and good compatibility (or even potential integration) with IC processing; therefore, the first micromachined [16] and commercialized accelerometers [17] were of the piezoresistive type. However, their small overall sensitivity (typically around 1-2 mV/g in the 20-50g range) and large temperature dependence are drawbacks. Capacitive accelerometers have advantages of high sensitivity, low temperature dependence, and good DC response; however, they are easily influenced by electromagnetic interference (EMI) because of their high impedance at the sense node. Many micromachined piezoresistive and capacitive accelerometers, having different designs for different frequency ranges and applications, are available in the literature [15,18].

Compared to piezoresistive and capacitive accelerometers, there have been few reports of micromachined piezoelectric accelerometers. ZnO and PZT films are the two

primary materials used in bulk- or surface-micromachined MEMS accelerometers. In 1982, Chen et al. [19] fabricated a silicon bulk-micromachined piezoelectric accelerometer with a cantilever-beam structure using a ZnO film as the sensing material. The cantilever beam was formed by anisotropic etching of the silicon using an aqueous solution of ethylenediamine and pyrocatechol (EDP). The piezoelectric charge generated by acceleration was coupled to the gate of a p-channel MOS transistor. In order to get a flat, near dc response, the ZnO film was isolated within insulating SiO₂ layers. The cross section of the accelerometer is shown in *Figure 1.1*. A voltage sensitivity of 47 $\mu\text{V/g}$ was obtained. In 1984, Chen and Muller [20] redesigned their accelerometer with a huge silicon proof mass, which was 20 times the beam mass, on the tip of a silicon cantilever beam to improve the sensitivity to 5 mV/g. The resonant frequency of the structure was 8.4 kHz. In 1997, DeVoe and Pisano [21] fabricated a ZnO accelerometer by surface-micromachining techniques, using polysilicon as the structural material and silicon oxide as the sacrificial material (see *Figure 1.2*). However, a low sensitivity of 0.21 fC/g was obtained because of the low piezoelectric constant of the ZnO film and the small mass provided by the cantilever structure. In 1999, Reus et al. [22] also fabricated a bulk-micromachined ZnO accelerometer based on their previous design [23], which had a seismic mass in a two-beam structure. KOH was used as the anisotropic etching solution to form the structure. Both vertical- and horizontal-direction accelerations were measured using this structure; *Figure 1.3* shows the structure and the sensing principles. A vertical-direction sensitivity of 0.1pC/g was measured and a resonant frequency of 4.5

kHz was calculated, while the horizontal-direction sensitivity was 100 times smaller than the vertical-direction sensitivity.

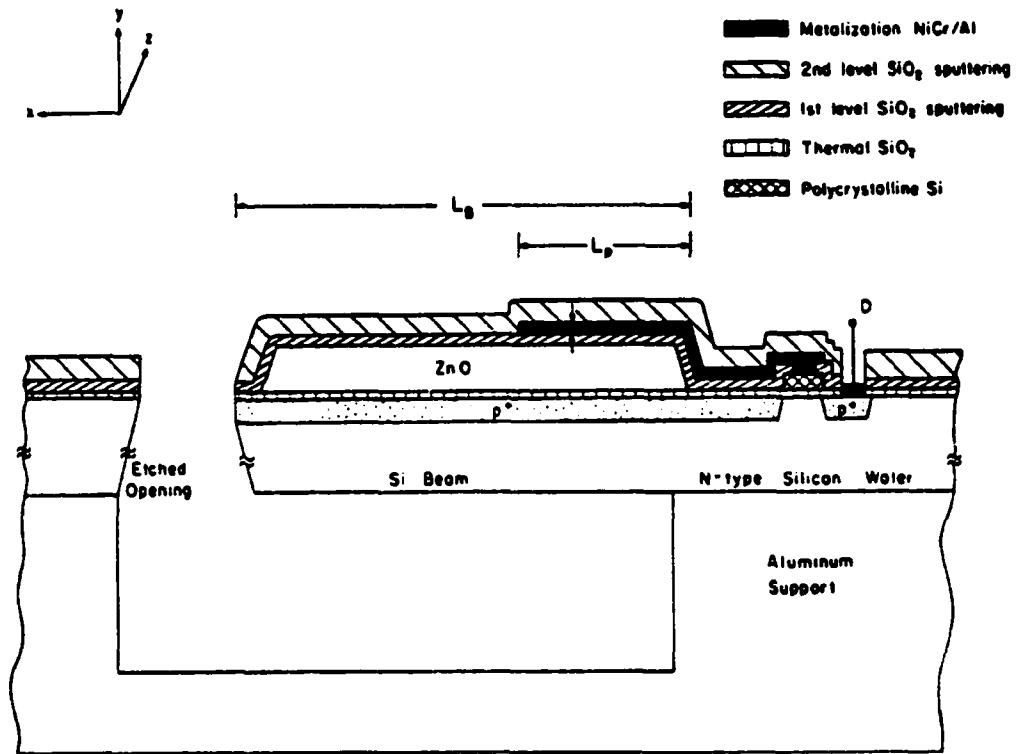


Figure 1.1: Cross section of the accelerometer designed by Chen et al. [19]

parameter	calculated	measured
L (length)	*	1000 μm
b (width)	*	50 μm
t_{Si}	*	2.1 μm
t_{ZnO}	*	0.5 μm
d_{31}	-5.0pC/N (bulk)	-2.3pC/N
ω_0 (res. freq.)	3.9kHz	3.3kHz
m (beam mass)	0.30 μgrams	*

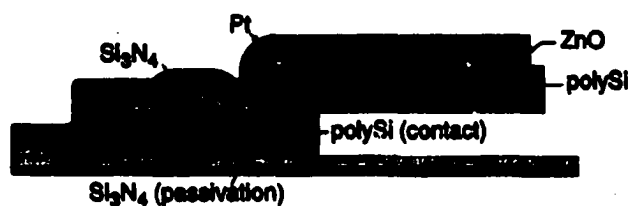


Figure 1.2: Cross section of a surface micromachined accelerometer fabricated by DeVoe and Pisano [21]

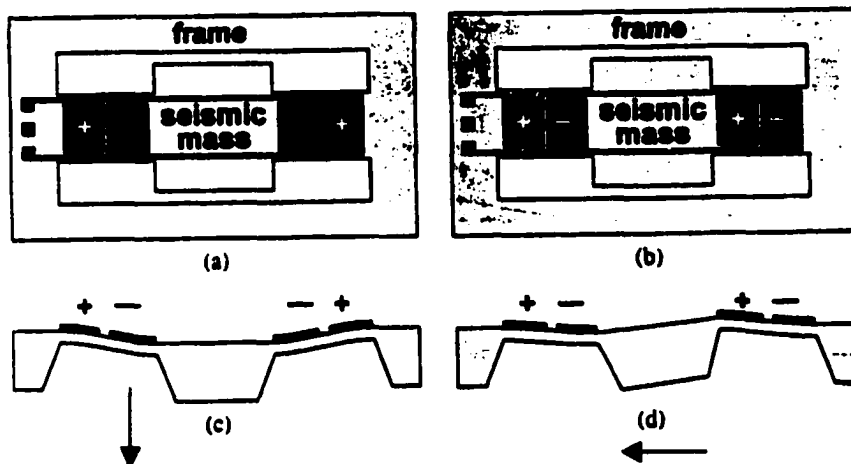


Figure 1.3: (a) and (c) show the electrode configurations for sensing a vertical-direction acceleration; (b) and (d) show the electrode configurations for sensing horizontal-direction accelerations [22]

In 1996, Nemirovsky et al. [24] designed a PZT thin-film piezoelectric accelerometer with a calculated sensitivity of 320 mV/g. However, it has not been fabricated. The first surface-micromachined PZT accelerometer with a cantilever-beam structure was fabricated in 1997 in Polla's group at the University of Minnesota [25]. However, a dynamic frequency response measurement, and therefore, sensitivity, was not available in that reference. In addition, surface micromachining limits the thickness of microstructures; as a result, the sensitivity is limited. In 1999, bulk-micromachined PZT accelerometers were fabricated and tested by Eichner et al. [26]. They used a two-step electrochemical etch-stop in a KOH solution to define the seismic mass and two silicon beams as the sensing structures, which is the same structure as in reference [22]. An average sensitivity of 0.1 mV/g was measured and the calculated resonant frequency was 13 kHz.

Recently, Beeby et al. fabricated a bulk micromachined accelerometer using screen-printed PZT thick films [27,28]. The sensing structure and its dimensions are shown in *Figure 1.4*. The reported sensitivity of 16 pC/g is suspect, since there are fundamental errors in the accelerometer design and the reported results are not self-consistent. First, the stresses on each beam are of opposite signs for the area near the frame and the area near the inertial mass (see also reference 22 and 26). However, their electrodes are continuous over the beam (see *Figure 1.5*); therefore, the charge output should be completely cancelled. Second, the inertial mass should be 4.83 mg instead of the reported 17 mg according to their dimensions, 4 mm² area and 525 μm thick (silicon density is 2.3 g/cm³). Third, the reported voltage sensitivity, 100 μV/g, is not consistent

with the charge sensitivity, 16pC/g, for a sensor capacitance of 360 pF. These factors, coupled with the low piezoelectric coefficients of their thick film ($d_{31} = -33$ pC/N) and the small reported Young's modulus (20 GPa), make the high reported sensitivity unlikely.

The previous reported bulk micromachined accelerometers were all fabricated by wet processing of the silicon using crystal-orientation-dependent anisotropic etching (KOH, EDP, or TMAH). However, they have some drawbacks, which will be discussed in the silicon micromachining section 1.3.1. Therefore, a new approach of fabricating bulk micromachined accelerometers combining a deep-trench reactive ion etching (DRIE) technique and high-performance piezoelectric PZT films will be investigated in this thesis.

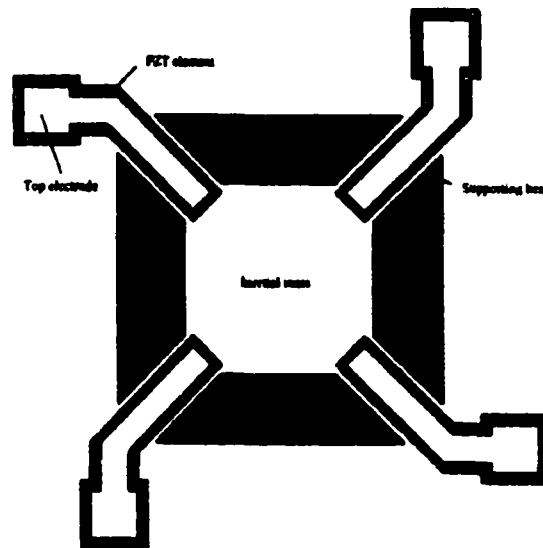


Figure 1.4: Dimensions of the accelerometer reported by Beeby et al. [28]; inertial mass 4mm^2 ; beam $975\ \mu\text{m}$ long, $750\ \mu\text{m}$ wide; PZT $900\ \mu\text{m}$ long, $660\ \mu\text{m}$ wide; top electrode $800\ \mu\text{m}$ long, $420\ \mu\text{m}$ wide



Figure 1.5: SEM showing that the top electrodes are continuous over the beams [28]

1.3 Technical and Theoretical Background

1.3.1 Silicon Micromachining for Accelerometers

Generally, silicon micromachining can be divided into two categories: bulk and surface micromachining. In bulk micromachining, the desired micro-structures are shaped out of the bulk silicon wafer by etching away selected portions of the substrate. The vertical dimension of structures can be as large as the substrate thickness (400 to 600

μm). In surface micromachining, thin film materials are deposited on the wafer surface and microstructures are formed by selectively removing the underlying sacrificial layers. Hence, the vertical dimension is limited by the film thickness. For example, chemical vapor deposited (CVD) polysilicon, the most common structural material for surface micromachining, cannot be made more than $5 \mu\text{m}$ thick [7]. Therefore, the dimensions of surface and bulk micromachining generally differ by two orders of magnitude. Each one has its own advantages and disadvantages depending on the application [29].

For inertial sensors, the minimum detectable signal is limited by Brownian noise [30], which is described in Eq. 1.1:

$$a_{\min} = \sqrt{4k_B T \omega_0 / m_i Q} \quad (1.1)$$

where a_{\min} is the minimum detectable signal when the signal-to-noise ratio (SNR) is unity; k_B is Boltzmann constant; T is the absolute temperature; ω_0 is the resonant frequency of the sensing structure; m_i is the effective sensor mass; and Q is the quality factor. If the minimum detectable signal is $30 \mu\text{g}$ at 100 Hz with a SNR of 4, the minimum m_i is $0.3 \mu\text{gram}$, which is not small for MEMS devices. Therefore, bulk micromachining is preferred in this work, since it can produce a larger mass than surface micromachining. Thus, the technical background for bulk micromachining will be introduced in the following paragraphs.

One of the key techniques in bulk micromachining is silicon etching. Wet and dry etching techniques are two main categories; they are distinguished by the phase of the reactants: liquid and gas phase, respectively. Etching can also be categorized as isotropic or anisotropic, both in wet and dry etching (see *Figure 1.7*). Isotropic etching causes the same etch rate in all directions. As a result, an undercut profile will be found at the mask edge. In contrast, anisotropic etching involves higher etch rates in some directions over others.

A common silicon isotropic etchant is the mixture of hydrofluoric acid (HF), nitric acid (HNO₃), and acetic acid (CH₃COOH) [31,32]. However, better control of etched profiles is always of interest in making useful microstructures in MEMS applications. A wide variety of etchant systems have been studied for anisotropic etching of silicon [33]; potassium hydroxide (KOH) [34,35] and ethylenediamine-pyrocatechol (EDP) [36,37] are the most commonly studied. The anisotropy is obtained because the etch rate is crystallographically dependent. For example, the etch rate of silicon along $\langle 100 \rangle$ is ~80 times larger than that along $\langle 110 \rangle$ in KOH because of the different atomic densities in different crystal directions (the etch rate depends on the chemical composition, concentration, and temperature) [38]. Recently, tetramethyl ammonium hydroxide (TMAH) has drawn some attention since it contains no alkali ions [39,40]. This makes it more compatible with CMOS processes. However, it has drawbacks limiting its popularity. These include a relatively low etch rate, hillock formation, and rapid evaporative losses of ammonia gas.

All of these crystallographic-orientation-dependent etchants require compensation to obtain designed structures; in addition, misalignments during lithography steps can lead to significant errors in the final results [41-43]. *Figure 1.6* gives an example of the planes occurring at convex corners during KOH etching; the lateral etching at the corner results in the undesired shape. Furthermore, high-quality hard masking materials such as silicon nitride and silicon oxide are required, since photoresist quickly dissolves in these base solutions. More importantly, wet process are difficult to control industrially and have low compatibility with IC processing. Therefore, the ability to dry etch deep and anisotropic microstructures in silicon has received much attention for bulk micromachining.

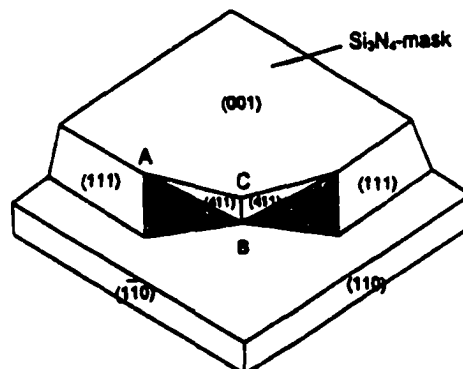


Figure 1.6: Planes occurring at convex corners during KOH etching of Si [41]

There are two reported approaches designed to deeply etch silicon with high aspect ratios (>25), cryogenic dry etching and the Bosch® process [33]. In the cryogenic etching method, the silicon substrate is maintained at cryogenic temperatures (77°K) using liquid nitrogen cooling to greatly enhance the anisotropy [44,45]. The anisotropy is

achieved by condensation of the reactant gases on the sidewalls of the etched structures; in contrast, the condensing gases at the bottom of structures are removed by ion bombardment. The commercial etcher made by Alcatel (San Jose, CA) can achieve aspect ratios on the order of 30:1. However, there is an important problem with cryogenic dry etching; the cryogenic temperature cannot be maintained locally if micro-structures become thermally isolated due to the continuous etching. As a result, this limits the type, shape, and size of micro-structures.

In 1994, Larmer and Schilp invented a high aspect-ratio silicon dry etching process, referred to as the Bosch® or deep-trench reactive ion etching (DRIE) process [46]. In this process, an alternating process of etching and protective polymer deposition is employed to achieve an anisotropy on the order of 30:1. An inductively coupled plasma (ICP) source is used to obtain a high-density and low-ion-energy plasma. As a result, a high etch rate (~2-3 $\mu\text{m}/\text{min}$) and a high selectivity (~30-100:1 to photoresist; ~120-200:1 to silicon oxide) are obtained. Commercial etchers using this principle are available from Surface Technology Systems, Ltd. (Redwood City, CA) and Plasma Therm, Inc. (St. Petersburg, FL). Moreover, the etching can be made either isotropic or anisotropic by adjusting the etching recipe. Therefore, versatile micro-structures can be fabricated with the combination of isotropic and anisotropic etching [47-49]. In summary, DRIE has greatly enhanced the ability to manufacture micro-structures for MEMS applications while maintaining compatibility with IC processing. Therefore, it is becoming the most popular tool for deep dry etching silicon in bulk micromachining.

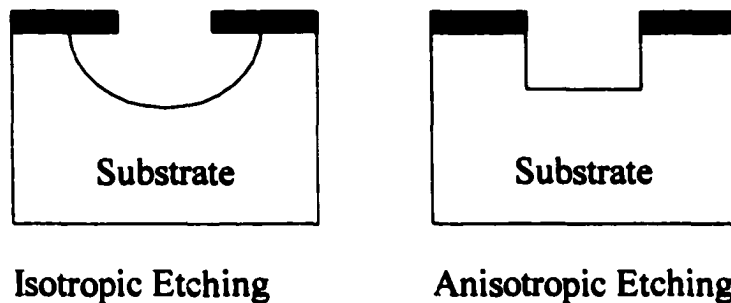


Figure 1.7: Etched profiles of isotropic and anisotropic etching

1.3.2 Ferroelectric Material Systems

Lead zirconate titanate (PZT) is a ferroelectric material; therefore, ferroelectricity is briefly introduced here. Ferroelectric materials are spontaneously polarized under equilibrium conditions and the spontaneous polarization can be reoriented between crystallographically defined states by applying a realizable electrical field [50]. All ferroelectric materials are piezoelectric since they all have polar structures. At high temperatures, many ferroelectric materials do not have a spontaneous polarization since they have a higher symmetry crystal structure (the paraelectric phase). The transition point is defined as the Curie temperature (T_c). At temperatures below T_c , a phase transformation occurs where the material distorts into a lower symmetry structure resulting in a ferroelectric phase with a spontaneous polarization. The appearance of polarization-field hysteresis is evidence for a re-orientable spontaneous polarization. A typical polarization electric-field (P-E) loop is shown in *Figure 1.8* [51]. Several

distinctive parameters should be noted in this figure. The saturation polarization (P_{sat}) is defined as the linear extrapolation of the polarization at high field back to a zero field point. It refers to the total polarization that can be attributed to the reversal of the spontaneous polarization. The remanent polarization (P_r) is defined as the polarization remaining in a ferroelectric material after the external electrical field is released (at $E=0$). This indicates the degree of alignment of dipole moments. The coercive field (E_c) is defined as the electrical field at which the net polarization is zero. Real hysteresis loops, especially in polycrystalline materials, are often slanted – different regions in the material reorient at different fields.

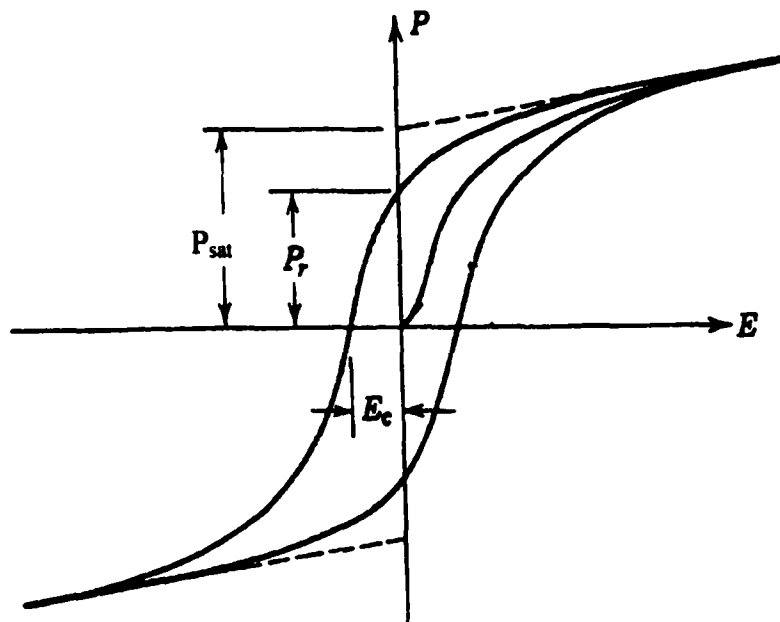


Figure 1.8: Polarization electric-field (P-E) hysteresis loop of a ferroelectric material [51]

1.3.3 Perovskite Structure of Lead Zirconate Titanate

One of the most important ferroelectric prototypes is the perovskite crystal structure; barium titanate and PZT belong to this family. PZT, $\text{Pb}(\text{Zr}_{1-x}\text{Ti}_x)\text{O}_3$, is a solid solution system between PbTiO_3 and PbZrO_3 [52]. Above T_c , the unit cell is cubic with ions arranged as in *Figure 1.9* and it is in a paraelectric phase. Below T_c , the cubic structure distorts into either a tetragonal or rhombohedral structure over most of the composition range (there is also an orthorhombic antiferroelectric). Due to this structural distortion, the relative shift of the oxygen octahedra and the cations results in the generation of an electrical dipole moment (in a ferroelectric phase).

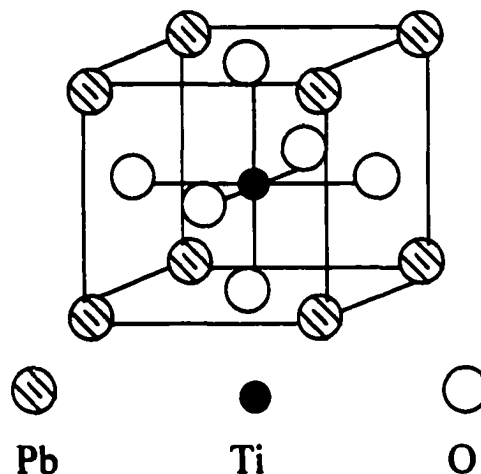


Figure 1.9: Perovskite structure of PZT; the corner atoms are Pb^{2+} , the face centered atoms are O^{2-} , and the central atom is either Zr^{4+} or Ti^{4+} [52]

Furthermore, the material properties of PZT can be adjusted by changing the ratio of PbTiO_3 and PbZrO_3 . The phase diagram of PZT is shown in *Figure 1.10* [53], where it

can be seen that it is in a rhombohedral phase for zirconium-rich compositions ($x < 0.52$) and in a tetragonal phase for titanium-rich compositions ($x > 0.52$) below the Curie temperature. In the rhombohedral distortion, there are eight possible orientations for the spontaneous polarization, which are along the 8 $\langle 111 \rangle$ directions of the cubic unit cell. In the tetragonal phase, there are six possible orientations for the spontaneous polarization along the 6 $\langle 100 \rangle$ directions of the cubic unit cell. One significant feature of PZT is the temperature-independent morphotropic phase boundary (MPB) between tetragonally and rhombohedrally distorted ferroelectric phases. It occurs close to a Zr:Ti ratio of 52:48 [54]. Bulk ceramics show significant enhancements in the dielectric and piezoelectric properties as a result of the larger number of possible orientations for the spontaneous polarization at the MPB composition. *Figure 1.11* shows that the coupling coefficient and relative permittivity reach their highest values at the MPB composition [53]. Although the maxima are less pronounced, some authors have reported that similar property peaks occur in PZT films [55]. There is some controversy, however, about whether the effective e_{31} coefficient peaks at the same composition, although compositional variations in the polability of sputtered films may have affected the later result [5]. Therefore, the PZT films used in this work are all prepared with 52/48 composition.

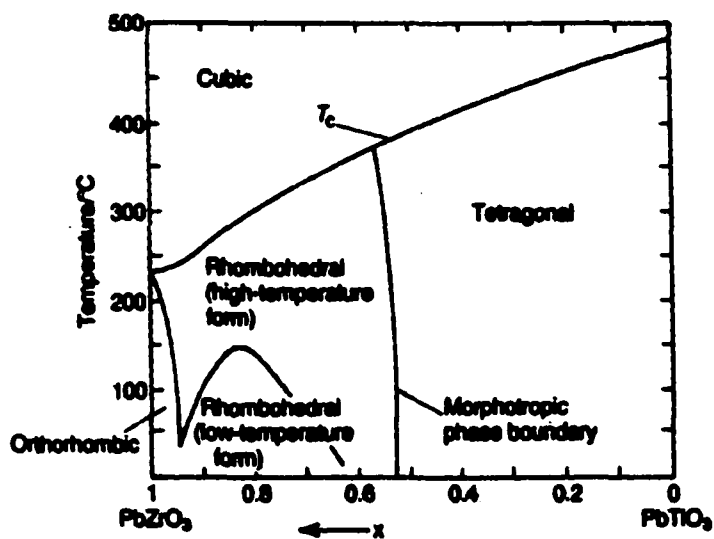


Figure 1.10: Phase diagram of PZT [53]

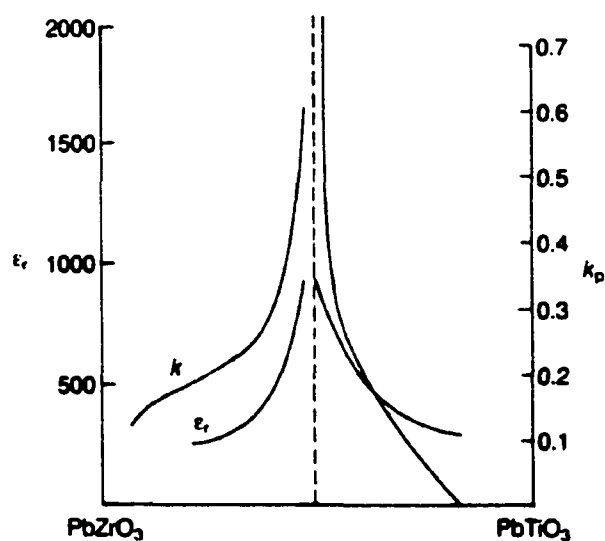


Figure 1.11: Coupling coefficient and permittivity values of PZT compositions [53]; k is coupling coefficient and ϵ_r is the relative permittivity

1.3.4 Piezoelectricity

Piezoelectricity will be introduced next to explain the operating principle of the accelerometer. Materials which develop a dielectric displacement proportional to an applied mechanical stress, or conversely, exhibit a proportional mechanical displacement (or strain) when subjected to an electrical field, are called piezoelectric materials. The former is the direct piezoelectric effect, which is usually used in sensor applications, and the latter is the converse effect, which is usually used in actuator applications. The constitutive equations of piezoelectricity are given in Eq. 1.2 and Eq. 1.3 [56].

$$D = dT + \epsilon^T E \quad (1.2)$$

$$S = s^E T + dE \quad (1.3)$$

where D , T , E , S , s , and d are dielectric displacement (C/m^2), stress (N/m^2), electric field (V/m), strain (m/m), compliance (m^2/N), and piezoelectric constant, usually given in C/N for the direct effect and m/V for the converse effect. The superscript denotes the parameter held constant. The piezoelectric constant depends on the orientation in which the mechanical stresses and electrical fields are applied. The existence of non-zero piezoelectric coefficients depends on the crystal symmetry of the material. For the PZT-based films used in this study, the most widely used operation modes are d_{33} and d_{31} . The first subscript denotes the polarization direction and the second one is the matrix notation for the stress. *Figure 1.12* illustrates these two operation modes. The MEMS

accelerometer is operated in d_{31} mode, so that stress amplification associated with flexing the element can be used to increase the sensitivity.

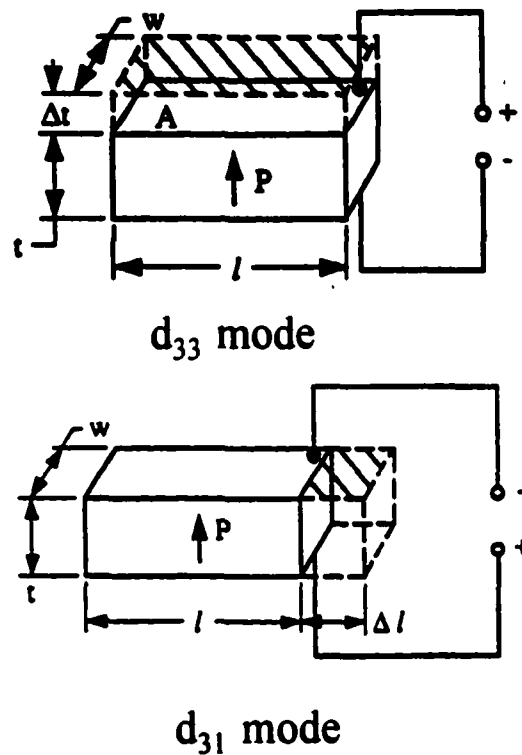


Figure 1.12: Schematics of d_{33} and d_{31} operation modes; the dashed areas show that changes in dimensions due to an applied stress lead to induced polarizations [53]

1.3.5 Interface Circuit

The interface circuit, to which the piezoelectric sensor is connected plays an important role in the sensor's operation as well as the electrical boundary conditions.

Figure 1.13 shows the configuration of the interface circuit used in the MEMS

accelerometers in this thesis. In this configuration, the piezoelectric film acts as a charge generator and the operational amplifier (op-amp) is in the inverting configuration serving as a charge amplifier. The op-amp is at virtual ground at point 1 for this configuration [57]; therefore, the charge generated from the piezoelectric film is quickly absorbed by the amplifier and leaves no charge on the electrodes. As a result, no potential develops across the film; that is, the film is effectively short circuited ($E \approx 0$). The charge, Q , generated by the film is transferred to the capacitance (C_F) in the amplifier's feedback loop. Hence, the output voltage, V_{out} , can be obtained by Eq. 1.4.

$$V_{out} = \frac{-Q}{C_F} \quad (1.4)$$

From the equation, it is clear that V_{out} depends on the feedback capacitance but is independent of the film and cable capacitances. Therefore, the length of the wire between the sensor and the electronics does not have a critical effect; in addition, charge leakage through stray capacitance around the sensor, such as in the packaging substrate, can be minimized.

The gain of the amplifier is expressed in Eq. 1.5:

$$Gain = \frac{C_s}{C_F} \quad (1.5)$$

where C_s is the film capacitance. The gain can be increased by increasing the film capacitance and decreasing the feedback capacitance. However, it is limited by the

bandwidth of the amplifier, which decreases with increasing gain. Since the electrical boundary conditions of the film (using the charge amplifier) approximate a short circuit, the constitutive equations of the piezoelectric film can be simplified from Eq. 1.2 and Eq. 1.3 to

$$D = dT \quad (1.6)$$

$$S = s^E T \quad (1.7)$$

This simplification will be beneficial to the derivation of the device's model in section 3.2.

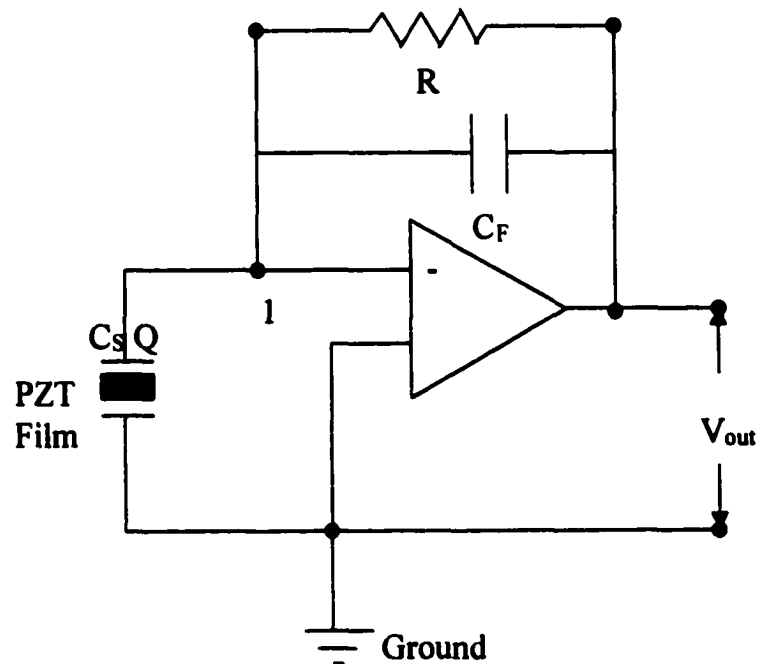


Figure 1.13: Electrical circuit configuration of a piezoelectric film connected to a charge amplifier

1.4 Research Objectives

The main objectives of this thesis were to design, fabricate, and test MEMS PZT accelerometers using silicon micromachining techniques. Problems encountered in this work in terms of design, fabrication, and testing, were studied in order to make high-performance, miniature, mass-production-compatible, and potentially circuitry-integratable accelerometers.

In the design aspect, different types of device structures were designed to study important accelerometer parameters including sensitivity, bandwidth, and transverse-sensitivity cancellation. Theoretical models, based on structural dynamics and piezoelectricity, were derived to help understanding both the device physics and relations between the design parameters. Therefore, the performance of accelerometers can be optimized for certain specifications.

For the fabrication aspect, these are the first reported MEMS accelerometers fabricated using a combination of the deep-trench reactive ion etching (DRIE) technique and piezoelectric PZT films. Therefore, processes developed in this work are beneficial for future research on PZT-based micromachined devices. Processing issues, including materials compatibility, metallization, processing of thick layers (PZT films and photoresist), double-side processing, deep-trench silicon etching, post-etch cleaning and process integration, presented the challenges in fabricating the MEMS PZT accelerometers.

Testing of MEMS PZT accelerometers was carried out by both electrical and mechanical excitations. Dynamic frequency response and impedance resonance

measurements were performed to evaluate the behavior of MEMS accelerometers. Processed PZT films were characterized by dielectric, polarization electric-field (P-E) hysteresis, and piezoelectric measurements, to insure no adverse effects on film properties. In addition, packaging of MEMS chips was developed to facilitate the testing as well as to improve noise rejection. The results were compared to theoretical and finite element analysis (FEA) results to evaluate the theoretical models and processing control.

Chapter 2

Processing and Characterization of PZT Films For MEMS Applications

2.1 Introduction

For many sensor applications, PZT films should be comparatively thick ($>1\mu\text{m}$) because the piezoelectric response increases with increasing film thickness [58]. However, depositing and processing of these thick films presents significant challenges [7]. Different deposition techniques, such as electron-beam evaporation [59], sputtering [60], ion beam deposition [61], metallo-organic chemical vapor deposition (MOCVD) [62], sol-gel [63], and laser ablation [64] have been used to deposit PZT films. Among these methods, sol-gel process has the advantages of easy chemical composition control, film homogeneity, high purity, large area deposition and low cost [65]. Therefore, the PZT films used in this work were all prepared by the sol-gel method. Deposition of thick PZT films up to $8\mu\text{m}$ thick by sol-gel method has been developed at Penn State University [66]. The preparation details and the correlations between preparation conditions and film properties are described elsewhere [67,68]. In this work, patterning of these thick PZT films using microfabrication techniques was investigated.

2.2 PZT Film Patterning Using Microlithography Processes

Lithography and etching are the key steps to define the films' geometry and to manufacture MEMS accelerometers. Different types of radiation, including ultraviolet light (optical lithography), electron-beam, X-ray, and ions, provide different resolutions for lithography. In this thesis, electron-beam lithography was used to generate photomasks and optical lithography to transfer the patterns on the photomask to the silicon wafer. A contact aligner (Karl Suss MA6) was used to provide UV radiation and alignment between photomask and wafer.

Reactive ion etching (RIE) using capacitive [69,70], inductive [71], or electron cyclotron resonance (ECR) plasmas [72] has been utilized to pattern PZT films. These studies were driven primarily by ferroelectric random access memory (FRAM) applications where PZT films are used as capacitors. The film thickness used in these applications generally does not exceed 250nm [73]. It has been reported that it is difficult to form volatile species with etching gases at room temperature; hence, heating the substrate or increasing the ion bombardment energy is generally required for dry-etch patterning. As a result, the etch rate and selectivity with respect to the photoresist developed in the above methods are not suitable to etch PZT films for MEMS applications, which generally require 2 to 10 μm PZT films. Therefore, a wet chemical route for patterning thick PZT films was developed here.

2.2.1 Lithography

General lithography and etching processes are illustrated in *Figure 2.1* and the basic principles and processing details are available elsewhere [74]. One important requirement for the lithography step used here is good adhesion between the PZT film and photoresist, since long etching times in HF-based solutions are used for patterning thick PZT films after the photolithography step. Hexamethyldisilazane (HMDS) was used to promote adhesion. HMDS is one of the most commonly used adhesion promoters for silicon oxide and photoresist in MOS processing [75]. It was spin-coated on the PZT films before spinning photoresist.

2.2.2 Patterning of PZT Thick Films

The chemical etchants utilized for the PZT thick films need to be compatible with photolithography processes. PZT ceramics can be etched by HCl, HF, H₃PO₄, HNO₃, H₂SO₄, NaOH, and KOH [76]. However, neither H₂SO₄ nor the basic solutions (NaOH, KOH) are suitable here, since photoresist is quickly stripped in these solutions. In addition, the etch rate for H₃PO₄ and HNO₃ is slow. Therefore, three etching recipes, 1) 0.34%HF:5%HCl:94.66%H₂O at room temperature; 2) HF at room temperature; and 3) HCl at 45°C, were first investigated to pattern the thick PZT films. In each case, the etchant was stirred. However, there were some problems with each etchant. For the first recipe, residues on the etched area could not be removed even for a long etching time (30minutes); consequently, the photoresist delaminated from the PZT films. A whitish

residue was clearly observed after drying the sample. SEM (*Figure 2.2*) shows this residue in the etched area. Adjusting the ratio of HF and HCl did not lead to markedly different results.

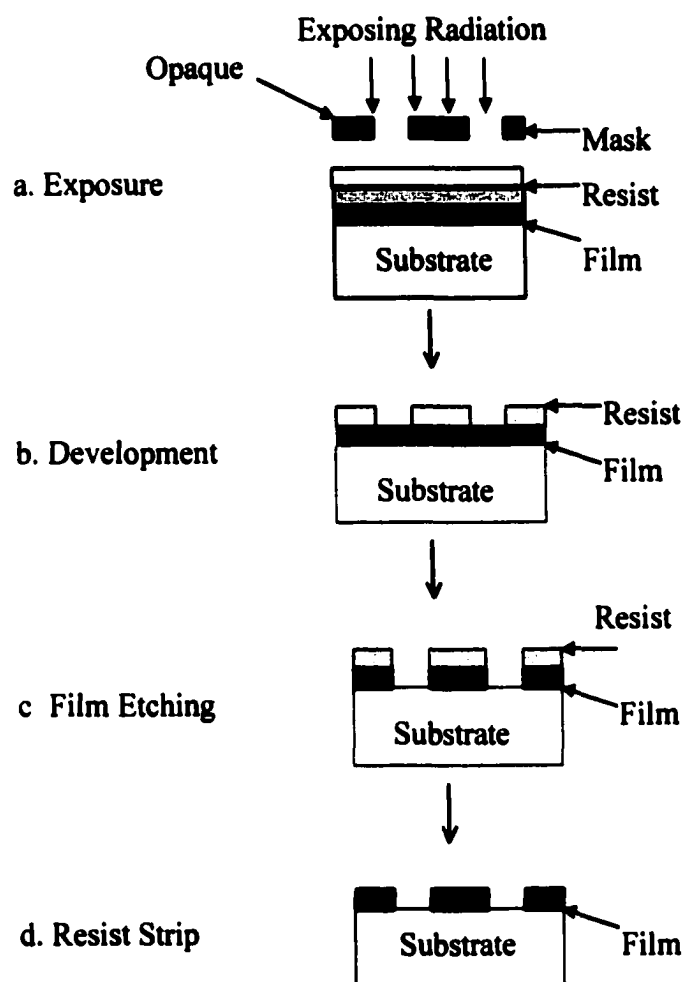


Figure 2.1: General lithography and etching processes



Figure 2.2: SEM micrograph showing residue in the etched area after etching a 4 μm PZT film in 0.34%HF:5%HCl:94.66% H_2O for 40 minutes

For the second recipe, residue formation was still a problem. Furthermore, the photoresist delaminated from the PZT films after only 10 minutes of etching. For the third recipe, residue was not a problem. However, patterns with feature sizes smaller than 50 μm cannot be well patterned, since HCl quickly etched the PZT films by dissolving along the grains boundaries [76]. This also resulted in severe undercutting and overall this etching process was difficult to control. *Figure 2.3* shows a 50 μm square pixel that was attacked by HCl. Photoresist did not provide adequate protection. *Table 2.1* summarizes the results of the above etching recipes.



Figure 2.3: Scanning electron micrograph showing a 50 by 50 μ m pixel patterned using HCl etching solution; the HCl has quickly attacked the PZT grain boundaries

Table 2.1: Comparison of different etching recipes for PZT thick films

Etching recipe	Etch Rate	Resist	Undercut (lateral to thickness)	Residue
0.34%HF 5%HCl 94.66%H ₂ O at 25° C	~0.2 μ m/min*	peeled after 30 minutes	3:1*	whitish residue
HF at 25° C	~0.15 μ m/min*	peeled after 10 minutes	2:1*	whitish residue
HCl at 45° C	(1 μ m/min)	does not provide good protection	10:1	clean surface

*Etch rate and undercutting are approximate since the end point of etching is difficult to define with the formation of residues

2.2.3 Residue Analysis

From the above results, it is apparent that residue formation resulted from use of HF-based solutions. X-ray diffraction (XRD) was used to characterize the residue. It was done by a Scintag DMC-105 diffractometer (Scintag, Inc., Sunnyvale, CA) using Cu $K\alpha$ radiation. A scan rate of 2 degree per minute was used for the data collection. XRD patterns indicate that the residues primarily consist of the metal fluorides, $Pb_{0.85}Zr_{0.15}F_{2.3}$ and Pb_5ZrF_{14} (see *Figure 2.4*), which have a very low solubility in the etching solutions. It was found that these residues can be quickly removed by HCl in a short time (~30 seconds). *Figure 2.5* shows that after a brief HCl dip, only PZT peaks were detected in the XRD patterns, and no residue was observed.

2.2.4 Two-step Etching Process

From the above results, no single etching step was found that can provide a residue-free surface, good selectivity, and limited undercutting for patterning thick PZT films. Consequently, a two-step etching process was developed. The procedures are summarized in *Table 2.2*. A 10:1 buffered oxide etch (BOE, which is $10HN_4F:1HF$) was used in the first etch step to remove most of the material. Here BOE is preferred rather than HF, because the photoresist delaminated from PZT films in straight HF after a relative longer etching time (~15 minutes for 2 μm films). As stated earlier, after rinsing with water and drying with a nitrogen gun, whitish residues on the etched area were observed. These residues resulted in a root mean square (RMS) surface roughness of 0.3

μm (RMS), measured by a surface profilometer (Tencor Instrument Alphastep). A second etch in $2\text{HCl}:1\text{H}_2\text{O}$ solution for 30 seconds at an elevated temperature (45°C) was used to remove the residues. The etching time needs to be kept short to minimize any further undercutting. Using this two-step process, a cleaner etched surface and better pattern transfer were obtained, as shown in *Figure 2.6*. *Figure 2.7* shows an etched profile. In addition, the etched surface was examined by XRD and no residue was found (see *Figure 2.8*). The etching stopped successfully at the Pt bottom electrode.

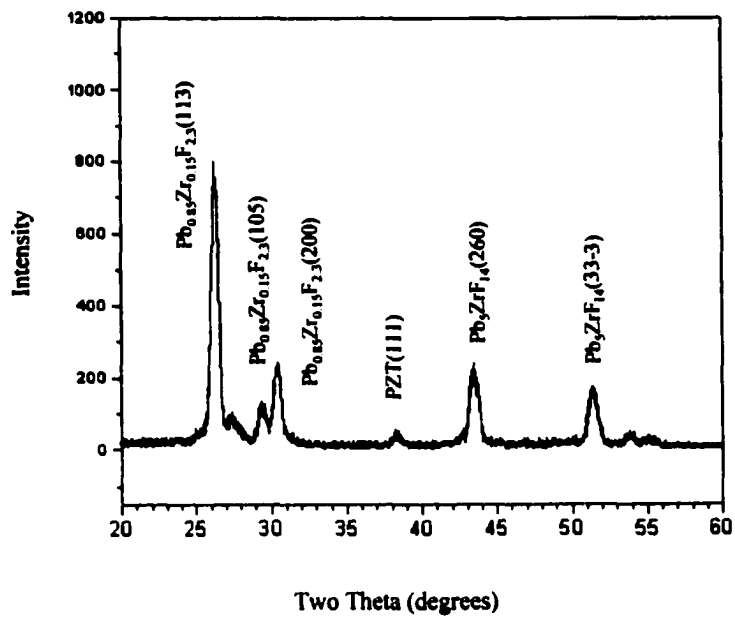


Figure 2.4: XRD showing residues consisting of metal fluorides; this sample was etched with an HF-based solution only

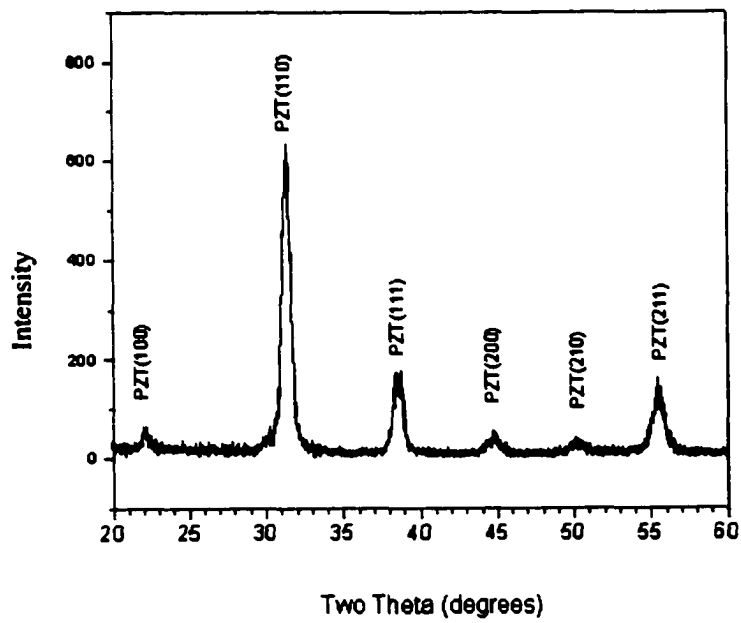


Figure 2.5: XRD pattern showing no residue on a sample which was incompletely etched in HF and then quickly dipped in HCl

Table 2.2: Two-step etching processes for thick PZT film patterning

Step	Process	Remark
1	BOE (10:1) etching at room temperature	Rate: 0.133 (μm /min)
	DI water rinsing and nitrogen gun drying	whitish residues on the etched area
2	2HCl:H ₂ O at 45° C	Time: 30 second
	DI water rinsing and nitrogen gun drying	Clean surface



Figure 2.6: SEM micrograph showing well-patterned 2 μm PZT films and a clean etched surface resulting from two-step etching

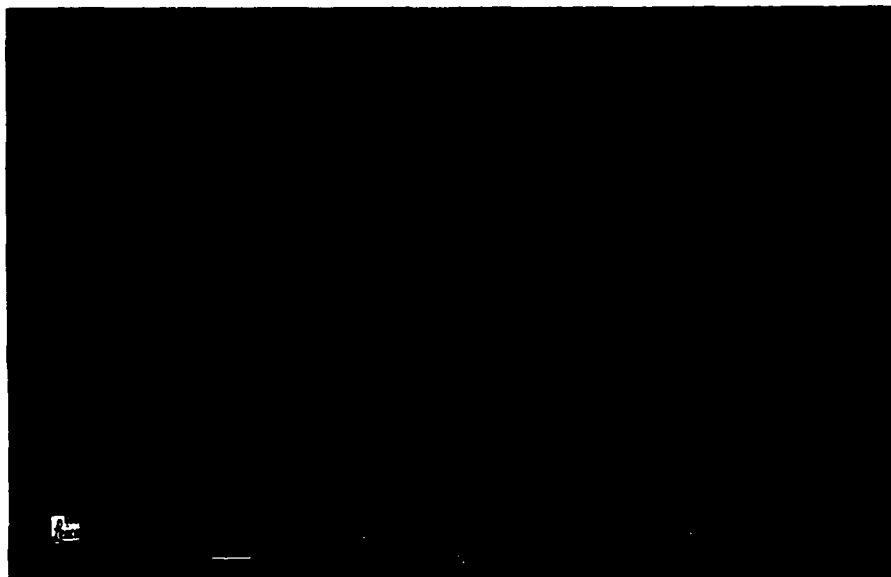


Figure 2.7: Etched profile of a 2 μm PZT film from lateral view

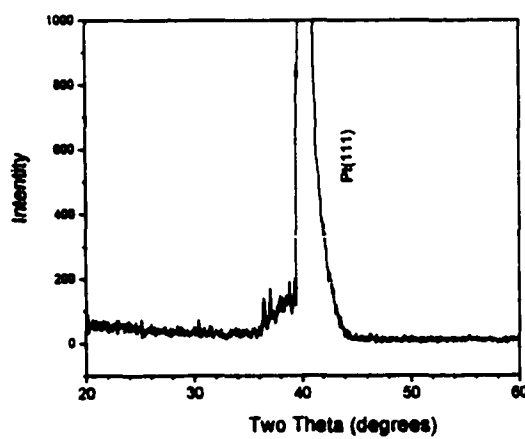


Figure 2.8: Surface etched by two-step etch examined by XRD; no residue was found. Pt is the bottom electrode

Since the wet etching process is isotropic, lateral etching cannot be avoided. One way to describe the degree of undercutting is the ratio of lateral to thickness etching. To determine this, the size of an etched pattern after stripping the photoresist was measured by microscopy and compared to the original photomask size. A ratio of 2 to 1 lateral to thickness undercutting was measured. The second etch step contributed half of the overall undercutting even with the short etching time because HCl quickly attacked the PZT film at the sidewalls. For most MEMS devices, 2:1 undercutting is acceptable since the feature size in MEMS is relatively larger than in microelectronics.

2.3 Characterization of Processed PZT Films

PZT films are used as the active material in accelerometers; therefore, the sensitivity of the device depends on the properties of the PZT films. In order to examine if there was any degradation in properties associated with the etching process, the processed films were characterized by dielectric, ferroelectric, and piezoelectric measurements. The uniformity of the films across a wafer surface was also examined.

2.3.1 Film Thickness and Uniformity

The thickness of PZT films was measured by a surface profilometer (Tencor Instrument Alphastep) after the films were patterned by the two-step etch process, as described in the previous section. Two samples were measured at points across the whole 4" wafers to evaluate the uniformity. For the thinner one, the average thickness is

1.7 μm with standard deviation of 0.037 μm . For the thicker one, the average thickness is 5.95 μm with standard deviation of 0.12 μm . These results ($< \pm 3\%$ variation across a 4" wafer) show good uniformity of PZT films deposited by the sol-gel method. The films are thicker in the middle and thinner near the edges (see *Figure 2.9*).

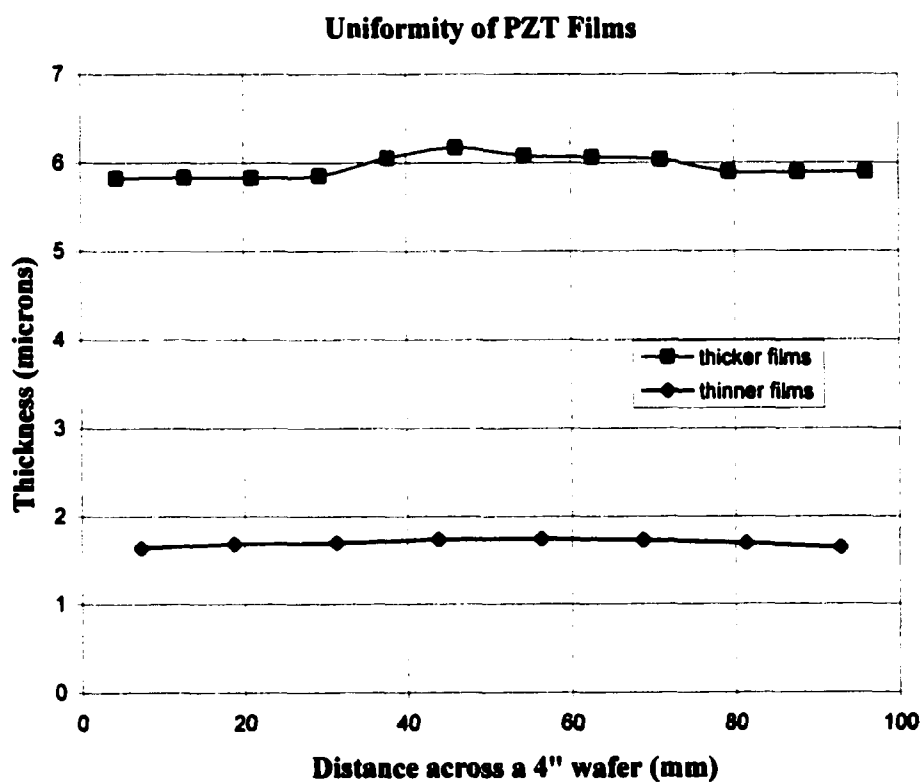


Figure 2.9: Uniformity of PZT films across 4" wafers

2.3.2 Measurement of Dielectric Properties

The capacitance (C) and dielectric loss ($\tan\delta$) of processed PZT films were measured using a multi-frequency LCR meter (Hewlett Packard 4274). The testing frequency was 1 kHz and the electrical field was 0.5 kV/cm. The relative permittivity (κ) can be calculated from Eq. 2.1.

$$\kappa = \frac{C \cdot t}{\epsilon_0 \cdot A} \quad (2.1)$$

A and t are the area and thickness of PZT films; ϵ_0 is the permittivity of vacuum. Results show that the average relative permittivity is 1000 with a standard deviation of 50, and the average dielectric loss is 1.6% with a standard deviation of 0.15% across a 4" wafer (see *Figure 2.10*).

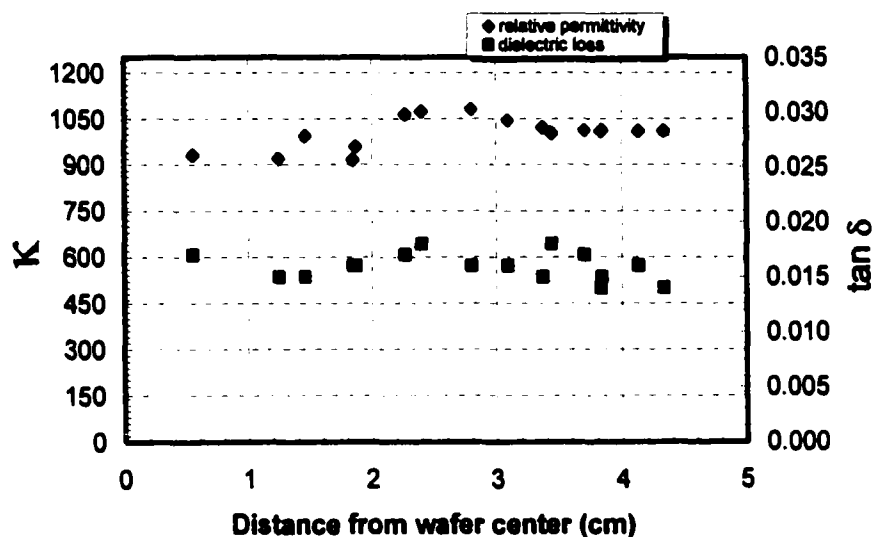


Figure 2.10: Permittivity and dielectric loss of etched 6 μm PZT films across a 4" wafer

2.3.3 Measurement of Ferroelectric Properties

The polarization hysteresis is usually measured by a Sawyer Tower circuit [48]. Here, a commercial ferroelectric tester (Radiant Technologies RT66A) based on this principle was used to measure the P-E hysteresis of processed PZT films. The measurement frequency was 30 Hz and the maximum electrical field was 500 kV/cm. For thick films, an external power amplifier (AVC Instrumentation 790 Series power amplifier) was used to provide a higher electric field. With this measurement, the remanent polarization (P_r) and coercive field (E_c) can be obtained. *Figure 2.11* shows the average P-E hysteresis loop across a 100mm wafer. The average P_r is $24 \mu\text{C}/\text{cm}^2$ with a standard deviation of $2.2 \mu\text{C}/\text{cm}^2$, and the average E_c is 42.1 kV/cm with a standard deviation of 3.7 kV/cm (see *Figure 2.12*). All tested results show good properties of processed PZT films. The observed properties were similar to those of unpatterned films of the same thickness.

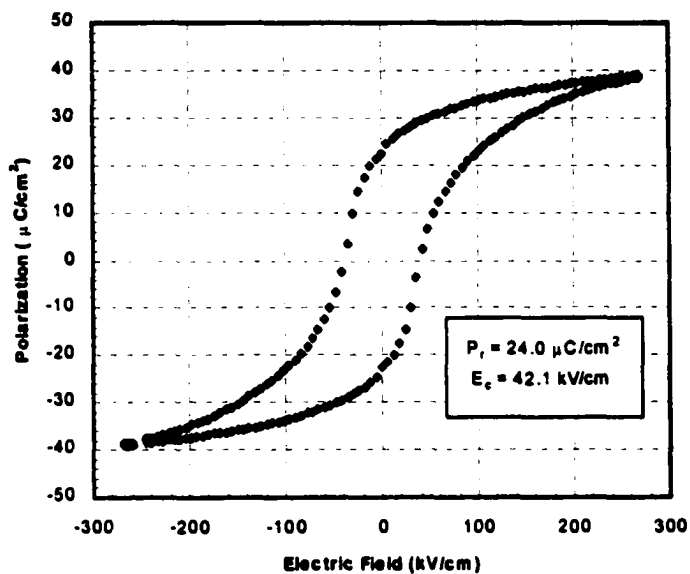


Figure 2.11: Average P-E hysteresis loop of a processed 5.95 μm PZT film across a 4" wafer

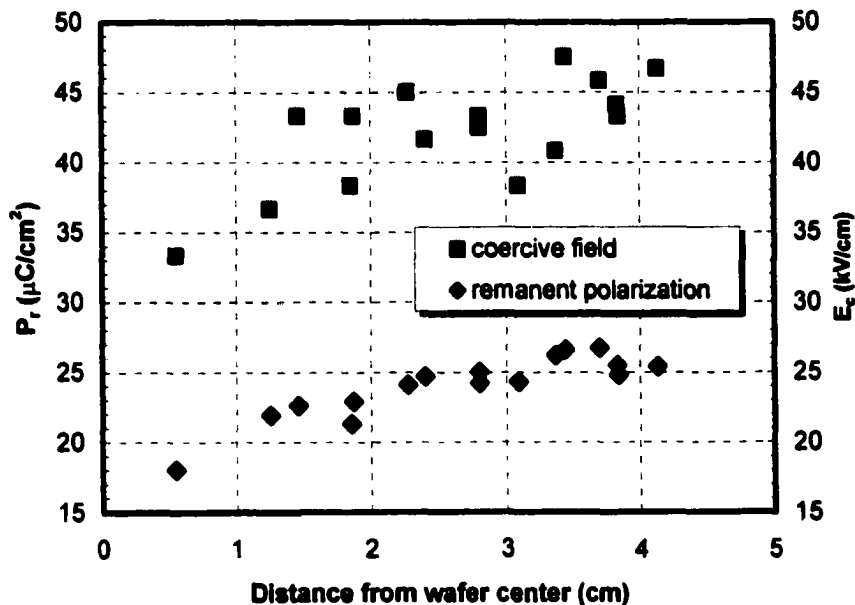


Figure 2.12: Coercive field and remanent polarization of a processed 5.95 μm PZT film

2.3.4 Measurement of the Transverse Piezoelectric Constant

Since the charge sensitivity of the MEMS accelerometer is directly proportional to the transverse piezoelectric constant (d_{31}), a better knowledge of d_{31} value leads to a more accurate theoretical calculation (detailed in section 3.2.3). Here, a simple and inexpensive method, developed by Shepard et al. [77], was utilized to measure $e_{31(\text{eff})}$ or d_{31} . Basically, the technique is based on the direct piezoelectric effect. An ac (~ 10 Hz) planar stress was applied to the PZT film through flexure of the underlying 3" silicon wafer using a pressure jig (see *Figure 2.13*). The charge output of the PZT film was connected to a charge integrator and converted into a voltage output. The applied pressure (therefore, the applied stress) was measured by a pressure transducer. *Figure 2.14* shows the equipment setup. Finally, the d_{31} was calculated based on plate theory for a known applied stress and voltage output. The detailed measurement procedure and technique are described in reference [77]. For measurement of test chips from the MEMS run, a slightly modified approach was used [78].

Before the measurement, a dc electrical field was applied between the top and bottom electrodes. This will reorient dipoles of the PZT films towards the direction of the applied field. Therefore, the net piezoelectric charges are not cancelled inside the films, when they are under stress. This procedure is termed poling. The PZT films were poled under 150 kV/cm electric field at room temperature for 15 minutes. The same poling condition is applied for the accelerometers before the frequency response measurement, which will be described on Chapter 5. The average measured d_{31} was -45 pC/N (assuming a Young's modulus of 101 GPa).

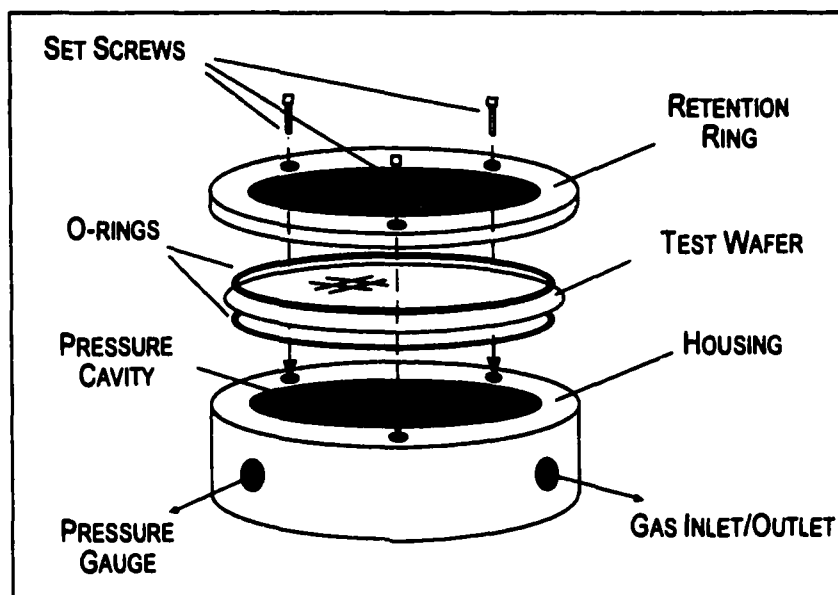


Figure 2.13: A pressure jig for d_{31} measurement [77]

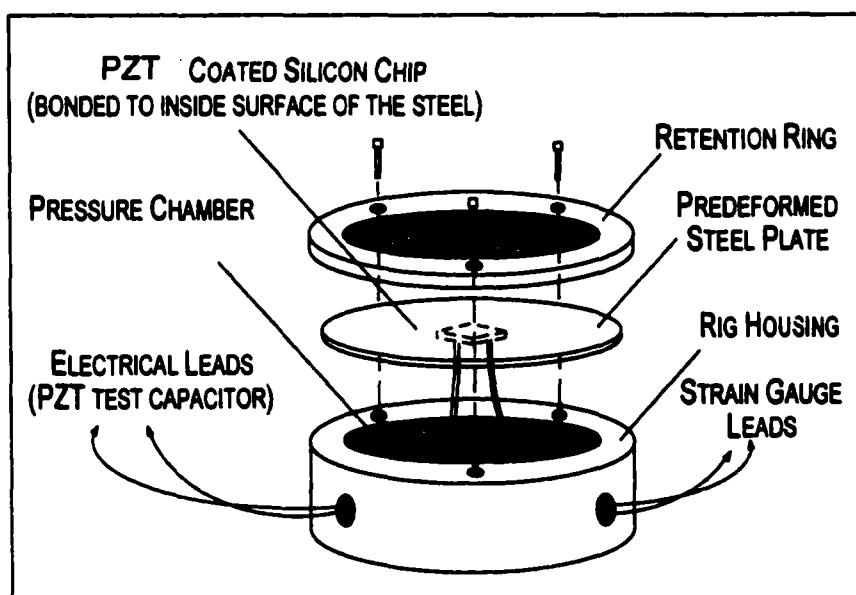


Figure 2.14: Equipment setup for measuring the transverse piezoelectric constant [78]

Chapter 3

MEMS Accelerometer Design I: Cantilever-Beam Structure

3.1 Device Design and Model

3.1.1 Device Structure and Design

A cantilever beam is the most common sensing structure for micromachined accelerometers because of its simplicity and low spring constant. Thus, a silicon cantilever beam with a silicon proof mass on the free end was used as the sensing element in the first accelerometer design, since the proof mass considerably improved the sensitivity. However, a big drawback of this type of design is the sensitivity to transverse accelerations because of the asymmetric mass distribution. For example, the desired acceleration sensing mode of the accelerometer is in the y direction (Q_y) as shown in *Figure 3.1*. When an x direction acceleration occurs, the bending moment generated from this resultant force also contributes to the piezoelectric charge, Q_x . In order to cancel the transverse sensitivity, the accelerometer was designed with four beams in a die with two beams opposing the other two (see *Figure 3.2*). The charge output of the left-hand-side beams when exposed to an acceleration containing components in both y and x directions, Q_L , equals

$$Q_L = Q_y - Q_x$$

The charge output of the right-side beams, Q_R , equals

$$Q_R = Q_y + Q_x$$

When the outputs of all four beams are connected, the total charge output, Q_T , equals

$$Q_T = Q_L + Q_R = 2*Q_y$$

Therefore, the transverse charge output in the x direction is cancelled. For a z-direction acceleration (see *Figure 3.3*), the generated charge on each beam is zero, since the stress on the beam on the opposite sides of the X axis is equal and opposite. Thus, for the ideal geometry, the transverse sensitivity can be eliminated, which is an important feature of this design. Three different sizes of beams are designed here to study the relation between the resonant frequency and sensitivity. Their dimension are shown in *Table 3.1*.

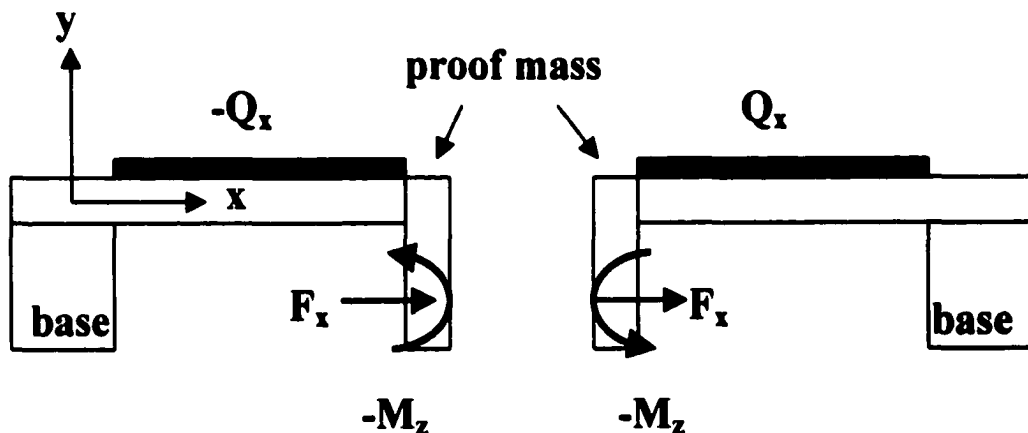


Figure 3.1: Transverse sensitivity cancellation in the x direction

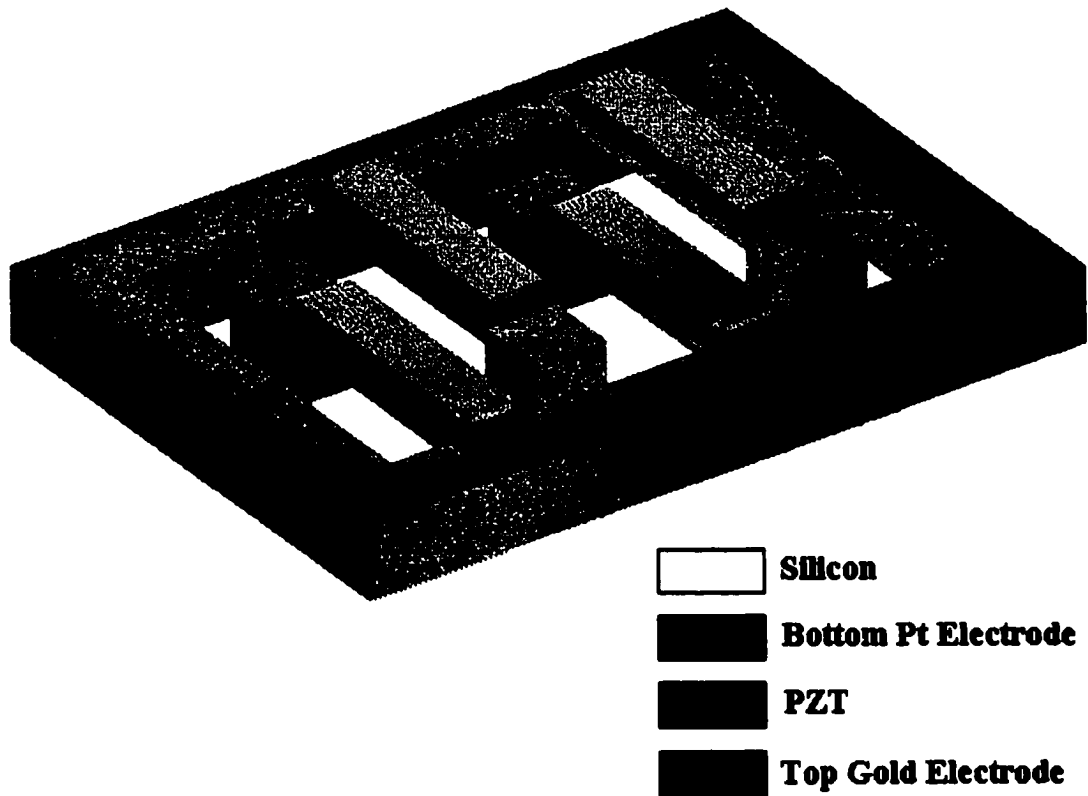


Figure 3.2: Schematic of PZT MEMS accelerometer; it consists of four cantilever beams with a proof mass at the end

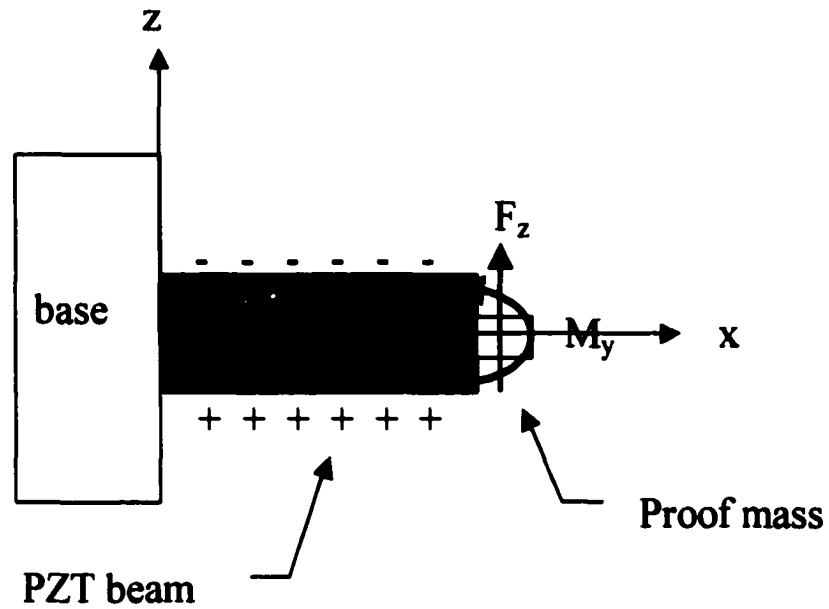


Figure 3.3: Charge cancellation in the z direction

Table 3.1: Dimension of cantilever-beam accelerometers

Device type	Silicon beam			Top electrode	
	Length (mm)	Width (mm)	Thickness (μm)	Length (mm)	Width (mm)
Small beam	1.00	0.80	50	0.96	0.76
Medium beam	1.27	0.80	50	1.23	0.76
Large beam	1.80	0.80	50	1.76	0.76
*Proof mass	0.30	0.35	450		

Note:

- 1) * Size of proof mass for all three beams is the same
- 2) The length and width of PZT layers are the same as the top electrode

3.1.2 Derivation of Structure Dynamics

It is useful to be able to model the dynamics of the accelerometer. Euler-Bernoulli beam theory is used here to describe the equation of motion of the beam [79]. The proof mass on the free end of a cantilever beam can be treated as an inhomogeneous boundary condition containing the eigenvalue as shown in *Figure 3.4*. The equation of motion and boundary conditions of the system are described in Eq. 3.1-3.3 [80].

Equation of motion:

$$EI \frac{\partial^4 u(x,t)}{\partial x^4} + m \frac{\partial^2 u(x,t)}{\partial t^2} = 0 \quad (3.1)$$

At the fixed end ($x=0$), the boundary conditions are:

$$\begin{cases} u(0,t) = 0 \\ \frac{\partial u(0,t)}{\partial x} = 0 \end{cases} \quad (3.2)$$

At the free end ($x=L$), the boundary conditions are:

$$\begin{cases} EI \frac{\partial^2 u(L,t)}{\partial x^2} = -I_0 \frac{\partial^2}{\partial t^2} \left(\frac{\partial u(L,t)}{\partial x} \right) \\ EI \frac{\partial^3 u(L,t)}{\partial x^3} = M_0 \frac{\partial^2 u(L,t)}{\partial t^2} \end{cases} \quad (3.3)$$

where L , E and I are the length, Young's modulus, and moment of inertia of the composite beam respectively; M_0 , and I_0 are the mass and moment of inertia of the proof mass respectively; m is the beam mass per unit length. The transverse displacement at any point along the beam is denoted as $u(x,t)$, which is a function of both the spatial coordinate x and the time t .

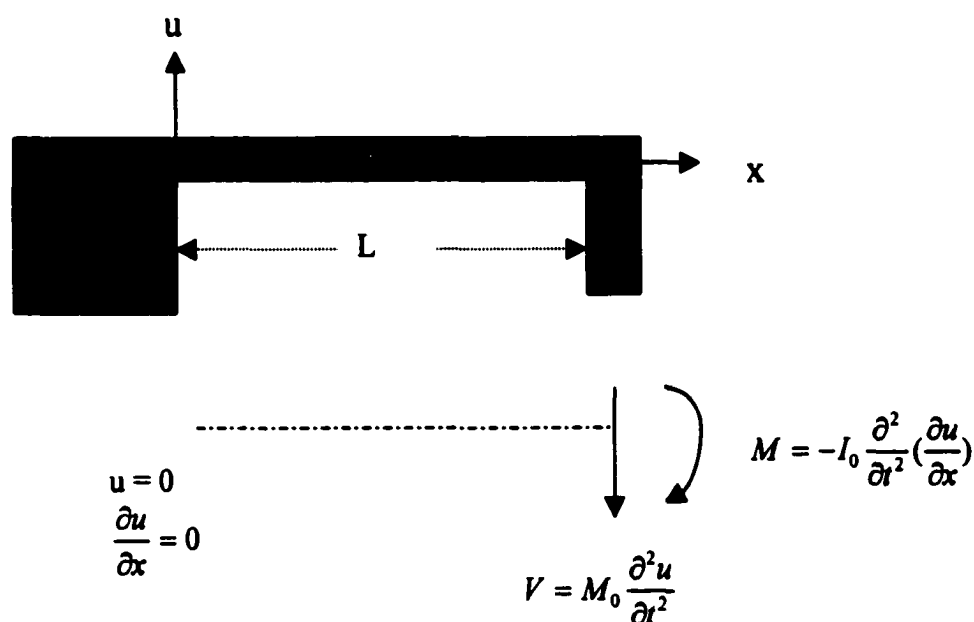


Figure 3.4: Boundary condition of a cantilever beam with a proof mass on the free end; M and V are the bending moment and shear force generated from the proof mass

Here, only silicon and PZT layers are considered in this composite beam, since the silicon oxide, top-, and bottom-electrode layers are relatively thin. Therefore, the equivalent EI of the composite beam is defined in Eq. 3.4

$$EI = E_s \cdot I_s + E_p \cdot I_p \quad (3.4)$$

where E_s and E_p are the Young's moduli of silicon and PZT; I_s and I_p are the moment of inertia of the silicon and PZT layers about the neutral axis of the composite beam.

Using the method of separation of variables, $u(x,t)$ can be expressed in Eq. 3.5. Therefore, the equation of motion (Eq. 3.1) can be separated into Eq. 3.6 and Eq. 3.7 by introducing the eigenvalue (ω^2).

$$u(x,t) = g(t) * y(x) \quad (3.5)$$

$$\frac{d^2 g(t)}{dt^2} + \omega^2 g(t) = 0 \quad (3.6)$$

$$EI \frac{d^4 y(x)}{dx^4} = m\omega^2 y(x) \quad (3.7)$$

By substituting Eq. 3.5 into Eq. 3.2 and 3.3, the time-independent boundary conditions are obtained in Eq. 3.8 and 3.9. At the fixed end ($x=0$), the boundary conditions are:

$$\begin{cases} y(0) = 0 \\ \frac{dy(0)}{dx} = 0 \end{cases} \quad (3.8)$$

At free end ($x=L$), the boundary conditions are:

$$\begin{cases} EI \frac{d^2 y(L)}{dx^2} = I_0 \omega^2 \frac{dy(L)}{dx} \\ -EI \frac{d^3 y(L)}{dx^3} = M_0 \omega^2 y(L) \end{cases} \quad (3.9)$$

The solution of Eq. 3.7 is expressed in Eq. 3.10 with four constants, C_1 , C_2 , C_3 , and C_4 .

$$y(x) = C_1 \sin \beta x + C_2 \cos \beta x + C_3 \sinh \beta x + C_4 \cosh \beta x \quad (3.10)$$

where β is the re-defined eigenvalue given in Eq. 3.11.

$$\beta^4 = \frac{m\omega^2}{EI} \quad (3.11)$$

Applying the four boundary conditions (Eq. 3.8 and 3.9) to Eq. 3.10, a matrix can be obtained (Eq. 3.12):

$$\begin{bmatrix}
 0 & 1 & 0 & 1 \\
 1 & 0 & 1 & 0 \\
 \sin \beta L + \frac{I_0 \beta^3 \cos \beta L}{m} & \cos \beta L - \frac{I_0 \beta^3 \sin \beta L}{m} & -\sinh \beta L + \frac{I_0 \beta^3 \cosh \beta L}{m} & -\cosh \beta L + \frac{I_0 \beta^3 \sinh \beta L}{m} \\
 -\cos \beta L + \frac{M_0 \beta \sin \beta L}{m} & \sin \beta L + \frac{M_0 \cos \beta L}{m} & \cosh \beta L + \frac{M_0 \beta \sinh \beta L}{m} & \sinh \beta L + \frac{M_0 \beta \cosh \beta L}{m}
 \end{bmatrix}
 \begin{bmatrix}
 C_1 \\
 C_2 \\
 C_3 \\
 C_4
 \end{bmatrix}
 =
 \begin{bmatrix}
 0 \\
 0 \\
 0 \\
 0
 \end{bmatrix}
 \quad (3.12)$$

For a non-trivial solution, the determinant of the first matrix in Eq. 3.12 has to be zero. By plotting the determinant as a function of β (see *Figure 3.5*), the eigenvalue (β_n) corresponding to each mode of the structure where the determinant is zero can be numerically calculated (using MATLAB program). The subscripts denote the n^{th} mode of the eigenvalue, eigenfunction, and resonant frequency. Knowing β_n , the resonant frequency (ω_n) can be calculated from Eq. 3.11; in addition, the ratios of C_1 to C_2 , C_3 , and C_4 can be obtained. Therefore, the eigenfunction (ϕ_n), or normal mode, is obtained by Eq. 3.10 given the ratios of C_1 to C_2 , C_3 , and C_4 . However, the magnitude of the eigenfunction is not unique and can scale in any way. Here, it is convenient to normalize the eigenfunctions so that the normalized values satisfy the relationship (Eq. 3.13):

$$\int_0^L m \phi_n^2(x) dx = 1 \quad (3.13)$$

Figure 3.6 shows the first two modes of the medium beam (1.27mm in length). The total displacement response can be obtained by supposing the mode response shown in Eq. 3.14.

$$u(x,t) = \sum_{n=1}^{\infty} \phi_n(x) \cdot g_n(t) \quad (3.14)$$

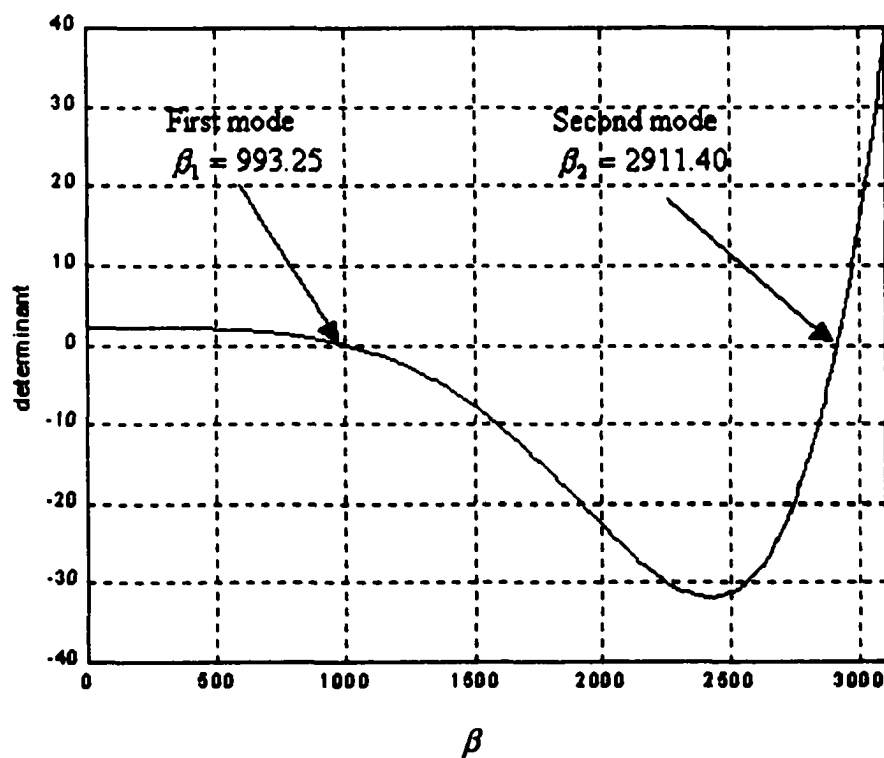


Figure 3.5: Eigenvalues corresponding to the first and second modes of a cantilever beam (1.27mm in length) with a proof mass at the free end

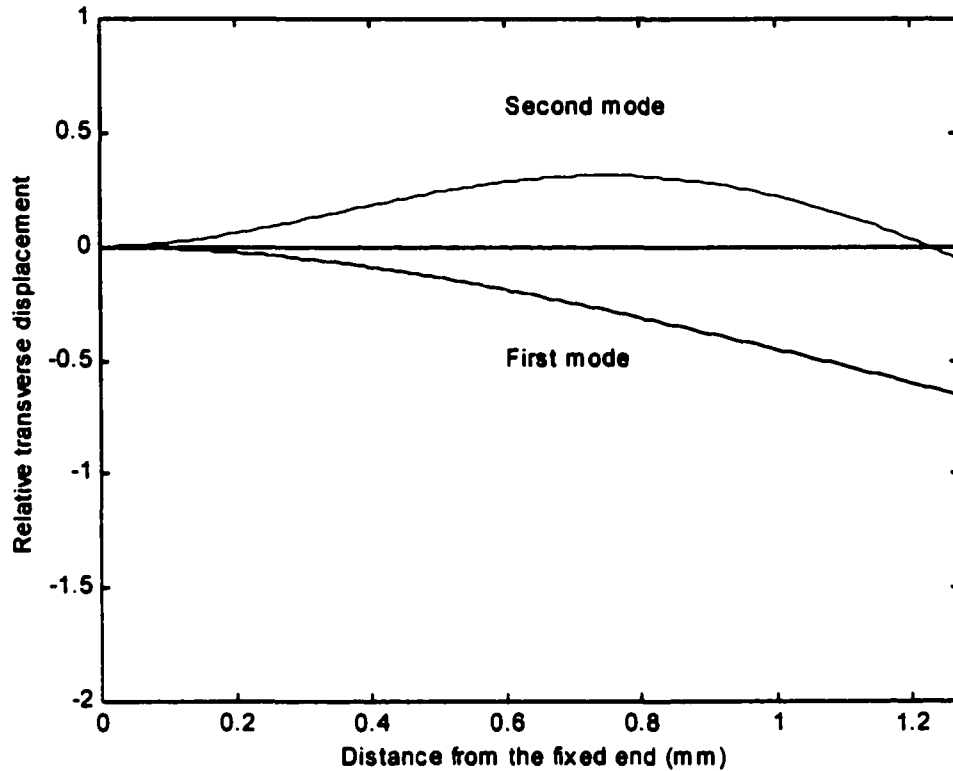


Figure 3.6: Mode shape of a cantilever beam (1.27mm in length) with a proof mass on the free end

3.1.3 Analytical Solution of Charge Sensitivity

To calculate the sensitivity of the accelerometer, a load (P) is defined as the force generated from the proof mass under a one-g acceleration (9.8m/s^2); as a result, the charge output is the sensitivity. For the forced vibration, a normalized forcing term is added on the righthand side of Eq. 3.6 to yield Eq. 3.15.

$$\frac{d^2 g_n(t)}{dt^2} + \omega^2 g_n(t) = \int_0^L \phi_n(x) \cdot P(x) dx \quad (3.15)$$

Since the frequency for the sensitivity calculation is in the flat frequency response range below the first resonant frequency; the quasistatic solution of Eq. 3.15 (g_s) is solved by setting the second time derivative term of Eq. 3.15 to be zero. Finite element analysis (FEA) of the PZT MEMS accelerometers were also performed using ANSYS, assuming under this condition (quasistatic analysis with piezoelectric coupling). Here, only the first two modes are superposed and expressed in Eq. 3.16. It gives a reasonable approximation (within 90%) for the quasistatic response [80].

$$y(x) = \sum_{n=1}^2 \phi_n(x) \cdot g_s \quad (3.16)$$

Then the bending moment (M) along the x direction can be obtained by Eq. 3.17.

$$M = EI \frac{d^2 y}{dx^2} \quad (3.17)$$

Since the Young's modulus of PZT and silicon are different, the stress distribution along the y axis of the composite beam is not continuous (see *Figure 3.7*). However, the

normal strain (ε_x) is continuous. Therefore, the average normal stress on the PZT layer (σ_x) can be calculated by Eq. 3.18.

$$\sigma_x = E_p \cdot \varepsilon_x = \frac{E_p M y_0}{EI} \quad (3.18)$$

where y_0 is the distance from the neutral axis to the middle of the PZT layer.

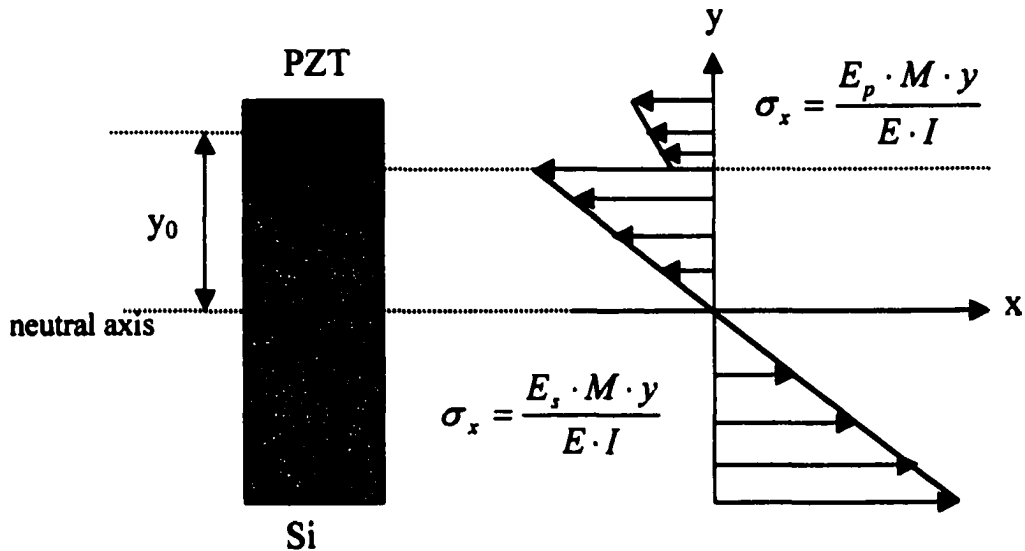


Figure 3.7: Stress distribution of the PZT and silicon composite beam along the y axis

The distribution of the normal stress (σ_x) at the middle of the PZT layer along the x-axis is plotted in *Figure 3.8*. There also is a shear stress (τ_{xy}) on the PZT films, when the beam is subjected to pure bending. However, it does not contribute to the charge output of the PZT accelerometer, because it is in the d_{15} mode and no electrode is placed on the

area normal to the x axis. As a result, the constitutive equations of the piezoelectric film can be simplified into one dimension. The dielectric displacement caused by σ_x can be obtained by simply substituting Eq. 3.18 into Eq. 1.5. Finally, the total charge can be obtained by integrating over the top electrode area as Eq. 3.19.

$$Q = \int \sigma_x \cdot d_{31} \cdot b_m \cdot dx \quad (3.19)$$

where b_m is the width of the top electrode. The analytical solution based on the above calculation will be compared to the FEA and measured values in Chapter 5.

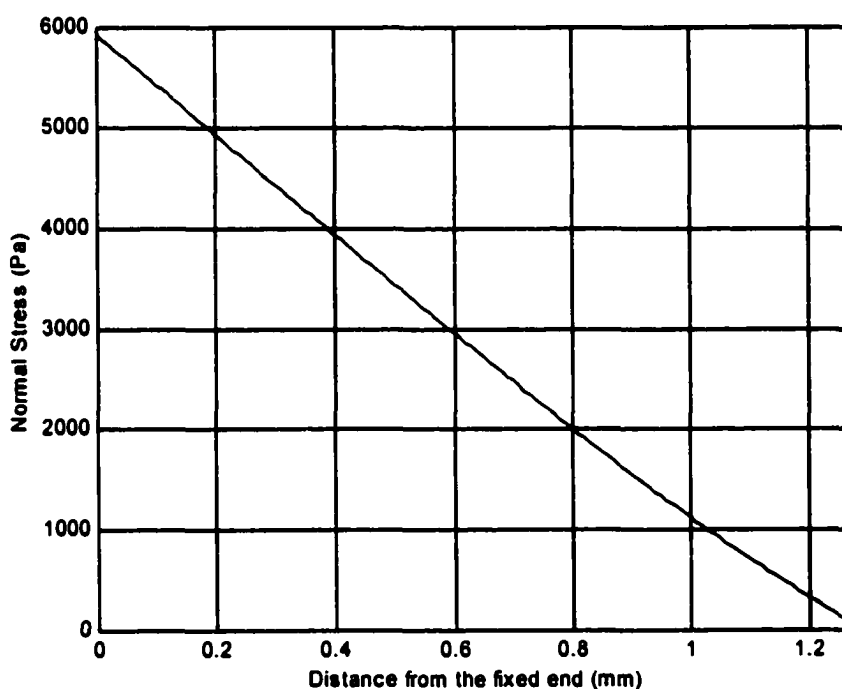


Figure 3.8: The distribution of the normal stress in the middle of the PZT layer for a cantilever beam beam (1.27mm in length) with a proof mass on the free end

3.1.4 Optimization of PZT and Silicon Beam Thickness

The thickness of the PZT and silicon layers plays an important role in the structure dynamics, influencing the sensitivity and resonant frequency. However, the piezoelectric constant is not independent of the PZT film thickness. It increases with increasing film thickness (see *Figure 3.9*). [68]. Therefore, it is not appropriate to optimize the PZT and silicon beam thickness without considering material properties. For example, *Figure 3.10 (a)* shows that the thickness of the PZT layer needs to be as thin as possible to obtain the maximum sensitivity, when assuming the piezoelectric constant is independent of the PZT thickness and the silicon beam thickness is fixed at 50 μm . However, the PZT thickness needs to be as thick as possible to have the maximum sensitivity (see *Figure 3.10 (b)*), when the thickness-dependent piezoelectric constant is applied. This is because the effect of the thickness-dependent piezoelectric constant is greater than the effect of the structure dynamics for the thickness of interest. In the summary, it is necessary to consider all the parameters in terms of structure dynamics, film properties, and manufacturing feasibility to have a practical optimization. Two approaches are used and illustrated in the following.

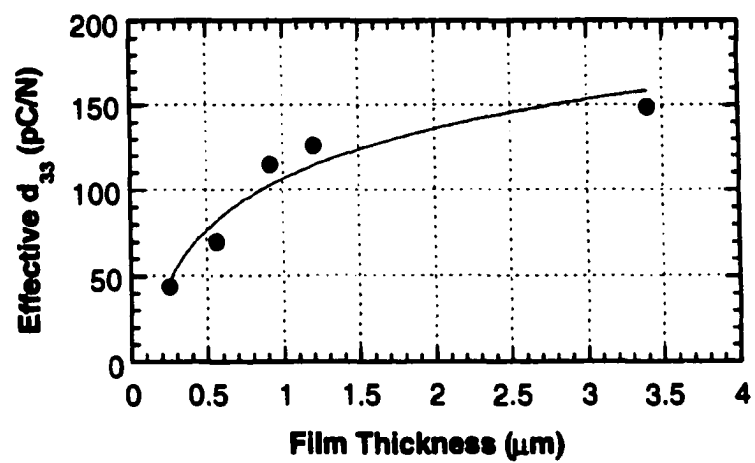
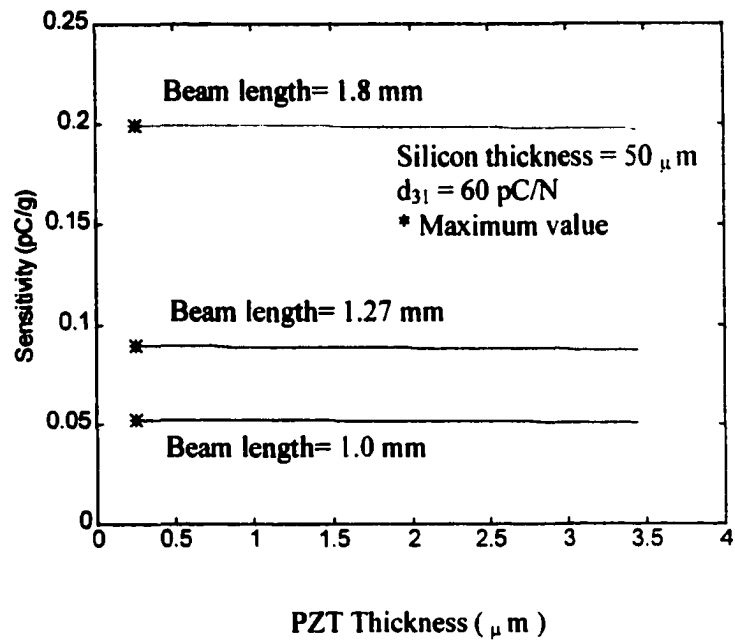
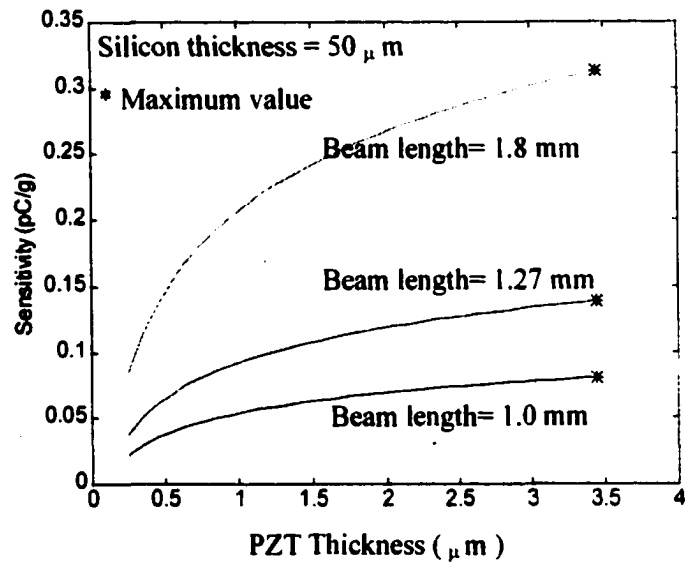


Figure 3.9: Thickness dependence of piezoelectric constant of PZT film [68]



(a)



(b)

Figure 3.10: Optimized PZT thickness for a 50 thick silicon beam (a) without (b) with considering the thickness-dependent piezoelectric constant

Case 1 - maximum sensitivity:

From *Figure 3.9*, it is clear that the thicker the PZT film, the higher the sensitivity that can be achieved; however, the film thickness is limited because of manufacturing feasibility. The film starts to crack after a certain thickness because of the stress build-up during deposition. For practical purposes, the PZT film was fixed at 6 μm , which can be routinely achieved at Penn State. *Figure 3.11* shows the sensitivity for different thicknesses of the silicon beam. The sensitivity increases with decreasing silicon thickness, because the bending stiffness of the composite beam decreases. As a result, under the same acceleration, the strain on the PZT film increases with lower beam stiffnesses. However, the neutral axis of the composite beam moves from the silicon layer toward the PZT layer with decreasing silicon thickness. The neutral axis moves inside the PZT layer when the silicon thickness is smaller than 5.26 μm . Charges generated on opposite sides of the neutral axis will have different signs. Hence, this will result in some charge cancellation. When the rate of charge cancellation exceeds the rate of decreasing stiffness, the sensitivity starts to decrease. The maximum sensitivity can be obtained at a silicon thickness of 2.8 μm . However, this thin silicon layer presents a challenge in the manufacturing, which will be discussed in Section 4.3.3.

Case 2 - fixed resonant frequency

For some situations, the first fundamental resonant frequency of an accelerometer needs to be specified in order to have the required bandwidth. Therefore, the equivalent EI of the composite beam should be fixed. For maximum sensitivity at a fixed resonant

frequency, the thickness of the PZT film should be set at the manufacturable maximum and then the thickness of the silicon layer should be adjusted to achieve the desired resonant frequency.

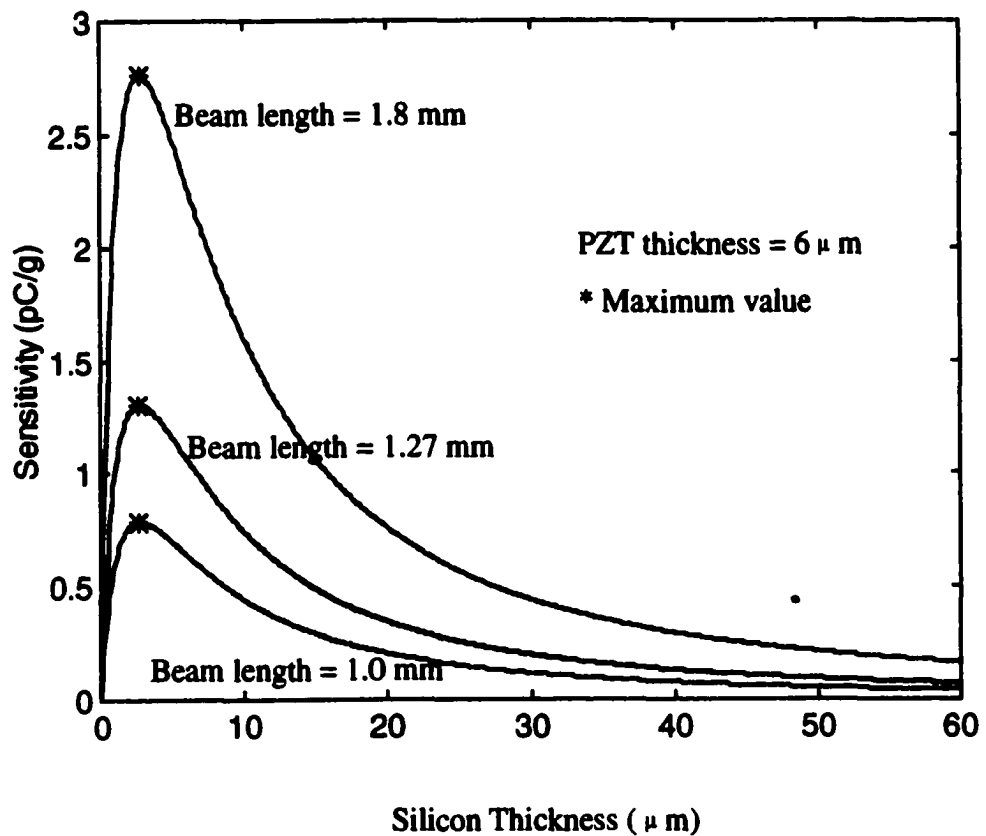


Figure 3.11: Sensitivity of MEMS accelerometers for different thickness of silicon layers; the thickness of the PZT layer is fixed at 6 μm

3.1.5 Sensitivity and Bandwidth

A wide, flat frequency response and a high sensitivity are always desirable and should be considered when designing an accelerometer. The former can be achieved by increasing the first fundamental resonant frequency of the device; however, the sensitivity will become lower. Therefore, there is a tradeoff between them and the device design should be tailored for the specific applications. The intended frequency range of 9 to 20 kHz for the MEMS accelerometers in this work was chosen for machine monitoring applications. This gives charge sensitivities ranging from 1 pC/g to 0.3 pC/g.

3.2 Processing Development

3.2.1 Overview

The PZT MEMS accelerometer is fabricated using bulk micromachining technology. The free-standing structures are released by etching the bulk silicon substrate from the backside of the wafer, while the front side contains the top electrode, bottom electrode, and PZT layers. Therefore, both sides of the wafer need to be processed and aligned with each other. As a result, front-to-backside photolithography presents the first challenge of the processes. The feature size of MEMS accelerometers is not critical compared to most microelectronic applications; however, the processing of relatively thick layers presents other challenges. Patterning of thick PZT films has already been discussed in the Chapter 2. Thick-resist photolithography is necessary to

provide good step coverage over already patterned features and to provide enough thickness for long DRIE steps.

3.2.2 Front-to-backside Alignment

Initially, etch-through holes were used as front-to-backside alignment marks. KOH and tetramethyl ammonium hydroxide (TMAH), the two most common base solutions for silicon crystal-orientation-dependent etching, were both used to etch holes on the wafer. However, the subsequent processing steps were problematic because high-quality PZT films could not be obtained by deposition either before or after the formation of the etch-through holes. If the PZT films were deposited before the etching of holes, there was no good way to protect them in the KOH or TMAH solution. On the other hand, the PZT films deposited using the sol-gel method on the wafers with holes were not uniform around the holes. Also, the wafers were easily broken during high temperature processing (due largely to unintentional pitting of the wafer surfaces).

An alternative method was successfully carried out using a mechanical jig (a design that originated from NIST and was made by Wilcoxon Research) for the front-to-backside alignment. It consists of two photomask plates, which are clamped and aligned. The holder is then subsequently disassembled and reassembled around the resist-coated wafer. The schematic of the alignment jig is shown in *Figure 3.12*. Both sides of the assembly are then exposed in a Karl Suss MA6 contact aligner. A $<25\mu\text{m}$ accuracy, which is the best resolution for general mechanical fixtures, was routinely obtained.

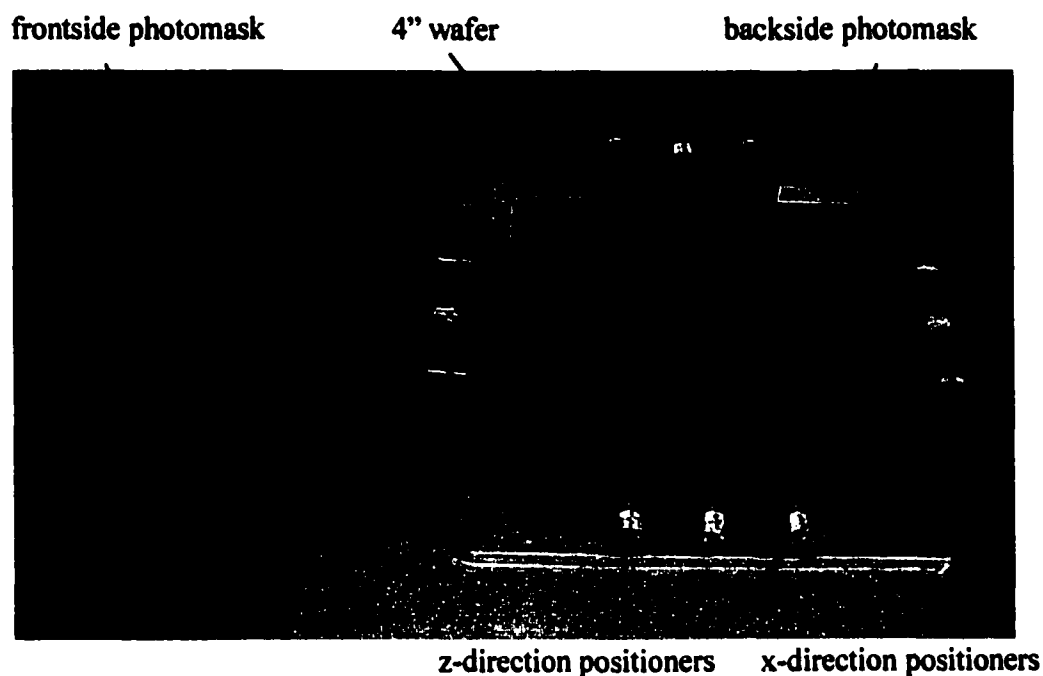


Figure 3.12: The mechanical jig for the front-to-backside alignment

3.2.3 Metallization

A Si/SiO₂/Ti/Pt multilayer structure was used here as the initial substrate for production of high quality PZT films. Pt is one of the preferred metals for the electrode material because of its low resistivity and good stability against oxidation and reaction with PZT during the subsequent high temperature processes. However, its adhesion to Si/SiO₂ is poor; as a result, it peeled during the subsequent processing steps. Therefore, a thin Ti layer was used as an adhesion promotion layer. 20nm of Ti was used to avoid the formation of a thick, low permittivity TiO₂ layer between the ferroelectric and the bottom

electrode. In addition, an important experimental result was that Ti/Pt metal layers electron-gun evaporated at room temperature tend to have higher tensile stresses than layers sputtered at $\sim 300 - 400^{\circ}\text{C}$. As a result, the electrode/PZT film stack cracked and peeled when deposited on the evaporated metal layer. Therefore, sputtered Ti/Pt layers were utilized here. The sputtered Ti/Pt layers were prepared by a vendor (Nova Electronic Materials, Richardson, TX).

For the top electrode, thermally evaporated Ni was initially used. However, the resulting effective dielectric constant of the PZT pixels was ~ 600 , which is lower than the normal value, 1000. This is because of the formation of a low dielectric constant NiO_x thin layer at the PZT/Ni interface; as a result, the total capacitance dropped due to the low capacitance material in series. Therefore, the top electrode was switched to Ti/Au or Cr/Au, which has a greater resistance to oxidation. In addition, the top Au contacts facilitate the final wire-bonding steps with Au bonding wire.

3.2.4 Thick-resist Photolithography

Thick resist was needed in the process for two reasons: providing good step coverage over the already etched patterns and providing enough thickness for the DRIE steps. AZ4620 photoresist (Hoechst Celanese Corp., Somerville, NJ) was used. One main difference between the thick resist and thin resist (such as Shipley 1800 series) is that the viscosity of the thick resist is much larger. As a result, it is difficult to wet the wafer surface completely and achieve good adhesion. Therefore, a dispersion step was utilized to spread the resist evenly on the surface at low spin speed and to wet the surface

completely. However, the uniformity of the resist becomes poor (especially on the wafer edge), if the dispersion speed is too low. From the experiment, it was found that 370 rpm dispersion speed can provide both good adhesion and uniformity. Thickness control was also important for the thick resist processing. However, many variables, such as surface topology, surface condition, wafer size, and initial location of resist, affect the thickness. Therefore, the spin curve was measured first; it shows a 35% deviation from the recommended data (see *Figure 3.13*). All of the following processes were based on the measured curve. The photolithography steps using this resist are detailed in *Table 3.2*. The thickness used for the PZT etch mask was 6.9 μm , where good step coverage can be obtained over patterned PZT films up to 6 μm thick. However, excessive photoresist thickness is not preferred, since it would complicate the resist stripping step following dry etching. For the mask for DRIE steps, the selectivity of the resist to silicon is about 50 to 1. Therefore, a 13 μm resist layer was sufficient for etching through the entire wafer.

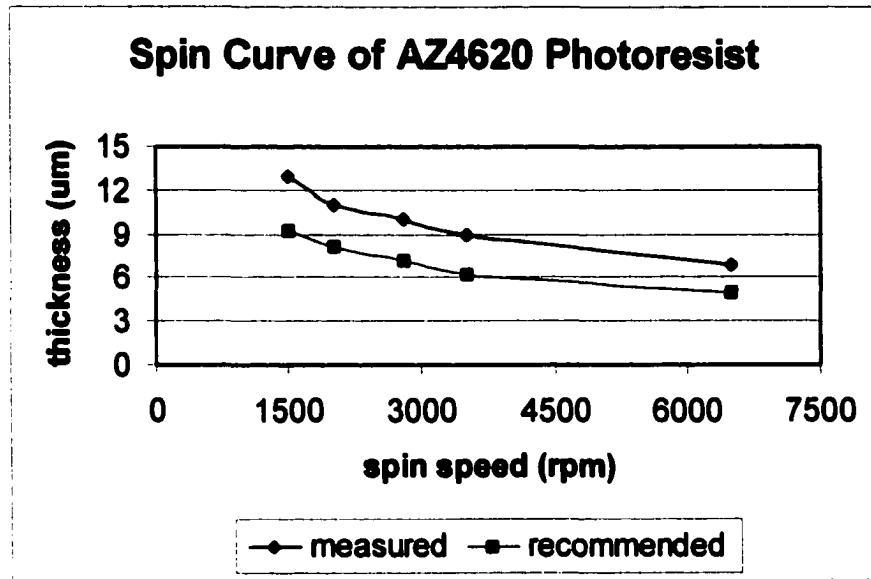


Figure 3.13: Spin curve of AZ4620 photoresist

Table 3.2: AZ4620 photolithography steps

	Step	Description	Remark
1	Dehydrate	10min@ 120 ^o C	Remove moisture
2	HMDS	10sec@ 3600rpm	Improve adhesion
3	Spread	15sec@ 370rpm	Better dispense for thick resist
4	Spin	45sec	See <i>Figure 3.13</i> for the thickness
5	Softbake	200sec@ 110 ^o C	
6	Expose	5.2 sec/ μ m@ 10mW/ cm ²	40mJ/cm ² per μ m (from data sheet)
7	Develop	180sec	Developer: AZ400K:4DI

3.2.5 Deep Reactive Ion Etching

The DRIE steps for the cantilever-beam accelerometers were done at BF Goodrich Advanced Micromachines (Cleveland, Ohio) using a Surface Technology Systems (STS) single-chamber multiplex ICP etcher using the Bosch® process, which is licensed by Robert Bosch GmbH [46]. The processing principles [81] as well as the pre- and post- processing procedures developed in this work are discussed in the following:

For the DRIE process, an inductively coupled plasma (ICP) source is the key to provide high concentrations of etching species at low pressure and low dc bias. Unlike the capacitively coupled plasma source, an ICP source uses electrodeless excitation; therefore, it avoids the high-voltage sheath. ICP can achieve a plasma density about 100 times higher than the capacitively coupled one with a dc voltage of ~20-30 V [82]. In addition, the electrode, on which the wafer is placed, is independently driven by a capacitively coupled rf source to control the ion energy. Hence, it is possible to independently control the ion fluxes (through the coil source power) and ion-bombarding energy (through the wafer rf power) of the ICP source. The high density plasma provides the high concentrations of etching species (thus the high silicon etch rate) and the low ion-bombarding energy gives a high selectivity with respect to the etch mask (photoresist or silicon oxide).

The process includes alternating cycles of etching and polymer deposition steps to achieve an anisotropy on the order of 30:1. During the etching cycle, sulfur hexafluoride (SF_6) is used. Silicon is etched by the atomic fluorine dissociated from SF_6 and forms the volatile SiF_4 . However, the silicon etch using fluorine radicals is spontaneous and does

not require ion bombardment; this results in a nearly isotropic etch. Thus, the subsequent polymer deposition cycle prevents lateral etching by sidewall passivation. This is done using C_4F_8 gas. The polymer on the base is quickly removed during the re-etching cycle where a low rf bias is applied, resulting in ion bombardment. Silicon etching takes place after the polymer is removed.

In the STS etcher, the wafer was electrostatically clamped and cooled with a He flow on the backside of the wafer. For the photomask design, dies were separated when the wafer was etched through. However, when the etching was nearly etched through, leakage of He and shattering of dies were observed. To solve this problem, a carrier wafer was glued to the front side of the wafer using Shipley 1813 photoresist (spun at 3600rpm). Both wafers were then baked on a hotplate at $100^{\circ}C$ for 10 minutes. During the baking, a ~5 lb weight was applied on the wafers to get good contact and prevent the formation of voids, which would reduce the thermal conductivity and cause bubble formation during the DRIE steps. After finishing the DRIE steps, a combination of plasma ashing and a modified Pirhana etch (Nanostrip, Cyantek Inc., Fremont CA) were used to strip the photoresist residue.

3.2.6 Processing Procedures

The PZT MEMS accelerometer was fabricated using four photomask levels including a front-to-backside alignment step. The four photomask levels include: a top metal (referred to herein as M2) pattern which doubles as the PZT etch mask; a lower, or

M1, metallization layer pattern; and two backside beam definition patterns (B1 and B2) which form the silicon cantilevers. The fabrication process flow is shown in *Figure 3.14* and is described in the following:

The starting substrate was a 4-inch diameter, n-type <100> (1-10 Ω -cm), double-side-polished silicon wafer. After standard RCA cleaning and a native oxide etching, an 800 nm thermal oxide was grown on the wafers, followed by the sputtering deposition of a low-stress Ti (20 nm)/Pt (150 nm) lower metallization (M1) layer. The frontside oxide serves as electrical isolation, while the patterned backside oxide serves as an etch mask for the backside cantilever beam processing. A $\sim 2\mu\text{m}$ thick blanket PZT was deposited by a sol-gel process. Following the PZT deposition, the top (M2) metallization layers of 8 nm Ti and 80 nm Au were deposited via thermal and electron-gun evaporation, respectively. The first photolithography step was a front-to-backside alignment (masks M2/PZT and B2) as described in section 3.3.2.

After development, the top Au layer was then wet etched using the gold etchant (42% KI: 3% Iodine Complex: 55% H_2O) from Transene Company, Inc., Danvers, MA. Then, a two-step wet etch process was utilized to pattern the PZT layer as described in Section 2.2.5. The initial buffered oxide etch in the first step also serves to remove the thin top Ti plus the exposed backside oxide and stops effectively on the underlying frontside Pt.

The front side of the wafer was then patterned using the M1, or lower level metal, mask using a thick AZ4620 resist ($6\mu\text{m}$ in this case). Using the resist, the lower Ti/Pt layers were reactive ion etched (RIE) using a Plasma Therm RIE720. The etching

species are a mixture of Cl_2 (27 sccm) and O_2 (3 sccm) gases at 6 mTorr and 400 W, resulting in a 700V DC self-bias. A subsequent oxygen plasma ashing step was used to remove the photoresist. *Figure 3.15* shows the patterned top electrode/PZT and bottom electrode layers.

At this point, the cantilever proof masses, beams, and die frames were formed by a 4620 thick resist process and two DRIE steps. The proof masses and die frames were defined by the B1 backside mask, using the AZ4620 resist with a thickness of approximately $13\mu\text{m}$. The wafers were then attached backside-up to carrier wafers using thin Shipley 1813 resist to maximize heat transfer to the cathode. The first DRIE step was used to define the thickness of the cantilever beams; $50 \pm 5\mu\text{m}$ was obtained based on a timed etch of 20 minutes. After the beam definition, an HF etch was used to remove the patterned oxide on the beam areas, after which a ~ 2 hour DRIE step was used to etch through the wafers (visual endpoint detection).

Figure 3.16 shows the released cantilever beam and proof mass after two DRIE steps. The tapered profile of the proof-mass sidewalls resulted from two sources, heating problems and a loading effect. The thermal conductivity of the thin bonding resist was still too low and it resulted in photoresist bubbling. Therefore, the rf bias during the etching cycle was lowered from its optimum value; as a result, the etching was more isotropic. Furthermore, one wafer was not successfully etched through since it suffered from low etch selectivity because of this problem. The thick resist was totally removed half way through the etching procedure (i.e. the selectivity was about 20:1). The other

main reason for the tapered profile was a loading effect. The area exposed to the plasma was 53% of the wafer area. During the polymer deposition cycle, chemical loading occurred because of this large exposed area. As a result, the polymer coating was preferentially deposited near the resist. This resulted in non-uniform sidewall passivation. That is, the sidewall was better protected in the area near the resist edge than in the depth of the trench. The undercutting reduced the proof mass by 48% from the designed value; therefore, it reduced the device sensitivity by approximately the same margin. The frontside oxide was removed by another RIE step from the backside of the wafer. The photoresist was stripped using a combination of plasma ashing and a Pirhana etch, $5\text{H}_2\text{SO}_4:\text{H}_2\text{O}_2$, (Nanostrip, Cyantek Inc., Fremont CA). After the final resist- strip step, the accelerometers were ready for the testing.

The heating and loading problems were solved in subsequent designs, as will be discussed in Chapter 4.

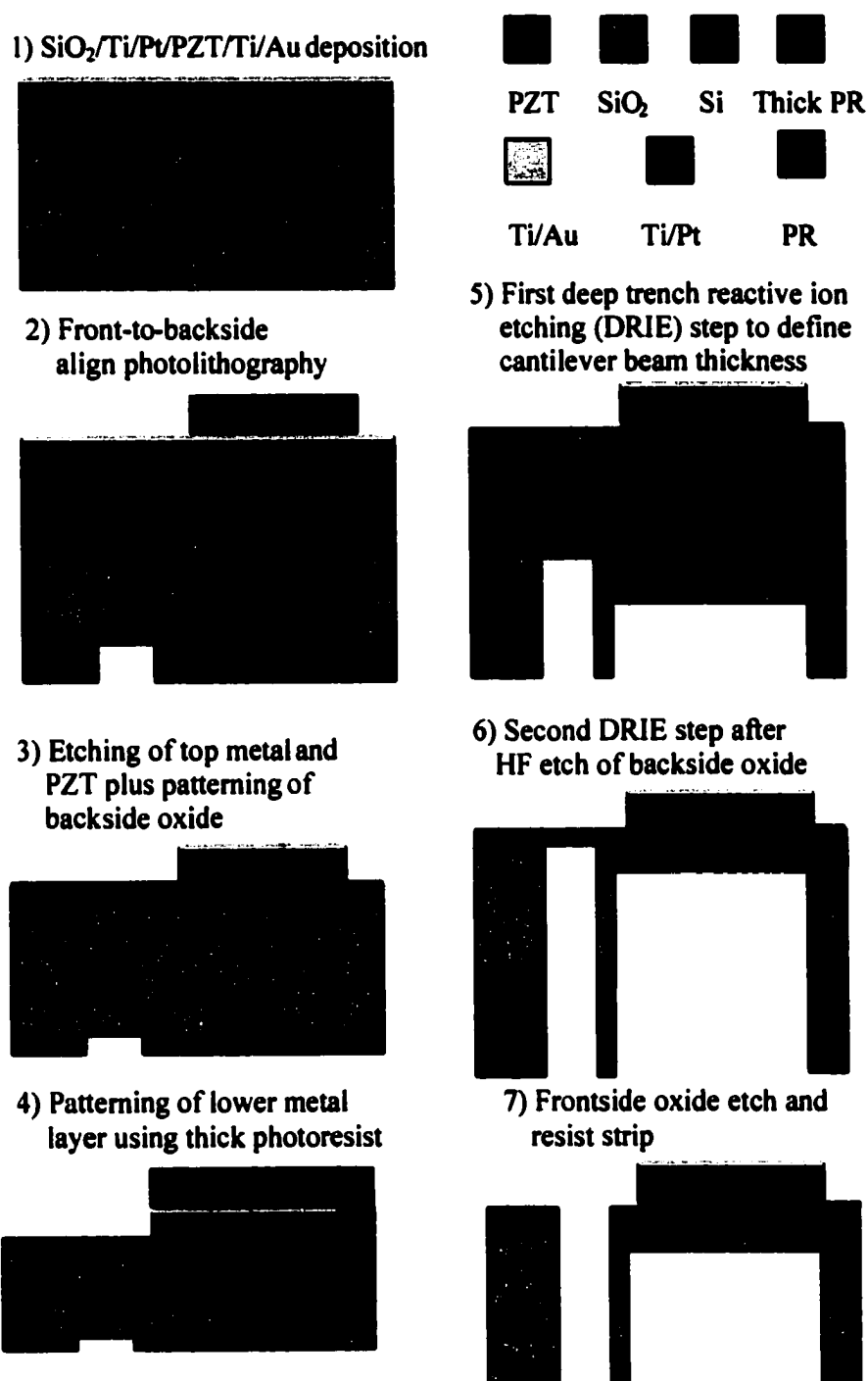


Figure 3.14: Fabrication Process flow of PZT MEMS accelerometers

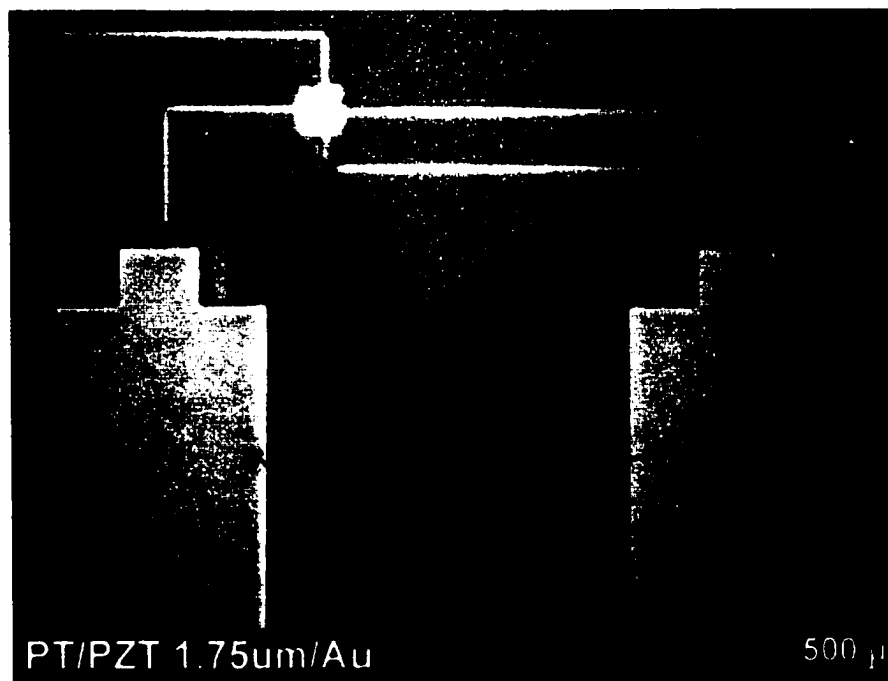


Figure 3.15: Frontside process: patterned top electrode/PZT and bottom electrode



Figure 3.16: SEM graph showing one of the cantilever beam and proof mass of the accelerometer; the tapered profile resulted from heating and loading effects

Chapter 4

MEMS Accelerometer Design II: Trampoline and Diaphragm Structures

In this chapter, two types of sensing structures, trampoline and diaphragm, were investigated for the second generation of PZT MEMS accelerometers. Their design, models, and fabrication processes were studied and compared to the first generation.

4.1 Device Design and Modeling of Trampoline-type Accelerometers

4.1.1 Device Structure and Design

The structure of the trampoline design consists of four co-joined beams with a proof mass at the juncture. *Figure 4.1* shows the schematic of the accelerometers. It is fully symmetrical about the x and z axes; therefore, there is ideally no sensitivity to transverse accelerations in these directions. The stress distribution on each beam will be derived in section 4.1.3. The stress is a maximum at the fixed end ($x=0$) and linearly decreases to zero at the middle of the beam; then it linearly increases in the opposite sign to another maximum at the end with the proof mass ($x=L$). Therefore, top electrodes at the outer (fixed end) and inner sides of the beams need to be separated from each other in order to avoid cancellation of piezoelectric charges generated from the PZT films. In this design, the PZT films on the inner and outer sides of the beams are poled in different

directions; therefore, the charges generated from these two areas can be added when they are connected in parallel. One advantage of having a beam with opposite polarities in separate areas is cancellation of the charges generated from thermal excursions. Since PZT is pyroelectric, temperature changes also generate charge. However, PZT films on the inner and outer sides of the beam are poled in opposite directions and the electrodes are connected in parallel. Thus, the pyroelectric charges will be cancelled because they are of opposite signs.

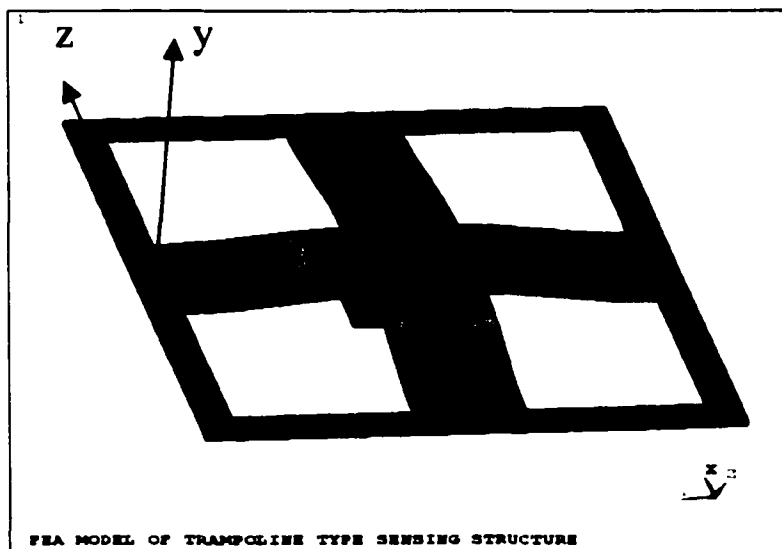


Figure 4.1: Schematic of a trampoline-type accelerometer

Three different sizes of trampoline-type accelerometers were designed here to study the relationships between sensitivity and resonant frequency; their dimensions are listed in *Table 4.1*.

Table 4.1: Dimensions of the trampoline-type accelerometers

Device type	Silicon beam: length*width (mm * mm)	Inner electrode: length *width (μm * μm)	Outer electrode: length *width (μm * μm)	Sensor Capacitance (nF)
I	1.1 * 0.8	350 * 730	350 * 730	4.02
II	1.3 * 0.8	450 * 730	450 * 730	4.87
III	1.7 * 0.8	650 * 730	650 * 730	6.57

Note:

- 1) The average thickness of the silicon beams were 40 μm and 60 μm for two different wafers
- 2) The length, width, and thickness of the proof mass are 800, 800, and 450 μm
- 3) The capacitance calculation is based on the PZT thickness of 6 μm and a dielectric constant of 1000

MEMS accelerometers will be integrated with application specific integrated circuit (ASIC) amplifiers for future smart sensor applications. Therefore, the capacitance of the MEMS accelerometers is constrained by the need for compatibility with the ASIC. For example, if the ASIC gain-bandwidth (GBW), which is the product of the amplifier's gain and bandwidth, is designed at 1MHz (see *Figure 4.2*), then for a desired bandwidth of 20kHz, the maximum gain is 50. The feedback capacitance of the ASIC amplifier designed by Wilcoxon Research for the MEMS accelerometers is 105.6 pF. As a result, the maximum capacitance of the MEMS accelerometer can be calculated from Eq. 1.5, and is 5.28 nF. If the entire beam area is covered with top electrodes (with a PZT thickness of 6 μm and dielectric constant of 1000), the capacitances are 5.88, 6.74, and

8.46, which are all larger than 5.28 nF. In order to solve this problem, the top electrodes are only placed on the highly stressed areas, which are close the frame for the outer electrode and close to the proof mass for the inner electrode. Therefore, the capacitance of MEMS accelerometers can be reduced to the desired value without significantly reducing the sensitivity. The capacitances for different sizes of the trampoline-type accelerometers are available in *Table 4.1*.

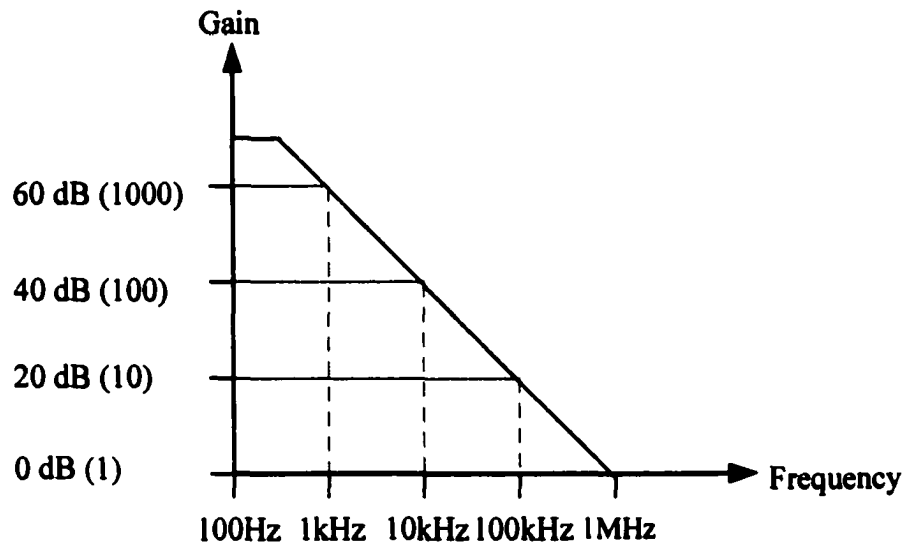


Figure 4.2: Gain-bandwidth (GWB) of an ASIC amplifier

4.1.2 Derivation of Structure Dynamics

Since the trampoline structure is fully symmetrical, modeling one beam with one-fourth of the proof mass is sufficient to describe the dynamics of the whole structure.

The structure for the modeling and the boundary conditions are shown in *Figure 4.3*.

Euler-Bernoulli beam theory is again used to describe the equation of motion of the beam (Eq. 3.1). At the fixed end ($x=0$), the boundary conditions are the same as Eq. 3.2. At the end with the proof mass ($x=L$), the shear force equals the inertial force provided from the proof mass as expressed in Eq. 4.1. The slope at this end is zero because the trampoline structure is symmetrical in the x direction. This provides another boundary condition (Eq. 4.2).

At the end with the proof mass ($x=L$), the boundary conditions are:

$$EI \frac{\partial^3 u(L,t)}{\partial x^3} = \frac{M_0}{4} \times \frac{\partial^2 u(L,t)}{\partial t^2} \quad (4.1)$$

$$\frac{\partial u(L,t)}{\partial x} = 0 \quad (4.2)$$

Using the same procedure (the separation of variables method) as described in the section 3.2.2, the time-independent boundary conditions can be determined. At the fixed end ($x=0$), the boundary conditions are

$$\begin{cases} y(0) = 0 \\ \frac{dy(0)}{dx} = 0 \end{cases} \quad (4.3)$$

At the end with the proof mass ($x=L$), the boundary conditions are

$$\left\{ \begin{array}{l} \frac{dy(L)}{dx} = 0 \\ -EI \frac{d^3 y(L)}{dx^3} = \frac{M_0 \omega^2 y(L)}{4} \end{array} \right. \quad (4.4)$$

Applying these four boundary conditions (Eq. 4.3 and 4.4) to the solution of the equation of motion (Eq. 3.8), a matrix can be obtained (Eq. 4.5):

$$\begin{bmatrix} 0 & 1 & 0 & 1 \\ 1 & 0 & 1 & 0 \\ \cos \beta L - \cosh \beta L & -\sin \beta L - \sinh \beta L & 0 & 0 \\ \frac{M_0}{4m} \beta \sin \beta L - \cos \beta L & \sin \beta L + \frac{M_0}{4m} \beta \cos \beta L & 0 & 0 \\ -\frac{M_0}{4m} \beta \sinh \beta L - \cosh \beta L & -\sinh \beta L - \frac{M_0}{4m} \beta \cosh \beta L & 0 & 0 \end{bmatrix} \times \begin{bmatrix} C_1 \\ C_2 \\ C_3 \\ C_4 \end{bmatrix} = \begin{bmatrix} 0 \\ 0 \\ 0 \\ 0 \end{bmatrix} \quad (4.5)$$

Following the same procedures as described in section 3.2.2, the eigenvalue (β_n), resonant frequency (ω_n), and the eigenfunction (ϕ_n) corresponding to each mode of the trampoline structure can be obtained. The eigenvalue and eigenfunction are plotted in *Figure 4.4* and *Figure 4.5* respectively.

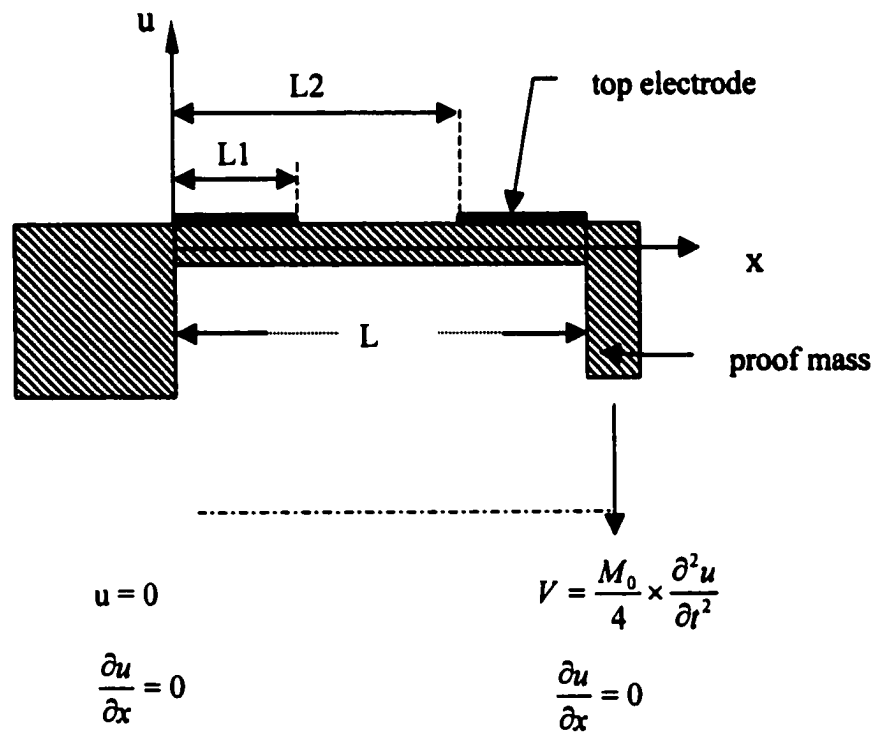


Figure 4.3: Boundary conditions for the trampoline-type beam

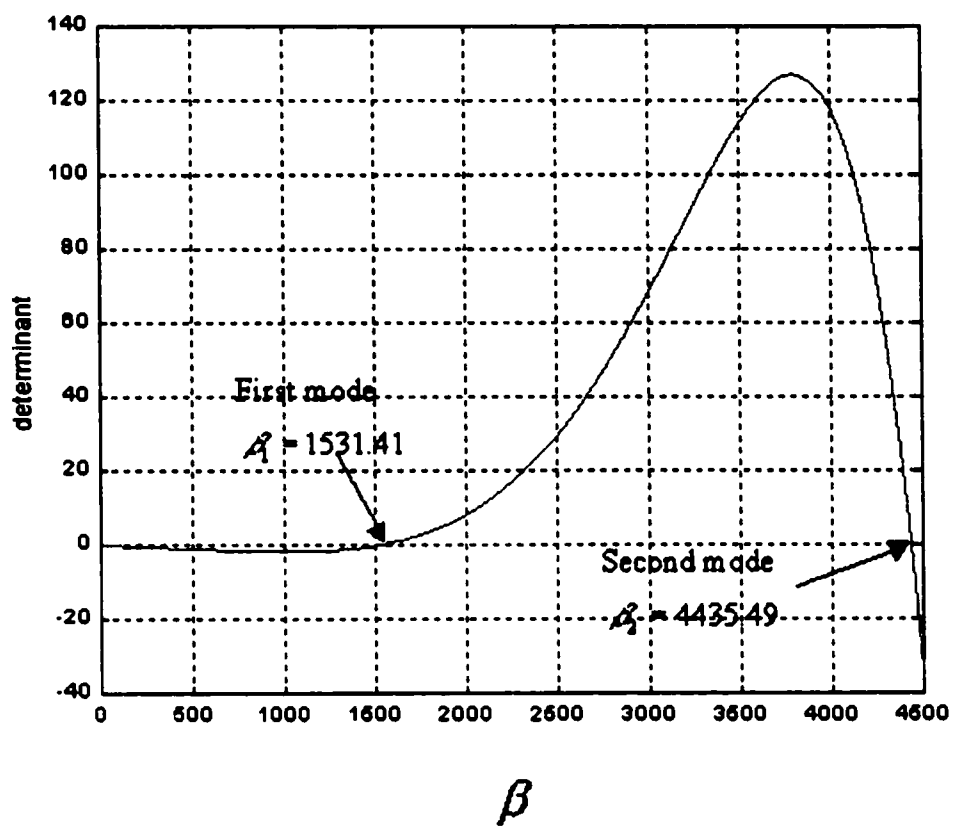


Figure 4.4: Eigenvalues corresponding to the first and second modes of the trampoline structure

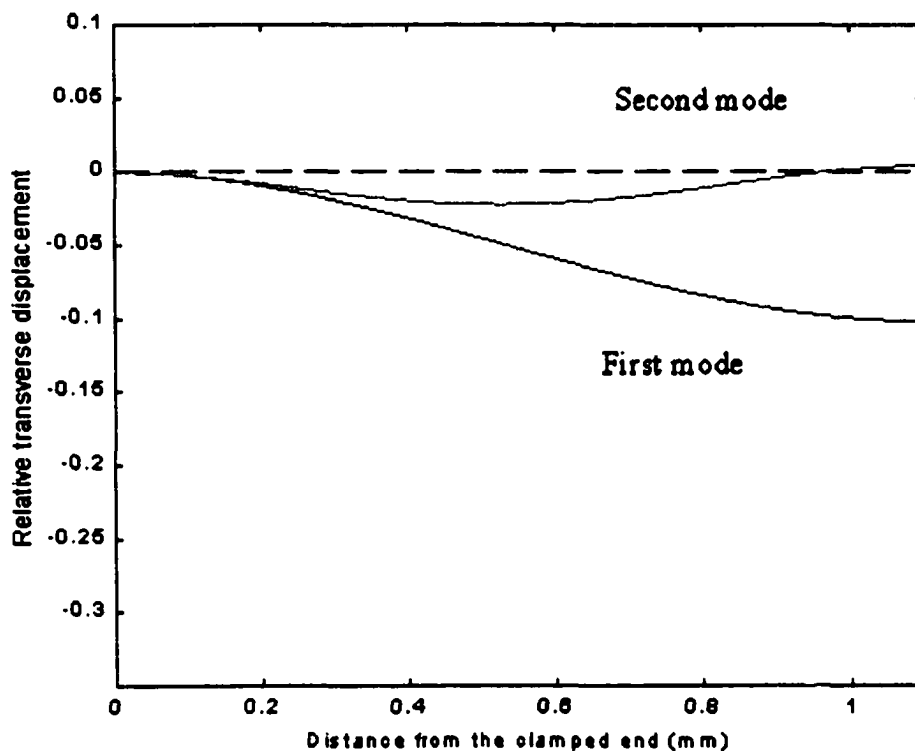


Figure 4.5: First and second mode shapes of one arm of the trampoline structure; beam length is 1.1 mm

4.1.3 Analytical Solution of Charge Sensitivity

The bending moment (M) and normal stress (σ_x) on the beam can be calculated by Eq. 3.16 and Eq. 3.17 respectively, following the procedure described in section 3.2.3. The distribution of the normal stress in the middle of the PZT layer along the x-axis is

plotted in *Figure 4.6*. The total charge can be obtained by integrating over the inner and outer top electrodes (Eq. 4.6),

$$Q = \int_{L_2}^{L_1} \sigma_x \cdot d_{31} \cdot b_m \cdot dx - \int_{L_2}^{L_1} \sigma_x \cdot d_{31} \cdot b_m \cdot dx \quad (4.6)$$

where L_1 and L_2 are indicated in *Figure 4.3*.

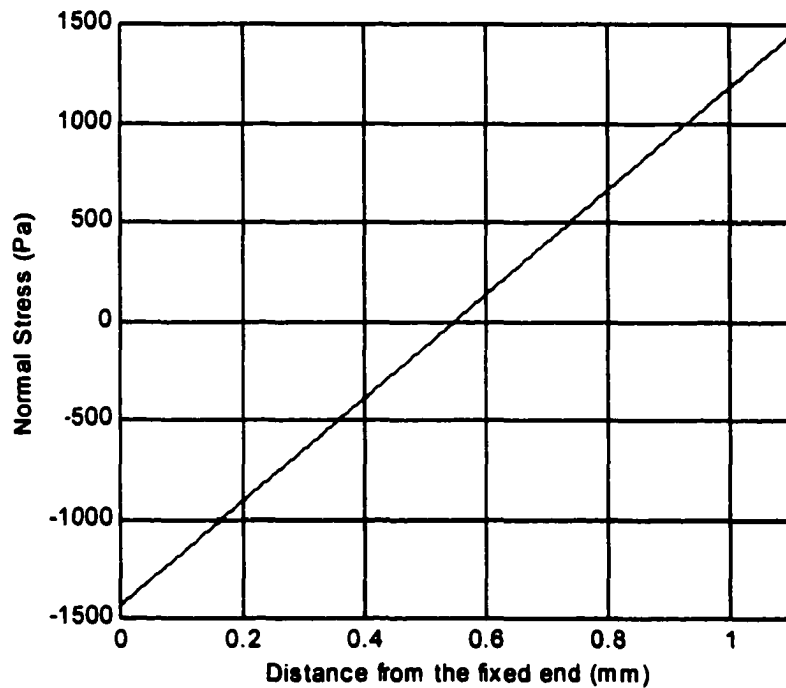


Figure 4.6: The distribution of the normal stress in the middle of the PZT layer under one g acceleration; beam length is 1.1 mm

4.2 Device Design and Finite Element Analysis (FEA) Model of Diaphragm-type Accelerometers

4.2.1 Device Structure and Design

Another structure for the second-generation MEMS accelerometers is the annular design. It consists of an annular diaphragm with an annular proof mass at the center of the diaphragm. Since it is totally symmetrical, half of the structure is sufficient for modeling. This is shown schematically in *Figure 4.7* for the FEA simulation. The polar coordinate system is used here to facilitate description of the structure. In this 3-D structure, both radial stresses (σ_r) and tangential stresses (σ_θ) contribute to the d_{31} piezoelectric charges.

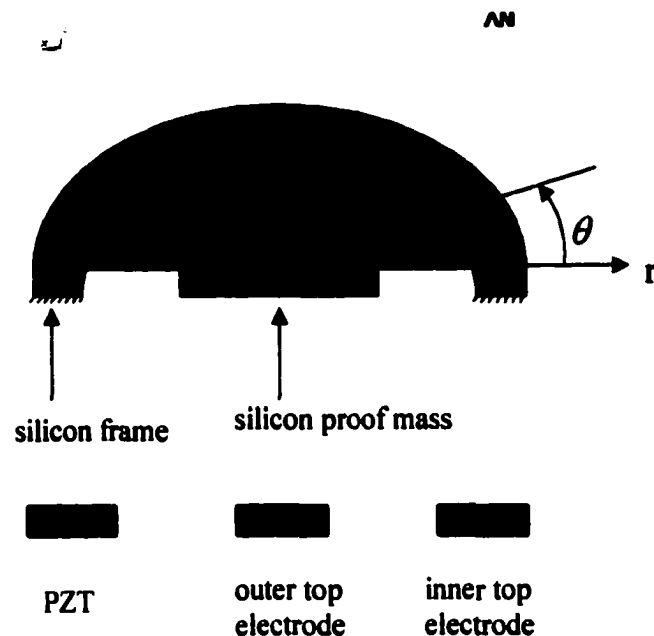


Figure 4.7: Schematic showing half of the diaphragm accelerometer

4.2.2 FEA Simulation using ANSYS software

Finite element analysis (FEA) using ANSYS software was utilized to model the structure. The stress distribution along the radial direction under a one g acceleration in the z direction (out of plane) is plotted in *Figure 4.8*. Like the trampoline structure, the stresses are of opposite signs for the outer (i.e. the side close to the frame) and inner sides of the diaphragm. Therefore, the top electrodes are separated on the inner and outer sides of the diaphragm and are placed only on the most highly stressed area for the same reasons as the trampoline accelerometer. In addition, the resonant frequency was calculated from the ANSYS simulation. Two different sizes of accelerometers were designed and their dimensions are shown in *Figure 4.9* and *Table 4.2*. The width of the inner and outer electrodes is adjusted to have the same area. Therefore, the temperature excursion effect can be minimized as described in Section 4.1.1.

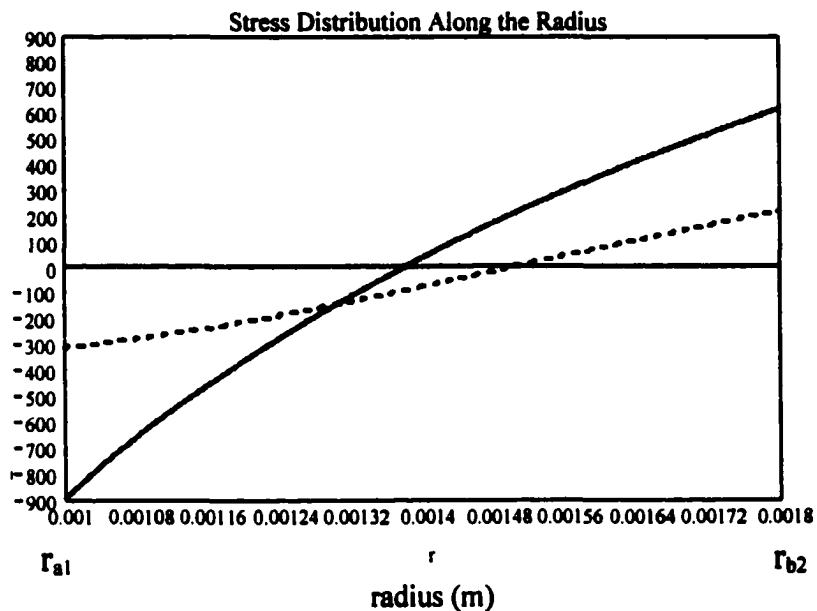


Figure 4.8: Stress distribution of a diaphragm accelerometer along the radial direction; the solid line is radial stress and the dashed line is tangential stress

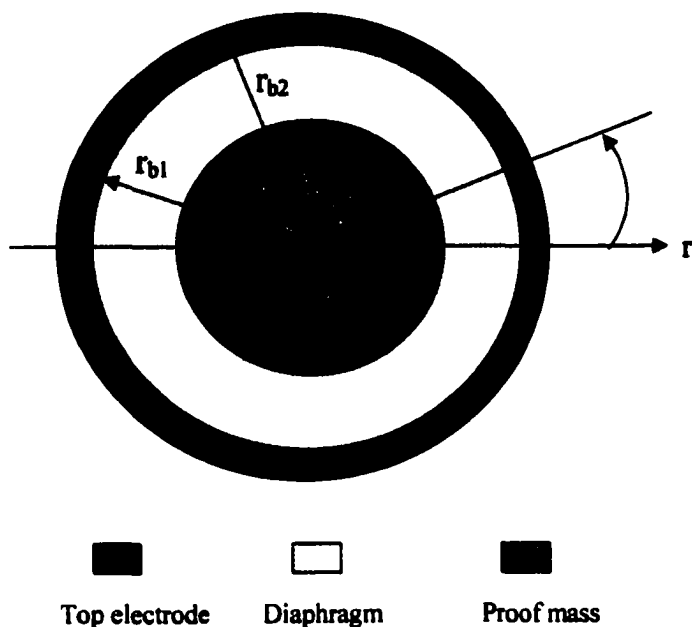


Figure 4.9: Top view of the diaphragm accelerometer showing the definitions of the dimensions

Table 4.2: Dimensions of diaphragm accelerometers

Device type	r_{a1} (μm)	r_{a2} (μm)	r_{b1} (μm)	r_{b2} (μm)	Capacitance (nF)
I	1000	1280	1620	1800	6.18
II	1000	1256	1850	2000	5.73

Note:

- 1) The average thickness of the silicon diaphragms are 40 μm and 60 μm for two different wafers
- 2) The thickness of the proof mass is 450 μm
- 3) The capacitance calculation is based on a PZT thickness of 6 μm and dielectric constant of 1000

The total charge output (sensitivity) can be obtained from Eq. 4.7.

$$\int_0^r \int_{\theta_1}^{\theta_2} 2 \cdot (\sigma_r + \sigma_\theta) \cdot d_{31} \cdot dr \cdot d\theta - \int_0^r \int_{\theta_1}^{\theta_2} 2 \cdot (\sigma_r + \sigma_\theta) \cdot d_{31} \cdot dr \cdot d\theta \quad (4.7)$$

4.3 Process Development

As discussed in Chapter 3, there were some problems and issues in the initial fabrication runs. Therefore, improved fabrication processes were developed and are discussed in the following section.

4.3.1 Photomask Design

Both trampoline-type and diaphragm-type accelerometers were designed on the same photomask set; in addition, some test patterns were included as well. *Figure 4.10* shows their arrangement on the whole mask set. The important features and modifications are described in the following:

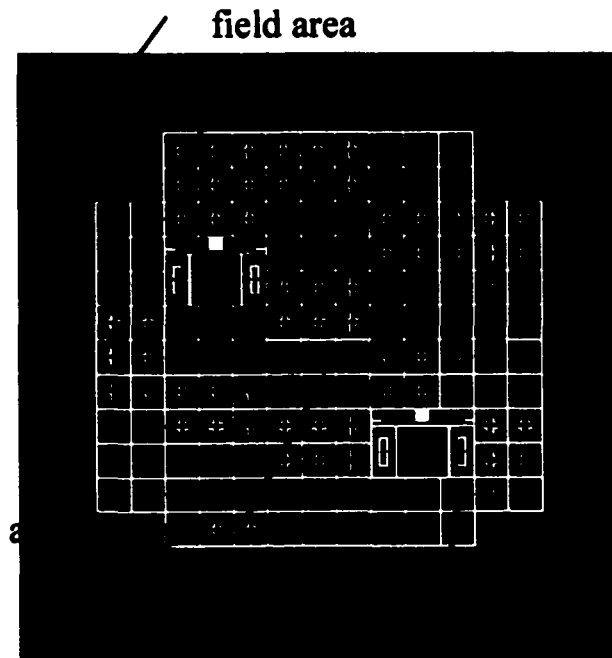


Figure 4.10: The second photomask set includes trampoline-type, diaphragm-type accelerometers and testing patterns

Five photomask levels, which is one more than the previous design, were used. The top electrode and the PZT layers were defined in the same photomask as in the previous processes. Since the undercutting of PZT films is about 2 to 1 (lateral to

thickness) as described in Section 2.2.5, the top metal sometimes contacted the bottom electrode along the sidewall of the etched area (see *Figure 4.11*) causing an electrical short. Therefore, two photomask levels with bias ($15\mu\text{m}$ for the trampoline design) between them were used to separately define the PZT and top electrode layers. The percentage of the occurrence of electrical shorts was reduced from 50% with the first design to 10% with the second design.

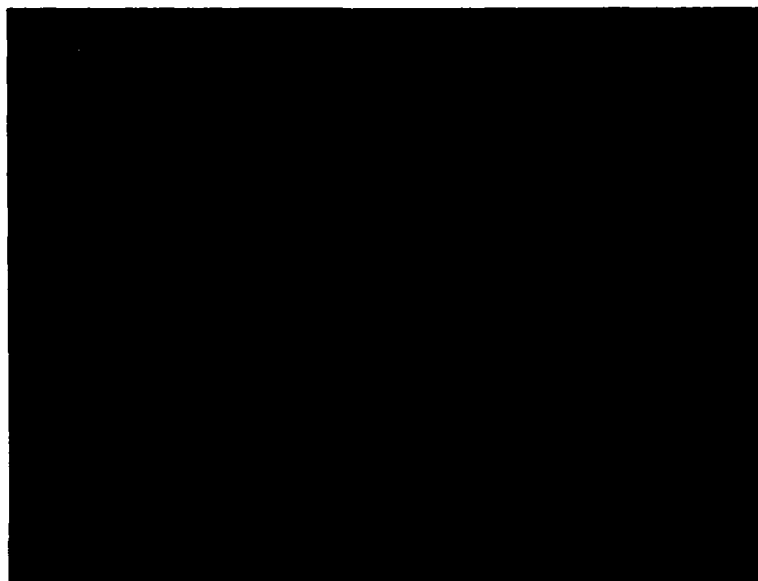


Figure 4.11: SEM showing contact of top and bottom electrodes causing an electrical short

In order to effectively use the wafer area, the size of each die was shrunk from 10 mm square in the first design to 6mm square in the second design. The total number of dies on a 4" wafer increased from to 44 to 114. This was mainly achieved by reducing

the frame area, which is non-functional. Therefore, the performance of the devices is not affected while the utilization of a wafer is enhanced.

During the first-design fabrication runs, chemical loading during deep-trench reactive ion etching (DRIE) step was observed because the area exposed to the plasma was too large (~53%). To prevent this, two modifications to the design of the DRIE mask level were made. First, the etched through area of the trampoline design was reduced with the configuration shown in *Figure 4.12*. This reduces the exposed area, while the performance of accelerometers is not affected. Second, the field area of the photomask, which is defined as the area outside the die area (indicated in *Figure 4.10*), was designed as a dark field to reduce the exposed area even more. With these adjustments, the exposed area was reduced to ~24%. The loading effect was avoided with this new design and the results will be shown in Section 4.3.4.

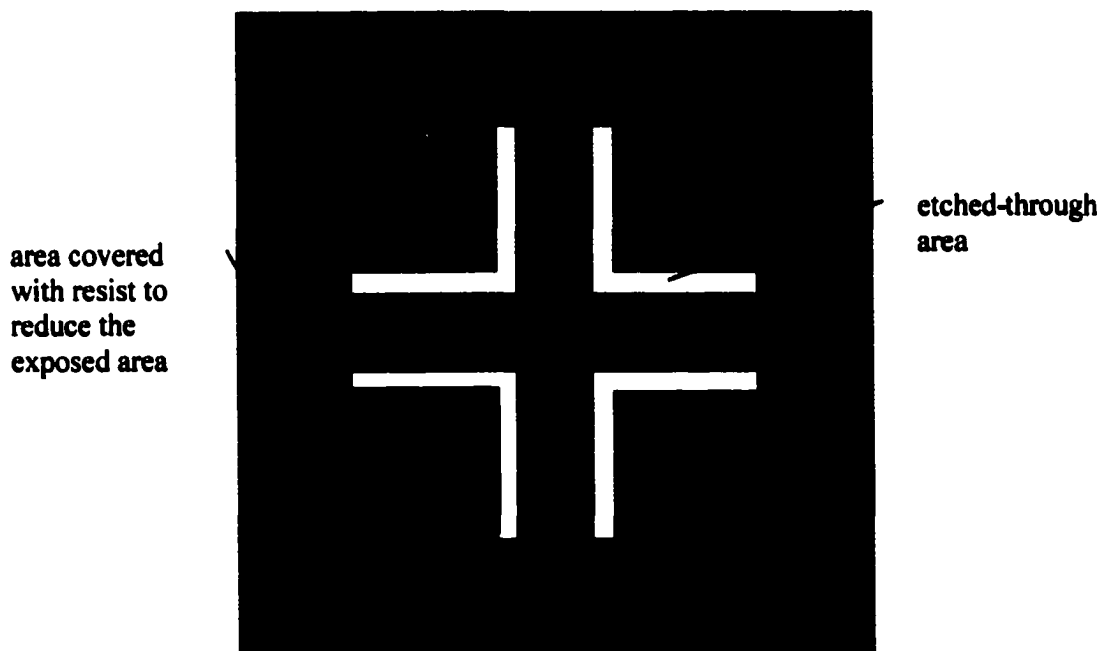


Figure 4.12: Etched through area of the trampoline design

Three types of testing patterns were also designed in the photomask set for the purposes of process monitoring and film characterization. For process monitoring, patterns for the end-point detection of silicon oxide etching and for the accuracy of front-to-backside alignment were designed. The pattern for the end-point detection enabled measurement by ellipsometer to ensure the complete etching of silicon oxide without over etching. Thus, the silicon beam area can be better defined. An etched through hole is designed to measure the accuracy of the front-to-backside alignment using the mechanical jig; *Figure 4.13* shows the designed pattern. The misalignment between the etched through hole and the patterned bottom metals can be measured using microscopy. It shows the misalignment of 9.5 μm in the x direction and 17.5 μm in the z direction, which as described before is about the best resolution for the mechanical assembly.

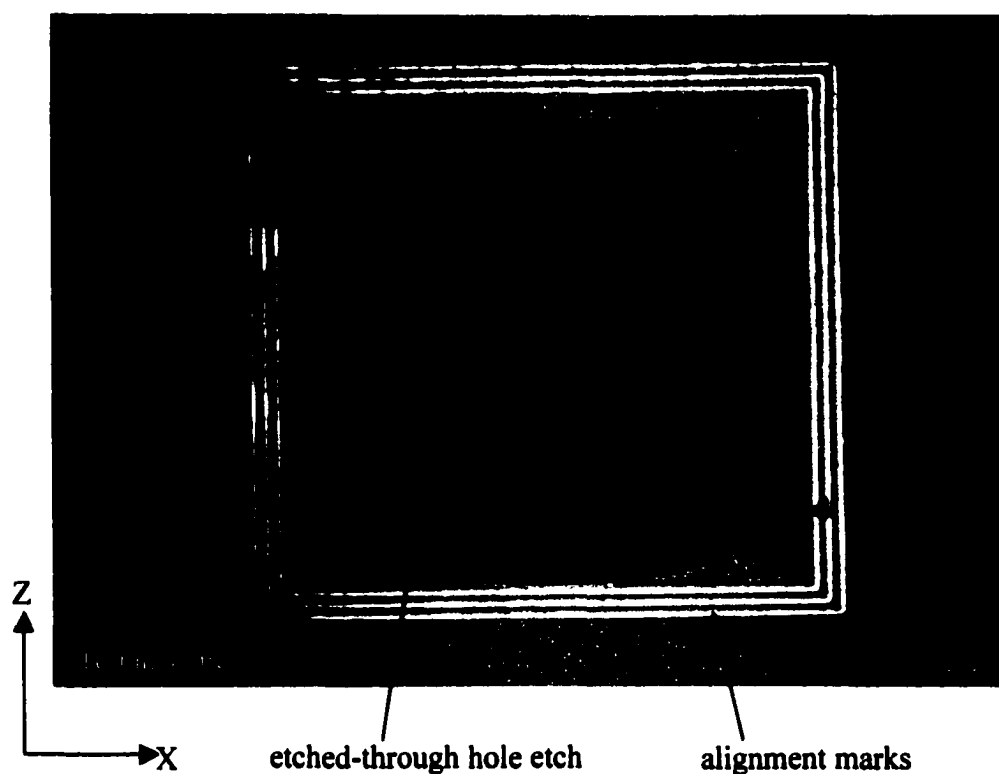
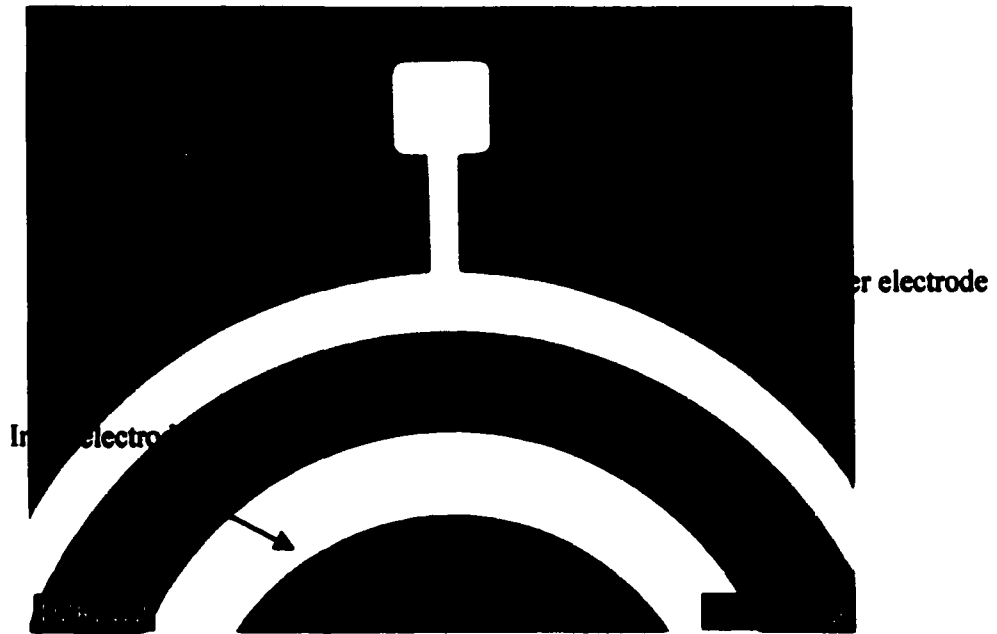


Figure 4.13: The accuracy of front-to-backside alignment using the mechanical jig was measured from this pattern; the misalignment is $9.5 \mu\text{m}$ in the x direction and $17.5 \mu\text{m}$ in the z direction, typical for this jig

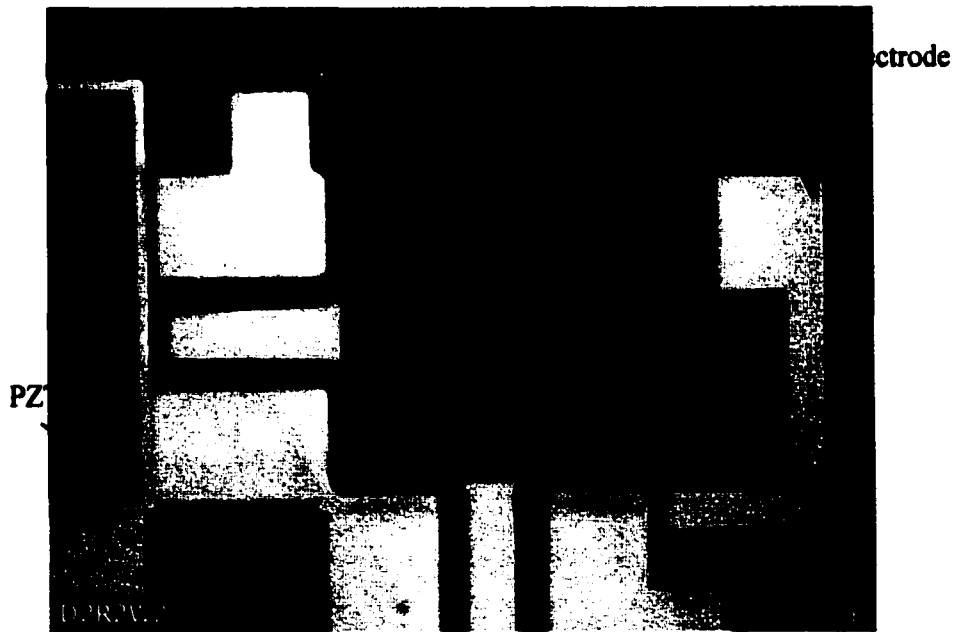
The sensitivity of the accelerometer is proportional to the piezoelectric constant of the PZT films (d_{31}); therefore, measurement of the piezoelectric constant on the device wafer leads to a more accurate theoretical calculation of the accelerometer sensitivity. Thus, a pattern was designed for the measurement of the piezoelectric constant. The measurement procedure and results were discussed in Section 2.3.3.

4.3.2 Metallization

The top electrode metallization scheme for the previous fabrication utilized Ti (8nm) and Au (80nm). Al, Cr, Ti, and Zr are the four film metals usually used to improve adhesion between an oxide surface and other metals because they form strongly bonded surface oxides [83]. However, it was found that Ti is easily attacked by HF and HF is used in the first-step of PZT etching. As a result, some of the top electrodes delaminated after the PZT etching. The adhesion layer was switched from Ti to Cr, since Cr was found to have a better adhesion with Au and better resistance to HF than Ti. In addition, better adhesion of top electrodes is important for the wire-bonding step during the device packaging, since poor adhesion presents one of the failure mechanisms for the wire-bonding step. The improved metallization of the top electrodes is shown in *Figure 4.14*.



(a)



(b)

Figure 4.14: The improved metallization of the top electrodes for (a) diaphragm type and (b) trampoline type accelerometers

4.3.3 Backside Processing

Previously, the backside oxide layer was also etched during the first step of the PZT etching. However, the relatively longer etching time for the first-step PZT etching (due to the thicker PZT films) caused over-etching of the backside oxide layer. As a result, the silicon beam dimensions were changed. In this run, these two etching steps were separated to have a precise etching time for each step. *Figure 4.15* shows improved backside processing including the well patterned silicon oxide and thick photoresist layers.

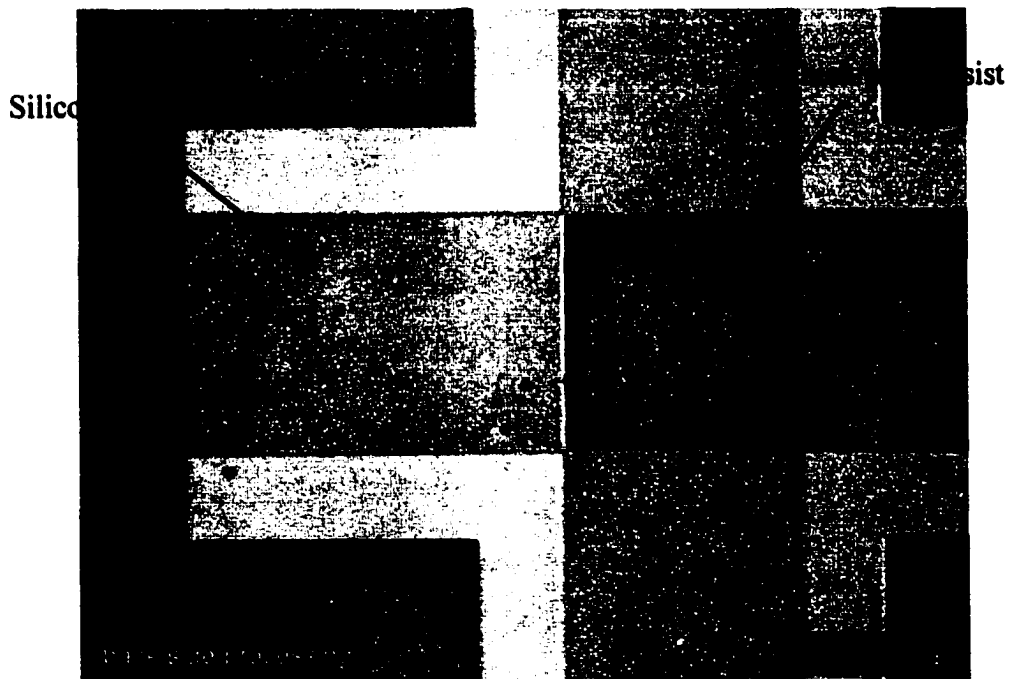
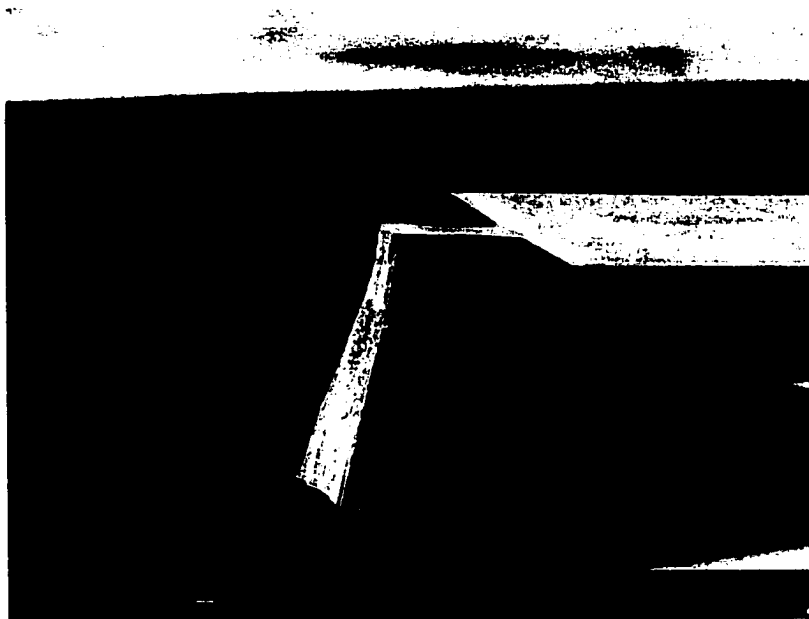


Figure 4.15: The improved backside processing including the well patterned silicon oxide and thick photoresist layers

4.3.4 DRIE

Both commercial DRIE etchers from Surface Technology Systems, Ltd. (STS) and Plasma Therm, Inc. (PTI) were used in fabricating the second-generation accelerometers. One significant difference between these two etchers is the wafer holder. The STS etcher uses electrostatic force to hold the processing wafer. Therefore, a carrier wafer is needed as described in Section 3.3.6, since the MEMS accelerometers are etched through. The heating (therefore, selectivity) problem, observed in the previous fabrication, was improved by taking a five-minute break for each ten-minute etch. For the PTI etcher, an alumina clamp was used to mechanically hold the wafer on the edge; therefore, no carrier is needed. The wafer cooling is more effective and no heating problem was observed.

The etched profile of the proof mass was greatly improved because chemical loading was prevented with the new mask design as described in section 4.3.2. The sidewall profiles improved from 45° to 83° for the first and second designs respectively (see *Figure 4.16*). This results in better control of the performance of the accelerometers.



(a)



(b)

Figure 4.16: Etched profiles of the proof mass for first (a) and second-generation (b) accelerometers; the proof mass in (b) was cut from its supporting trampoline structure

Variations in the thickness of the silicon beams and diaphragms will significantly affect the sensitivity and resonant frequency of the accelerometers. Therefore, a uniform DRIE etch rate over a 4" wafer is desirable to have a better control over the thickness of the silicon beams and diaphragms. Furthermore, well controlled etch rates are necessary, as a small variation of the etch rate will result in a large variation in the thickness after a long etching time. For example, a variation of 6% in the etch rate will cause a variation of 27 μm in the thickness, when a 450 μm thick silicon wafer is etched through. Compared to the designed silicon thickness, 40 μm and 60 μm , and the optimized silicon thickness, 2.8 μm (described in section 3.2.4), the 27 μm variation is relatively large. This will significantly reduce the controllability of device performance over a 4" wafer.

However, a very uniform etch rate is difficult to obtain in DRIE etchers. Many parameters affect the etching rate uniformity such as temperature uniformity, the geometric arrangement of the power coil and the gas feed schemes, feature density (locally exposed area to plasma) and local rates of plasma density formation and loss. The etching rate uniformities for the STS and PTI etchers were measured and are shown in *Figure 4.17*. In this case, the rf power coil arrangement of the ICP etcher has the dominant effect [81]. The etch rate is higher on the periphery of the wafer because the plasma density is higher at this area, which is closer to the rf power coil. Another important observation found was that the lower etch rate benefits uniformity [81]. This is because the higher etching rate increases the difficulty in transporting etched products; as a result, a non-uniform concentration is formed over the wafer. Therefore, the ion flux

and neutral reactants are non-uniform over the surface, causing the non-uniform etch rates. It is evident that non-uniformities are 20.18% (STS etcher), 7.34% (PTI-1), and 5.43% (PTI-2) for the average etching rates of 2.28, 1.50, and 1.29 $\mu\text{m}/\text{minute}$ respectively.

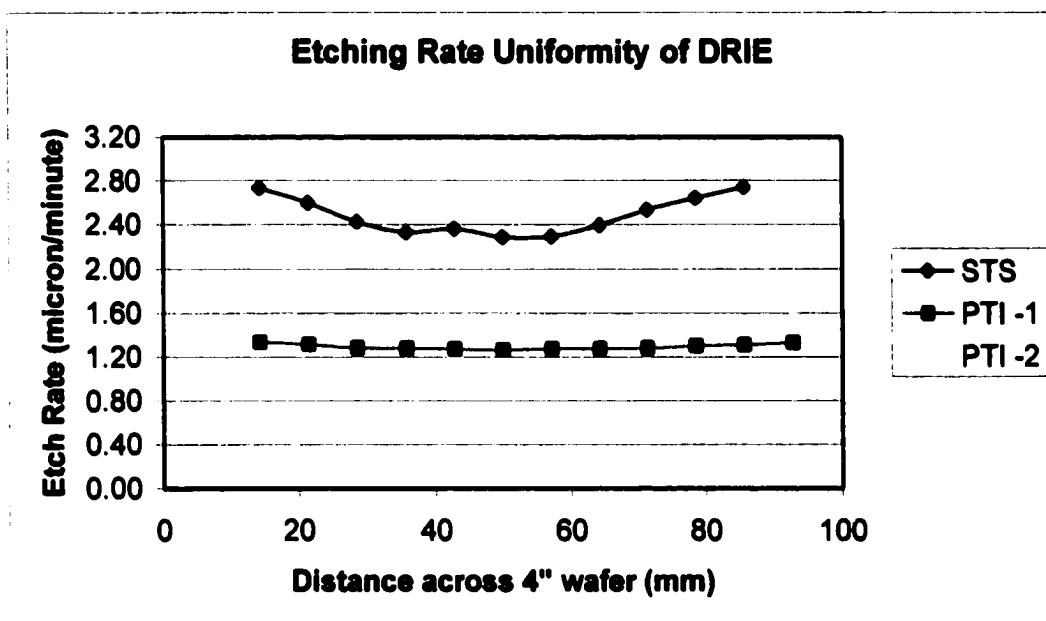


Figure 4.17: Etching rate uniformity over 4" wafers for STS and PTI etchers; the higher etching rate results in a higher non-uniformity

4.3.5 Processing Procedures

The fabrication procedures of the second-design accelerometers were improved from the procedures of the first design. The entire procedure integrating the improved processes is described in the following.

The PZT MEMS accelerometers of the second design were fabricated using five photomask levels including a front-to-backside alignment step. The five photomask levels include: a top electrode pattern (referred to herein as M2), a PZT etch mask pattern (PZT), a bottom electrode pattern (M1), and two backside beam definition patterns (B1 and B2) which form the trampoline and diaphragm structures. The fabrication process flow is shown in *Figure 4.18*.

The starting substrate was a 4-inch diameter, n-type <100> (1-10 Ω -cm), double-side-polished silicon wafer. After standard RCA cleaning and native oxide etch, an 800 nm thermal oxide was grown on the wafers, followed by the sputter deposition of a low-stress Ti (20 nm)/Pt (150 nm) lower metallization layer. A $\sim 6\mu\text{m}$ thick blanket PZT was deposited by a sol-gel process. Following the PZT deposition, the top metallization layers of Cr (8nm) and Au (80nm) were deposited via thermal and electron-gun evaporation, respectively. The first photolithography step was a front-to-backside alignment (masks M2 and B2) as described in section 3.3.2.

After development, the top Au layer was then wet etched using a gold etchant (Transene Inc., Danvers MA). Using the same mask layer, the Cr was etched using a mixture of 6% HNO_3 :16%(NH_4) $\text{Ce}(\text{NO}_3)_6$:78% H_2O (Transene Inc., Danvers MA). The backside oxide was reactive ion etched (RIE) using a CF_4/O_2 mixture (45:5 sccm) at 100mTorr and 150W (resulting in a 220V DC self-bias).

After stripping the photoresist on both sides, the backside of the wafer was spin-coated with photoresist to protect the already patterned silicon oxide during the subsequent PZT etching step. After another photolithography step (using the PZT mask),

the two-step wet etch process was utilized to pattern the thick PZT layer as described in Section 2.2.5.

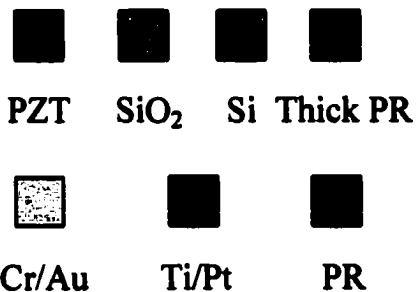
After PZT etching, the front side of the wafer was then patterned using the M1 mask followed by the RIE of lower Ti/Pt electrode layers. A subsequent oxygen plasma ashing step was used to remove the photoresist. At this point, the frontside processing was finished.

Thick resist photolithography (B1 mask) was utilized to define the die frames, diaphragms, and proof masses of the trampoline structures. A 13 μm thick AZ4620 photoresist, which can be obtained at a spin speed of 1500rpm, was used. Before the DRIE steps, the frontside of the wafer was spin coated with Shipley 1813 photoresist to protect the films during the oxide etching between the two DRIE steps. The first DRIE step was used to define the thickness of the beams and diaphragms. Two wafers were etched in the Plasma Therm ICP770 etcher for 24 and 40 minutes and an etched depth of $40 \pm 1.5 \mu\text{m}$ and $60 \pm 2 \mu\text{m}$ was obtained, respectively. After defining the beam and diaphragm thickness, BOE was used to remove the patterned oxide on the beam areas, after which a second DRIE step was used to etch through the wafers (visual endpoint detection).

After DRIE steps, the frontside oxide was removed from the backside of the wafer by another RIE step. The final step was photoresist stripping. In the previous fabrication, the photoresist on the front of the wafer was burned during the DRIE steps, since wafer cooling was not effective when using a carrier wafer. Therefore, it took a long time to strip the resist using a combination of oxygen plasma ashing and a Pirhana

etch ($5\text{H}_2\text{SO}_4:\text{H}_2\text{O}_2$). The metal traces of the bottom electrode were attacked during the Pirhana etch and this caused electrical open circuits. To avoid this problem, a new base-type stripper, ACT935 resist stripper (Ashland Chemical Company, Covington KY), with a composition of 55% $\text{HOCH}_2\text{CH}_2\text{NH}_2$, 20% NH_2OH , 5% $\text{C}_6\text{H}_4(\text{OH})_2$, and 20% H_2O (all in weight percent), was used. This solution is preferred since the top and bottom electrode metals have a better resistance to this chemical composition than the Pirhana etch. *Figure 4.19* shows a diaphragm-type accelerometer after finishing the processing steps. After the final resist-strip step, the accelerometers were ready for packaging and testing.

1) SiO₂/Ti/Pt/PZT/Ti/Au deposition



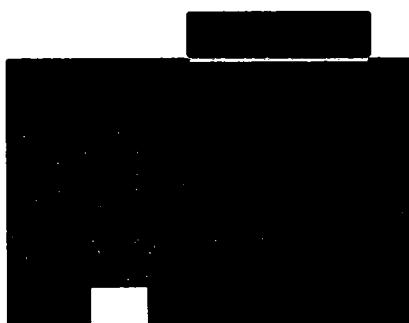
2) Front-to-backside align photolithography



4) Dry etch of backside silicon oxide using CF₄ and O₂ plasma



3) Top electrode (Cr/Au) etch



5) Etching of thick PZT films; backside was coated with photoresist

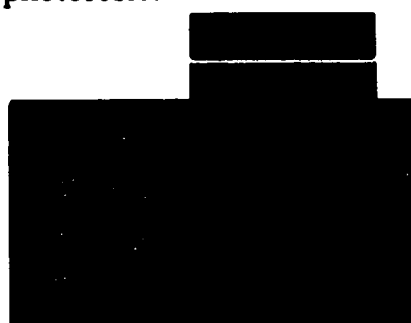


Figure 4.18: Fabrication process flow for second-generation MEMS accelerometers

6) Patterning of bottom electrode using RIE (Cl_2 plasma); thick photoresist was used to provide better step coverage



8) Second DRIE step after HF etch of backside oxide



7) First DRIE step to define beam or diaphragm thickness



9) Frontside oxide etch and resist strip

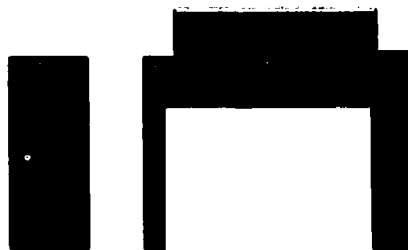


Figure 4.18: Fabrication process flow (continued)



Figure 4.19: A diaphragm-type accelerometer compared to a penny after finishing the processing steps

Chapter 5

Characterization of MEMS Accelerometers

5.1 Frequency Response Measurement

The frequency response of the accelerometers will be described first since it is of interest for most vibration applications. A description of the measurement principle will be introduced, followed by the equipment setup and measurement procedure.

5.1.1 Introduction

There is a direct linear relationship between the input and output for any linear system. In the time domain, the relationship is determined by the system impulse response function, $h(t)$, using the convolution integral of Eq. 5.1 [79]. For the accelerometer case, the input is the initial force (P) or acceleration and the output is the piezoelectric charge (Q) or voltage output.

$$Q(t) = \int P(\xi) * h(t - \xi) d\xi \quad (5.1)$$

This relationship is much simpler in the frequency domain. A Fourier transform of the output function, $Q(\omega)$, can be obtained easily from the product of the frequency response function, $H(\omega)$, and the Fourier transform of the input function, $P(\omega)$, as shown in Eq. 5.2.

$$Q(\omega) = H(\omega) \cdot P(\omega) \quad (5.2)$$

This is why most vibration problems are analyzed in the frequency domain instead of the time domain. Here, the dynamic frequency response of the accelerometers was measured to obtain their sensitivity, $H(\omega)$, and their resonant frequency. From Eq. 5.2, it is clear that both the applied force and the piezoelectric charge output need to be measured in order to calculate the sensitivity of the accelerometers. However, it is difficult to measure the absolute value of the applied force. Instead, a comparison measurement using a reference accelerometer was utilized. The frequency response measurement was done both at PSU and at Wilcoxon Research utilizing the same principles, but with different sample handling to verify the accuracy of the results. The equipment setup and measurement procedures at PSU are described in the following section.

5.1.2 Equipment Setup and Measurement Procedure

A schematic of the equipment setup is shown in *Figure 5.1*. An electromagnetic shaker (Wilcoxon F3), which has a usable frequency range of 25 – 10,000 Hz, was used

to mechanically excite the accelerometers in one direction as the applied force (or input acceleration). An aluminum plate, shown in *Figure 5.2*, designed to hold both MEMS and reference (Wilcoxon 736) accelerometers was screwed to the shaker. Thus, the applied force to both accelerometers should be the same. In addition, the aluminum plate was electrically grounded to shield the MEMS accelerometer from electromagnetic interference (EMI) from the shaker.

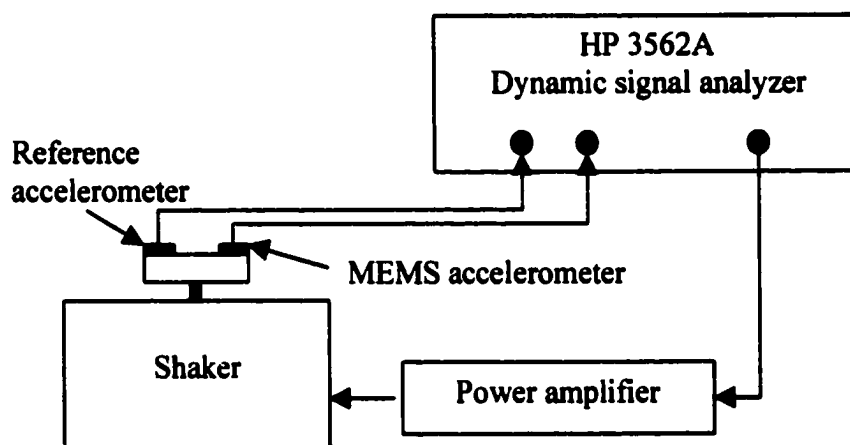


Figure 5.1: Schematic of the equipment setup for the frequency response measurement



Figure 5.2: Aluminum holder designed for frequency response measurement of the MEMS accelerometer sensitivity

Initially, the MEMS accelerometers were contacted using spring probes for the signal output. It was found that the contact force from the probes could introduce a large piezoelectric charge when the sample was driven mechanically by the shaker. Therefore, the charge sensitivity was artificially amplified. To solve this problem, bonding wires were used for the signal output. The MEMS accelerometer was glued to a ceramic substrate, which has screen-printed contact pads. Then the contact pads on the MEMS accelerometer were wire-bonded to the contact pads on the ceramic substrate. Finally, a co-axial wire was soldered to the ceramic substrate for the signal output.

The charge output of the MEMS accelerometer was connected to a charge amplifier with a 10 pF feedback capacitor (the configuration is shown in Figure 1.3).

Therefore, the amplification is 10 mV/pC. The reference accelerometer with a built-in charge amplifier has a voltage sensitivity of 100 mV/g and a first fundamental resonant frequency at 52 kHz. The outputs of both accelerometers (after-amplifier) were connected to a two-channel dynamic signal analyzer (HP 3562A). A sweep-sine signal, generated by the analyzer and then amplified by a power amplifier (Harmon/Kardon 330c), was used to drive the shaker. The output signals were acquired by the signal analyzer and analyzed using a transfer function measurement. Through this measurement, the voltage ratio of the MEMS accelerometer to the reference accelerometer was obtained. Therefore, the unknown applied force was cancelled as indicated in Eq. 5.3. The voltage sensitivity of the MEMS accelerometer is simply the product of the voltage ratio and the sensitivity of the reference accelerometer in the frequency domain. Finally, the charge sensitivity was calculated from the charge amplification (0.1 pC/mV) and the voltage sensitivity.

$$R(\omega) = \frac{V_{MEMS}(\omega)}{V_r(\omega)} = \frac{H_{MEMS}(\omega) \cdot P(\omega)}{H_r(\omega) \cdot P(\omega)} = \frac{H_{MEMS}(\omega)}{H_r(\omega)} \quad (5.3)$$

where $V_{MEMS}(\omega)$, $V_r(\omega)$, $H_{MEMS}(\omega)$, $H_r(\omega)$ are the voltage output and sensitivity for MEMS and reference accelerometers respectively. In addition, the resonant frequency can be obtained through this measurement, if it occurs below 10 kHz.

5.1.3 Tested Results

The frequency responses for different types of accelerometers are shown in *Figures 5.3 to Figure 5.5*. All of them show a flat frequency response from ~250 Hz to their first fundamental resonant frequency, a desirable feature for an accelerometer design. Below 250 Hz, the frequency response shows a roll off. This could be caused by the leakage of piezoelectric charges. This is why piezoelectric-type accelerometers are generally not used for near dc measurements [20]. In *Figure 5.5*, another peak around 40 kHz is observed in the frequency response. It comes from the mode of the metal case used for temporarily packaging the MEMS accelerometer. Hermetic packaging can solve this problem in future iterations. The charge sensitivities were calculated at 1 kHz following the procedure described in the previous section and plotted as a function of the corresponding resonant frequencies in *Figure 5.6*. The frequency variations for each type of accelerometer were caused by variations of the silicon diaphragm thickness. The curve shows that the sensitivity increases with decreasing resonant frequency, in good agreement with the conclusions from Section 3.2.5.

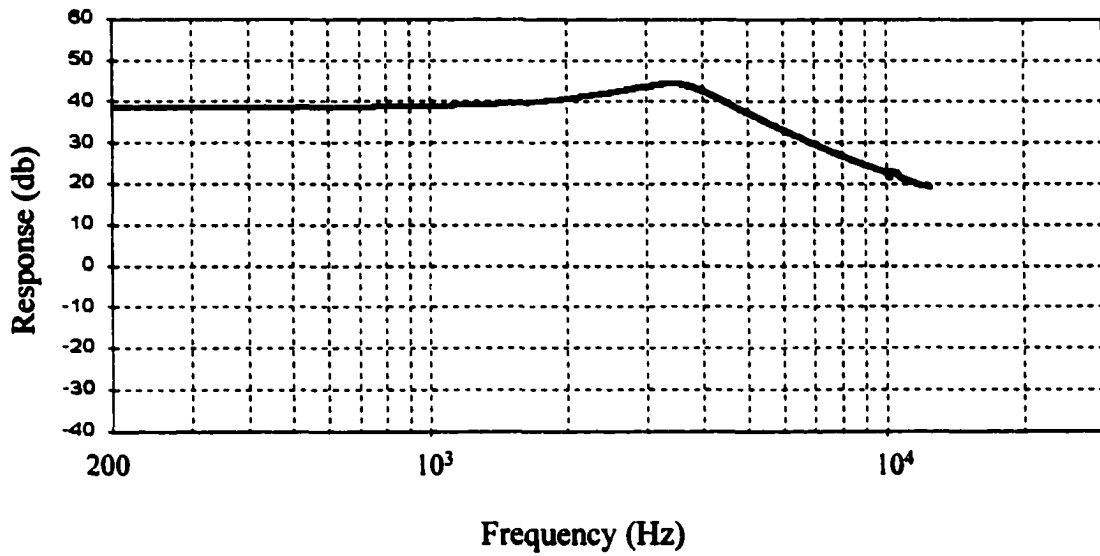


Figure 5.3: Frequency response of the diaphragm-type MEMS accelerometer; the resonant frequency is 3.7 kHz and sensitivity is 7.6 pC/g

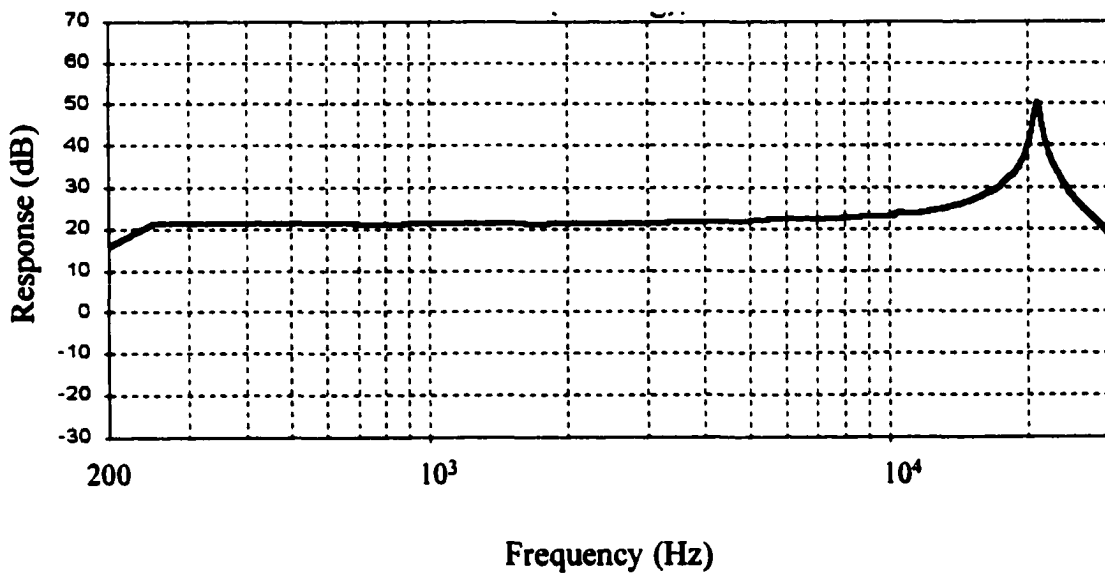


Figure 5.4: Frequency response of the diaphragm type MEMS accelerometer; the resonant frequency is 22.06 kHz and sensitivity is 0.47 pC/g

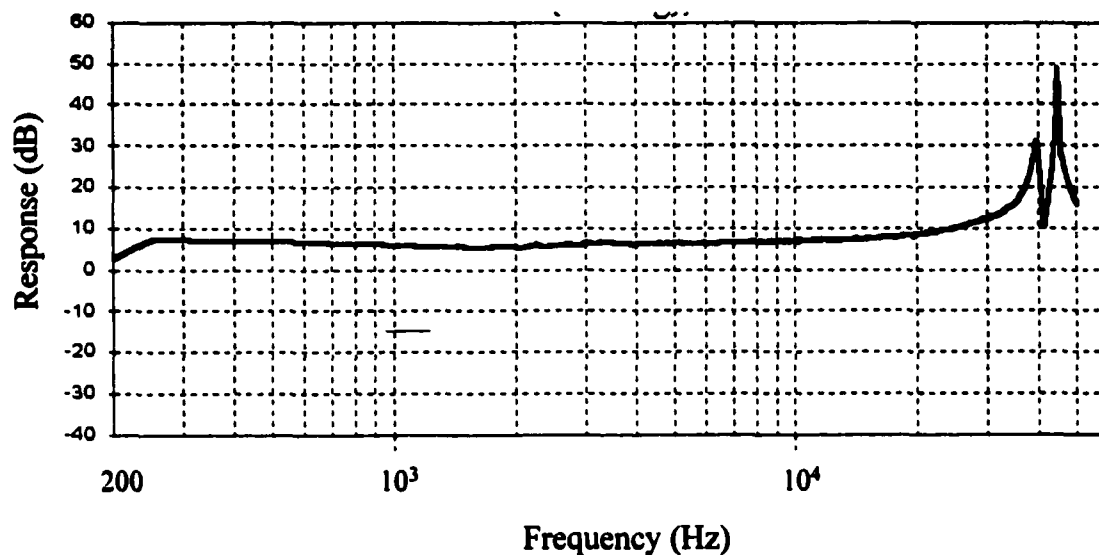


Figure 5.5: Frequency response of the trampoline type MEMS accelerometer; the resonant frequency is 44.3 kHz and sensitivity is 0.10 pC/g

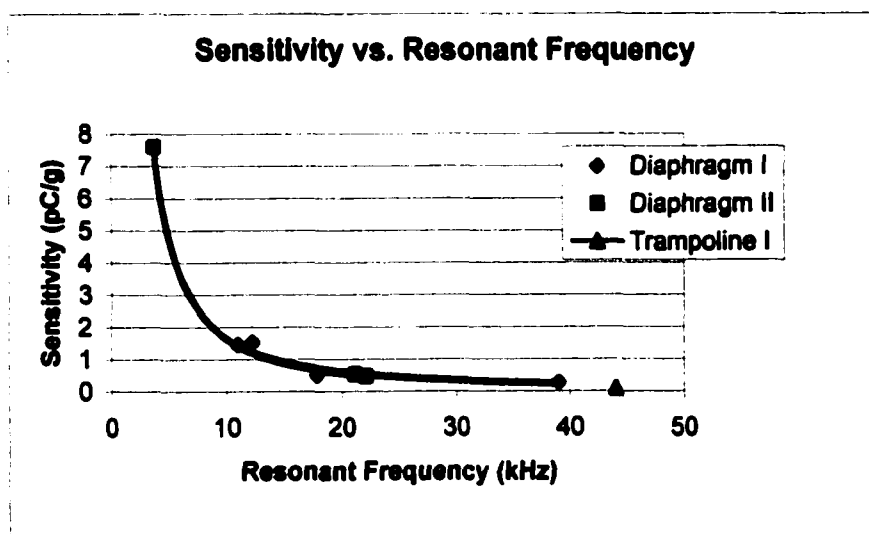


Figure 5.6: Sensitivity vs. resonant frequency for each type of MEMS accelerometer

5.2 Impedance Resonance Measurements

Piezoelectric PZT films can also be excited electrically. Impedance measurements of bulk piezoelectric ceramics are widely used to extract material properties [53]. Here, impedance measurements were used to complement the frequency response measurements of the sensitivity. This was particularly useful when the MEMS accelerometer resonant frequency is higher than that which the shaker can achieve. An impedance analyzer (HP 4194A) was used and the oscillating voltage was set at 0.5 V without DC bias. *Figure 5.7* shows one of the measured impedance curves and the resonant peak is around 12.27 kHz. The measured resonant frequency is in good agreement with that measured from frequency response measurement both at PSU and Wilcoxon Research.

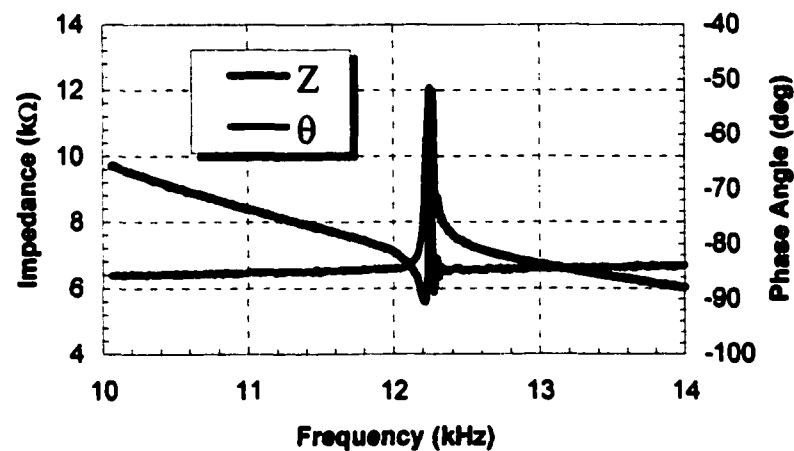


Figure 5.7: The impedance measurement of the diaphragm type MEMS accelerometer showing the resonant peak at 12.27 kHz; Z is the impedance and θ is the phase

5.3 Comparison of Theoretical and Measured Results

5.3.1 Comparison of Analytical and FEA Results

The analytical dynamic models of the cantilever beams and trampoline structures described in Chapters 3 and 4 provide useful information for the accelerometer design. Furthermore, they provide insight into the device physics (such as the relationship between dimensions and material parameters), which are difficult to incorporate explicitly in the FEA model. However, some assumptions in the analytic models affect the accuracy of the predicted results. For example, the resonant frequency of the analytic solution is higher than that calculated from FEA. This is because the proof mass in the analytic model is treated as a mass concentrated at position L (see *Figure 3.4* and *4.3*) instead of a distributed mass; as a result, the equivalent stiffness of the whole structure is higher with this assumption. In contrast, the bending moment generated from the proof mass is smaller with this assumption; as a result, the sensitivity of the analytic model is smaller than that calculated from FEA. From *Table 5.1*, it can be seen that the difference between the analytic and FEA results is smaller for longer beams (both for cantilever and trampoline types). The reason is that the size of the proof mass, which is the same for each type, is relatively close to a concentrated mass for a longer beam.

In summary, it is suggested that the analytic model can be used in prototyping designs, since it provides more insight between design parameters and it results in an acceptable error. However, for detailed evaluations and comparisons, FEA modeling is

recommended. The following section will compare the measured results of the MEMS accelerometers with the FEA results.

Table 5.1: Comparison of analytic and FEA results

Device Type	Resonant Frequency (kHz)		Sensitivity (pC/g)	
	Analytic	FEA	Analytic	FEA
Cantilever I (1.0 mm)	27.5	20.0	0.18	0.27
Cantilever II (1.27 mm)	18.8	14.8	0.31	0.46
Cantilever III (1.8 mm)	10.6	9.3	0.69	0.91
Trampoline I (1.1 mm)	33.2	31.9	0.15	0.23
Trampoline II (1.3 mm)	25.4	24.5	0.23	0.33
Trampoline III (1.7 mm)	16.4	16.0	0.49	0.56
<p>1) The proof mass for the cantilever beam is $300*350*450 \mu\text{m}$ (length*width*thickness)</p> <p>2) The proof mass for the cantilever beam is $800*800*450 \mu\text{m}$ (length*width*thickness)</p>				

5.3.2 Comparison of Measured and FEA Results

Since the thickness of the silicon beam (or diaphragm) deviated from the desired values (40 μm and 60 μm) because of the non-uniform etching rate of the DRIE steps as described in Section 4.3.4, the sensitivity and resonant frequency also differed from the theoretical value as well. In order to have a better comparison, the thickness of the silicon diaphragm corresponding to each measured resonant frequency and device type was calculated. Consequently, the sensitivity corresponding to a particular silicon thickness was calculated (see Table 5.2).

Table 5.2: Comparison of FEA and measured results

Device type	Measured	
	Resonant Frequency (kHz)	Sensitivity (pC/g)
Annular I	11.01	1.45
Annular I	12.27	1.53
Annular I	17.80	0.50
Annular I	39.00	0.27
Annular II	3.70	7.60
Annular II	21.12	0.53
Annular II	22.06	0.47
Trampoline III	44.30	0.1

1. Sensitivity and silicon thickness are calculated corresponding to the measured resonant frequency for each type of devices
2. The Young's modulus and d_{31} of the PZT film used in the calculations were 100 GPa and -45 pC/N

The average measured sensitivity is 36.3% below the FEA value; *Figure 5.8* shows the percent of the measured sensitivity over the FEA sensitivity vs. the resonant frequency. There are several possible reasons for the observed difference between the theoretical and measured sensitivity. First, misalignment of the front-to-backside photolithography can result in the misplacement of the top electrode on the highly stressed area. The measured misalignment according to section 4.3.1 was 20 μm and the top electrode widths of the diaphragm design are 180 μm (outer), 280 μm (inner) and 150 μm (outer), 256 μm (inner) for type I and II designs respectively. Therefore, the error from the misalignment could be around 10% or more. Second, the profile and dimension of the beam or diaphragm were not perfect. For example, the profile of the bottom of the proof mass or frame was convex instead of a perfect square (see *Figure 5.9*). Consequently, the stress distribution on this area, which is the highly stressed area, was not exactly the same as the modeled one. This will affect the accuracy of the sensitivity calculation. Finally, the Young's modulus of the silicon is not isotropic and an average value of 150 GPa was used for the calculation. In summary, the difference between the experimental and theoretical results is acceptable and it shows good control of the material preparation and device fabrication. In the future, the disparity can be reduced with better understanding of the material properties, improved modeling of the real geometry of the accelerometer, and better processing control (DRIE and front-to-backside alignment).

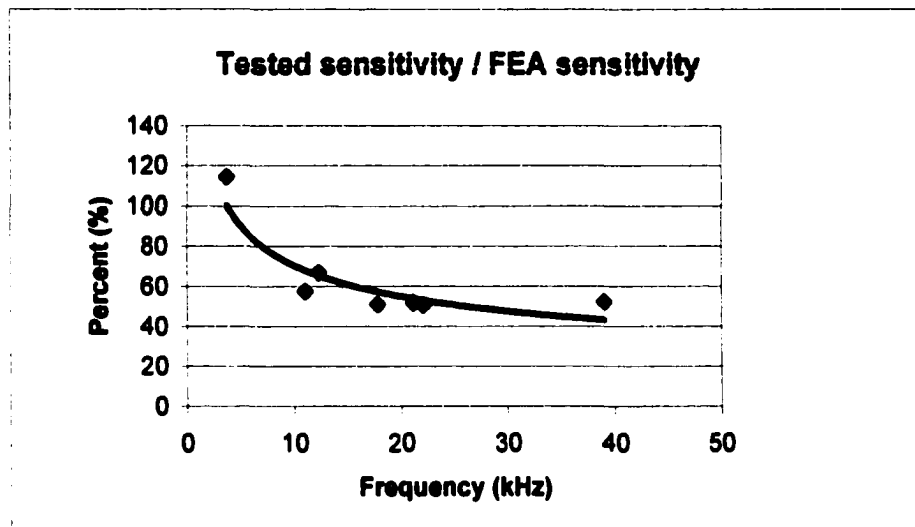


Figure 5.8: The average tested sensitivity is 36.3% below the FEA value

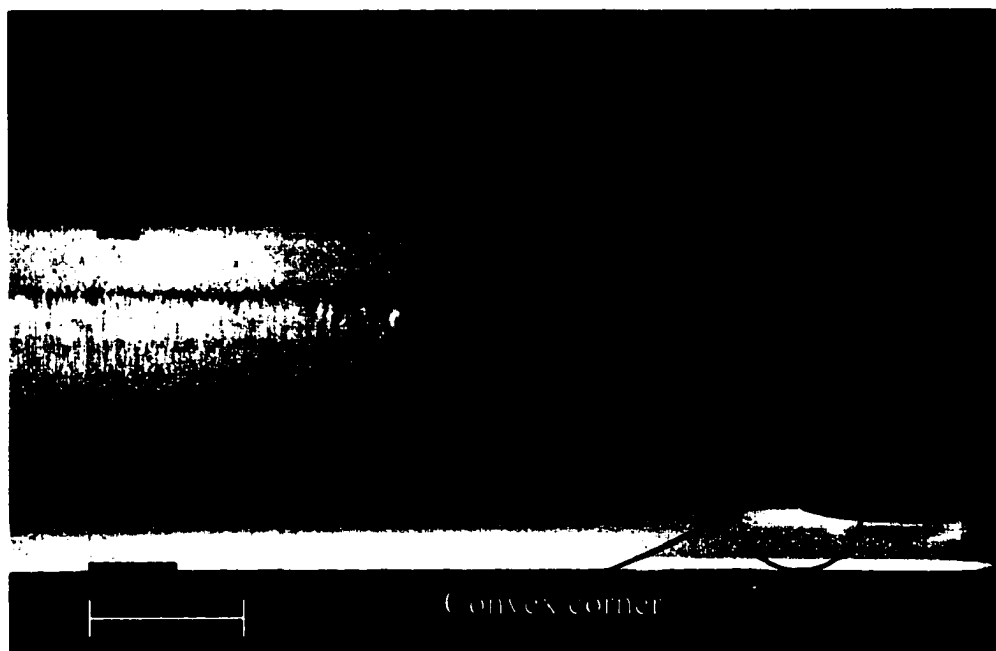


Figure 5.9: Etched profile of the proof mass (diaphragm type) showing an imperfect vertical wall

In the measurement, another important material property of PZT films was also observed. In *Figure 5.8*, the frequency difference for each type of accelerometers was mainly caused by variations of the silicon thickness. Therefore, it can be re-plotted by changing the x-axis from frequency to the corresponding silicon thickness, as shown in *Figure 5.10*. From the figure, the ratio between the measured sensitivity and the FEA calculations is nearly constant (~60%) down to a silicon thickness of ~30 μm , and then starts to increase with decreasing silicon thickness. One possible origin for this behavior would be that the piezoelectric constant starts to increase with decreasing silicon thickness below this point. If so, then the piezoelectric constant at a silicon thickness of 6.1 μm is about two times larger than the average value for the heavily clamped films. This difference is much larger than the point-to-point variations in the piezoelectric coefficient of the film. It is likely that the increase response results from removal of the clamping of the PZT films from the silicon substrate [84]. The clamping effect has not been observed experimentally in the past because of the lack of micromachining techniques to efficiently remove the bulk silicon substrate. Another possibility is that the structure itself deforms due to stress relief, leading to the part behaving more like a shell than a straight diaphragm. Consequently, the stresses may be amplified. Future work to clarify the origin of this behavior should be undertaken. This is a very good initiation for a further detailed study on the clamping effect of PZT films leveraging from the microfabrication processing and testing techniques developed in this work.

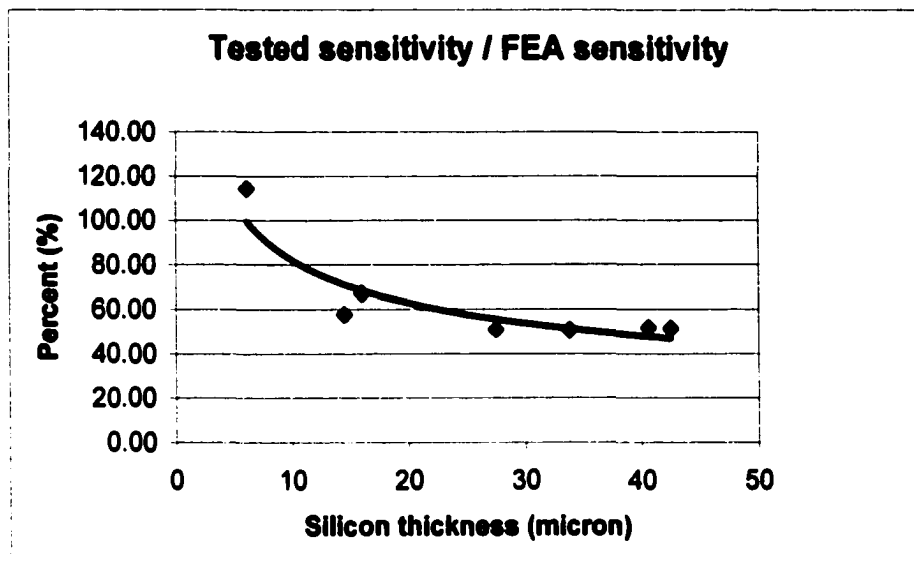


Figure 5.10: The ratio of the measured sensitivities to the theoretical ones plotted as a function of the silicon thickness; the PZT thickness is 5.6 μm

Chapter 6

Conclusions and Future Work

6.1 Conclusions

The major contributions and findings of this research included developing analytical and FEA modeling for piezoelectric accelerometers, developing an appropriate fabrication route for the accelerometers, including the etching of thick PZT films combined with DRIE processing, and comparing the measured sensitivities to the predicted values.

6.1.1 Design and Modeling

Dynamic models of the cantilever and trampoline accelerometers were derived via structural dynamics and the constitutive equations of linear elastic, piezoelectric materials. In addition to the time-dependent transverse vibration equation, the mode shape, resonant frequency and sensitivity of the accelerometers were calculated through these models. These aid in understanding the relationships between the design parameters. Optimization of the thickness of the PZT and silicon beams, which is critical to the sensitivity of the accelerometers, was achieved. It was found that the effects of the structural dynamics, the material properties, and manufacturability issues all need to be

considered to avoid incorrect conclusions. Two approaches to the optimization were demonstrated for different accelerometers specifications.

6.1.2 Fabrication

This work is the first demonstration of fabricating bulk-micromachined accelerometers combining the DRIE releasing strategy and thick piezoelectric PZT films. The processes developed in this research are beneficial for future research on PZT-based MEMS devices. The important processes developed are summarized in the following:

A mechanical jig is demonstrated to provide ease of use and acceptable accuracy ($< 25 \mu\text{m}$) for front-to-backside alignment. Pt(150nm)/Ti(20nm) bottom electrodes sputtered at temperatures of 300–400° C were preferable to electron-gun films evaporated at room temperature, since they provide better adhesion for subsequent high-temperature PZT crystallization steps. For the top electrode, Au/Cr is preferable to Au/Ti, both because Cr provides better adhesion between PZT and Au, and because it shows better resistance to the subsequent PZT etching.

Processes for patterning thick PZT films were developed and characterized. A two-step etching process was developed to pattern thick PZT films. In the first step, 10:1 buffered HF is used to remove the majority of the film at room temperature. However, etching thick PZT films using HF-based solutions forms metal-fluoride residues, which have low solubility. Therefore, a second etching step, 2HCl:H₂O at 45° C, was used to remove these residues. A high etch rate (0.13 $\mu\text{m}/\text{min}$), extremely high selectivity with respect to photoresist, and limited undercutting (2:1 lateral to thickness) were obtained.

Furthermore, no adverse effect on the properties of etched films is found in permittivity, dielectric loss, P-E hysteresis loop, and piezoelectric measurements.

It was found that the etching profile obtained in the DRIE steps is greatly affected by the fraction of the wafer surface exposed to the plasma because of the chemical loading effect. The chemical loading was minimized by designing smaller exposed areas, yielding a near vertical side wall (83°). It was found that the uniformity of the DRIE etching rate can be improved by decreasing the etching rate. The thesis successfully demonstrates the manufacturability of integrating high-performance piezoelectric PZT films with the DRIE releasing technique. This opens a new field for future MEMS technology.

6.1.3 Measurement and Results

It was found that probe testing was not adequate for the piezoelectric-type devices when they were mechanically excited during the measurement. This was because the contact force from the probe generated considerable piezoelectric charge, influencing the test results. Instead, wire-bonding was found to be more appropriate for the MEMS accelerometer measurements.

A comparative test was used to measure the frequency response of the MEMS accelerometer sensitivity. The results demonstrate high sensitivities and broad usable frequency ranges of the piezoelectric-type MEMS accelerometers; the sensitivities range from 0.1 to 7.6 pC/g for resonant frequencies ranging from 44.3 kHz to 3.7 kHz.

Reasonable agreement with the FEA results (~ 36% difference) for sensitivity was obtained.

Finally, the importance of substrate thickness in clamping the piezoelectric response of PZT films was experimentally observed for the first time. It is found that the piezoelectric output for the PZT films started to rise when the silicon thickness was about five times (~30 μm in this case) the PZT thickness (5.6 μm). At a silicon thickness (6.1 μm) about the same as the PZT film thickness, the effective piezoelectric constant was nearly twice as large as the clamped one.

6.2 Future Work

There are a number of scientific and technological issues worthy of future investigation, including changing the accelerometer configuration to maximize the figure of merit, improving the fabrication procedure to increase the uniformity of the accelerometers, using an interlayer electrode to increase the accelerometer sensitivity and using the bulk-micromachining technology to study the material properties of PZT films.

To lower the sensor capacitance, an interdigitated electrode configuration could be used, because in this case the capacitance is decided by the finger spacing instead of the film thickness [85]. In addition, PZT films in this configuration are poled in plane; in other words, the d_{33} mode is applied. This could improve the charge sensitivity, since the d_{33} piezoelectric constant is about twice as large as d_{31} for PZT films. However, the area under the electrodes cannot be poled effectively; as a result, it does not contribute to the

charge output. Therefore, optimization of finger width and spacing is necessary to obtain a low capacitance and high sensitivity for the accelerometer.

Non-uniformity in the etching rate of the DRIE etcher causes variations of the beam and diaphragm thickness across a wafer. This, in turn, causes variations in the sensitivity and resonant frequency. This could be solved using silicon on insulator (SOI) wafers, which have a buried silicon oxide layer between an active silicon layer and the silicon substrate. During the DRIE step, the etch would stop at the silicon oxide layer and the beam and diaphragm thickness would then be precisely controlled as the thickness of the active silicon layer.

As discussed in the section of the optimization of the PZT and silicon beam thickness, the sensitivity increases with decreasing silicon thickness. However, the piezoelectric charge starts to cancel when the neutral axis moves into the PZT layer. To circumvent this, an interlayer electrode could be placed on the neutral axis inside the PZT layer (see *Figure 6.1*). Therefore, the cancellation can be avoided and the sensitivity could be increased to a maximum value with this new electrode design. However, deposition of high-quality PZT thick films on this configuration could be a challenge. In addition, the mechanical strength of the PZT film without a silicon supporting layer could cause a failure problem.

The properties of the PZT films, such as Young's modulus and the unclamped piezoelectric constant, are not yet well understood. Taking advantage of the microfabrication processing and measurement techniques developed in this thesis, they could be studied in detail. A simple structure, such as a cantilever beam or a diaphragm,

would be preferred since available analytical models of these structures would be helpful to extract material properties from the experimental data. The Young's modulus of the PZT film could be calculated from the measured resonant frequency of the structure, after removing the entire silicon layer. The clamped piezoelectric constant as a function of the silicon thickness (or the ratio of the silicon and PZT layers) could be obtained by changing the thickness of the silicon and PZT layers. Based on the measured data, a theoretical model for the clamping effect could be derived.

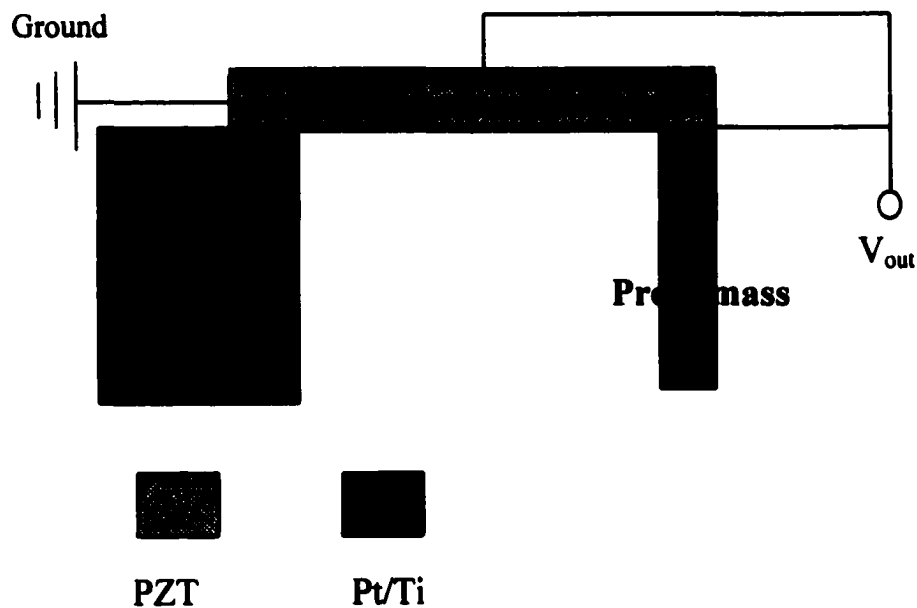


Figure 6.1: Interlayer electrodes for a high-sensitivity accelerometer design

In summary, this thesis demonstrates not only high-performance (high sensitivity and broad bandwidth) MEMS accelerometers, but also opens a new field combining the DRIE technique and piezoelectric PZT films for future MEMS applications.

BIBLIOGRAPHY

1. K. Najafi, "Micromachined Micro Systems: Miniaturization Beyond Microelectronics," *VLSI Circuits, Digest of Technical Papers*, pp. 6-13, 2000
2. M. Pottenger, B. Eyre, E. Kruglick, G. and Lin, "MEMS: The Maturing of a New Technology," *Solid State Technology*, vol. 40, no. 9, pp. 89-96, 1997
3. D. S. Eddy and D. R. Sparks, "Applications of MEMS Technology in Automotive Sensors and Actuators," *Proceedings of The IEEE*, vol. 86, no. 8, pp. 1747-1755, 1998
4. M. Mollendorf, "Micro-Electro-Mechanical-Systems and Industrial Applications," *Proceedings of ASME Aerospace Division*, vol. 52, pp. 761-767, 1996
5. P. Muralt, "Ferroelectric Thin Films for Micro-sensors and Micro-actuators: a Review," *J. Micromech. Microeng.*, vol. 10, pp. 136-146, 2000
6. J. T. Evans and R. Wormack, "An Experimental 512-bit Nonvolatile Memory with Ferroelectric Storage Cell," *IEEE J. Solid-State Circuits*, vol. 23, pp. 1171-1175, 1988
7. S. M. Sze, *Semiconductor Sensors*, John Wiley & Sons, Inc., 1994

8. K. Tani, K. Senda, T. Niikawa, and K. Tazuke, "ZnO Surface Acoustic Wave Filter for TV Set," *National Technical Report (Matsushita Electric Industry Company)*, vol. 24, no. 1, pp. 134-143, 1978
9. C. Lee, T. Itoh, and T. Suga, "Micromachined Piezoelectric Force Sensors Based on PZT Thin Films," *IEEE Transactions on Ultrasonics, Ferroelectrics, and Frequency Control*, vol. 43, no. 4, pp. 553-559, July 1996
10. D. L. Polla, C. Ye, P. Schiller, T. Tamagawa, W. P. Robbins, D. Glumac, and C. C. Hsueh, "Applications of PZT and Related Thin Films in Piezoelectric Microsensors," *Material Research Society Symposium Proceedings*, vol. 243, pp. 55-60, 1992
11. W. Benecke, "Micromechanical Sensors," *CompEuro '89., 'VLSI and Computer Peripherals. VLSI and Microelectronic Applications in Intelligent Peripherals and their Interconnection Networks', Proceedings*, 1989
12. W. P. Robbins, D. L. Polla, T. Tamagawa, D. E. Glumac, and W. Tjhen, "Design of Linear-motion Microactuators Using Piezoelectric Thin Films," *IEEE/ASME, Journal of Microelectromechanical Systems*, vol. 1, pp. 247-252, 1991
13. A. M. Flynn, L. S. Tavrow, S. F. Bart, R. A. Brooks, D. J. Ehrich, K. R. Udayakumar, and L. E. Cross, "Piezoelectric Micromotors for Microrobots," *IEEE/ASME, Journal of Microelectromechanical Systems*, vol. 1, pp. 44-51, 1992

14. J. G. Smits, "Piezoelectric Micropump with Three Valves Working Peristaltically," *Sensors and Actuators*, vol. A21-A23, pp. 203-206, 1990
15. N. Yazdi, F. Ayazi, and K. Najafi, "Micromachined Inertial Sensors," *Proceedings of the IEEE*, vol. 86, no. 8, pp. 1640-1659, 1998
16. L. M. Roylance and J. A. Anbell, "A Batch-fabricated Silicon Accelerometer," *IEEE Transactions of Electronic Devices*, vol. ED-26, no. 12, pp. 1911-1917, 1979
17. P. W. Barth, F. Pourahmadi, R. Mayer, J. Poydock, and K. Petersen, "A Monolithic Silicon Accelerometer with Integral Air Damping and Overrange Protection," *Tech. Dig. Solid-state Sensors and Actuators Workshop*, pp. 122-125, 1992
18. C. Song, B. Ha, and S. Lee, "Micromachined Inertial Sensors," *Proceedings of the 1999 IEEE/RSJ, International Conference on Intelligent Robots and Systems*, vol. 2, pp. 1049-1056, 1999
19. P. L. Chen, R. S. Muller, R. D. Jolly, G. L. Halac, R. D. White, A. P. Andrews, T. C. Lim, and M. E. Motamedi, "Integrated Silicon Microbeam PI-FET Accelerometer," *IEEE Transactions of Electronic Devices*, vol. ED-29, no. 1, pp. 27-33, 1982
20. P. L. Chen and R. S. Muller, "Integrated Silicon Pi-FET Accelerometer with Proof Mass," *Sensor and Actuators*, vol. 5, pp. 119-126, 1984

21. D. L. DeVoe and A. P. Pisano, "A Fully Surface-Micromachined Piezoelectric Accelerometer," *IEEE International Conference on Solid-State Sensors and Actuators*, vol. 2, pp. 1025-1028, 1997
22. R. de Reus, J. O. Gullov, and P. R. Scheeper, "Fabrication and Characterization of a Piezoelectric Accelerometer," *J. Micromech. Microeng.*, vol. 9, pp. 123-126, 1999
23. P. Scheeper, J. O. Gullov, and L. M. Kofoed, "A Piezoelectric Triaxial Accelerometer," *J. Micromech. Microeng.*, vol. 6, pp. 131-133, 1996
24. Y. Nemirovsky, A. Nemirovsky, P. Murali, and N. Setter, "Design of a Novel Thin-film Piezoelectric Accelerometer," *Sensors and Actuators*, vol. A56, pp. 239-249, 1996
25. J. H. Kim, L. Wang, S. M. Zurn, L. Li, Y. S. Yoon, and D. L. Polla, "Fabrication Process of PZT Piezoelectric Cantilever Unimorphs Using Surface Micromachining," *Integrated Ferroelectrics*, vol. 15, pp. 325-332, 1997
26. D. Eichner, M. Giousouf, and W. von Munch, "Measurements on Micromachined Silicon Accelerometers with Piezoelectric Sensor Action," *Sensors and Actuators*, vol. A76, pp. 247-252, 1999
27. S. P. Beeby, N. Ross, and N. M. White, "Thick Film PZT/Micromachined Silicon Accelerometer," *IEEE Electronics Letters*, vol. 35, no. 23, pp. 2060-2062, 1999

28. S. P. Beeby, N. Ross, and N. M. White, "Design and Fabrication of a Micromachined Silicon Accelerometer With Thick-film PZT Sensors," *J. Micromech. Microeng.*, vol. 10, p. 322-328, 2000
29. P. J. French and P. M. Sarro, "Surface versus Bulk Micromachining: the Contest for Suitable Applications," *J. Micromech. Microeng.*, vol. 8, pp. 45-53, 1998
30. T. B. Gabrielson, "Fundamental Noise Limits for Miniature Acoustic and Vibration Sensors," *J. Vibration and Acoustics*, vol. 117, pp. 405-410, 1995
31. H. R. Robbins and B. Schwartz, "Chemical Etching of Silicon – I. The System HF, HNO₃, H₂O, and HC₂C₃O₂," *J. Electrochem. Soc.*, vol. 106, no. 6, pp. 505-508, 1959
32. H. R. Robbins and B. Schwartz, "Chemical Etching of Silicon – II. The System HF, HNO₃, H₂O, and HC₂C₃O₂," *J. Electrochem. Soc.*, vol. 107, no. 2, pp. 108-111, 1960
33. G. T. A. Kovacs, N. I. Maluf, and K. E. Petersen, "Bulk Micromachining of Silicon," *Proceedings of the IEEE*, vol. 86, no. 8, pp 1536-1551, 1998
34. H. Seidel, "The Mechanism of Anisotropic Silicon Etching and Its Relevance for Micromachining," *Proc. Transducers '87, Rec. 4th Int. Conf. Solid-state Sensors and Actuators*, pp. 120-125, 1987

35. H. Seidel, L. Csepregi, A. Heuberger, and H. Baumgartel, "Anisotropic Etching of Crystalline Silicon in Alkaline Solutions I: Orientation Dependence and Behavior of Passivation Layers," *J. Electrochem. Soc.*, vol. 137, no. 11, pp. 3612-3626, 1990
36. R. M. Finne and D. L. Klein, "A Water-amine Complexing Agent System for Etching in Silicon," *J. Electrochem. Soc.*, vol. 114, no. 9, pp. 965-970, 1967
37. A. Reisman, M. Berkenblit, S. A. Chan, F. B. Kaufmann, and D. C. Green, "The Controlled Etching of Silicon in Catalyzed Ethylene-diamine-pyrocatechol-water Solutions," *J. Electrochem. Soc.: Solid-State Sci. Technol.*, vol. 126, no. 8, pp. 1406-1415, 1979
38. K. E. Petersen, "Silicon as a Mechanical Material," *Proceedings of the IEEE*, vol. 70, pp. 42-457, 1982
39. O. Tabata, R. Asahi, H. Funabashi, K. Shimaoka, and S. Sugiyama, "Anisotropic Etching of Silicon in TMAH Solutions," *Sensors and Actuators A*, vol. 34, no. 1, pp. 51-57, 1992
40. A. Merlos, M. Acero, M. H. Bao, J. Bausells, and J. Esteve, "TMAH/IPA Anisotropic Etching Characteristics," *Sensors and Actuators*, vol. A37-38, pp. 737-743, 1993

41. Q. Zhang, L. Litian, and Z. Li, "A New Approach to Convex Corner Compensation for Anisotropic Etching of (100) Si in KOH," *Sensors and Actuators*, vol. A56, pp. 251-254, 1996
42. B. Puers and W. Sansen, "Compensation of Structures for Convex Corner Micromachining in Silicon," *Sensors and Actuators*, vol. 23, no. 1-3, pp. 1036-1041, 1990
43. R. P. van Kampen and R. D. F. Wolffenbuttel, "Effects of <110>-oriented Corner Compensation Structures on Membrane Quality and Convex Corner Integrity in (100)-silicon Using Aqueous KOH," *J. Micromech. Microeng.*, vol. 5, no. 2, pp. 91-94, 1995
44. K. Murakami, Y. Wakabayashi, K. Minami, and M. Esashi, "Cryogenic Dry Etching for High Aspect Ratio Microstructures," *Proceedings of IEEE Microelectromechanical Systems Conference*, pp. 65-70, 1995
45. M. Esashi, M. Takinami, Y. Wakabayashi, and K. Minami, "High-rate Directional Deep Dry Etching for Bulk Silicon Micromachining," *J. Micromech. Microeng.*, vol. 5, no. 1, pp. 5-10, 1995
46. F. Larmar and P. Schilp, "Method of Anisotropic Etching Silicon," *German Patent DE 4241045*, 1994

47. K. A. Shaw, Z. L. Zhang, and N. C. MacDonald, "SCREAM I: A Single Mask Single-crystal Silicon Process for Microelectromechanical Structures," *Proc. 1993 Micro Electro Mechanical Systems Workshop*, pp. 155-160, 1993
48. W. Hofmann and N. C. MacDonald, "Fabrication of Multiple-level Electrically Isolated High-aspect-ratio Single Crystal Silicon Microstructures," *Proc. 10th Ann. Workshop Micro Electro Mechanical Systems*, pp. 460-464, 1997
49. G. K. Fedder, S. Santhanam, M. L. Reed, S. C. Eagle, D. F. Guillou, M. S.-C. Lu, and L. R. Carley, "Laminated High-aspect-ratio Microstructures in a Conventional CMOS Process," *Sensors Actuators*, vol. A57, no. 2, pp. 103-110, 1997
50. L. A. Shuvalov, *J. Phys. Soc. Jpn.*, vol. 38, 1970
51. W. D. Kingery, H. K. Bowen, and D. R. Uhlmann, *Introduction to Ceramics, Second Edition*, John Wiley and Sons, New York, 1976
52. F. Jona and G. Shirane, *Ferroelectric Crystals*, The Macmillan Company, New York, 1962
53. A. J. Moulson and J. M. Herbert, *Electroceramics: Materials, Properties, Applications*, Chapman and Hall, New York, 1990
54. B. Jaffe, J. W. R. Cook, and H. Jaffe, *Piezoelectric Ceramics*, Academic Press, New York, 1971

55. F. Xu, "Longitudinal Piezoelectric Characterization and Domain Wall Contributions in Lead Zirconate Titanate Thin Films," *Ph. D. Thesis, The Pennsylvania University*, 1999
56. ANSI/IEEE 176-1987, *IEEE Standard on Piezoelectricity*
57. D. F. Stout, *Handbook of Operational Amplifier Circuit Design*, McGraw-Hill, Inc., 1976
58. Q. M. Zhang, H. Wang, N. Kim, and L. E. Cross, "Direct Evaluation of Domain-wall and Intrinsic Contributions to the Dielectric and Piezoelectric Response and Their Temperature Dependence on Lead Zirconate Titanate Ceramics," *J. Applied Physics*, vol. 75, no. 1, pp. 454, 1994
59. A. Oikawa and K. Toda, "Preparation of $\text{Pb}(\text{Zr},\text{Ti})\text{O}_3$ Thin Films by an Electron Beam Evaporation Technique," *Applied Physics Letter*, vol. 29, pp. 491, 1976
60. A. Oikawa, "Some Electrical and Optical Properties of Ferroelectric Lead-zirconate-lead-titanate Thin Films," *Journal of Applied Physics*, vol. 48, pp. 2905, 1977
61. R. N. Castellano and L. G. Feinstein, "Ion-beam Deposition of Thin Films of Ferroelectric Lead-zirconate-titanate (PZT)," *Journal of Applied Physics*, vol. 50, pp. 4406, 1979

62. M. Odada, et al., "Preparation of c-axis Oriented PbTiO₃ Thin Film by MOCVD," *Journal of Applied Physics*, vol. 28, p1030, 1989
63. G. Yi, Z. Wu, and M. Sayer, "Preparation of PZT Thin Film by Sol-gel Processing: Electrical, Optical, and Electro-optic properties," *Journal of Applied Physics*, vol. 64, no. 5, 1989
64. D. Roy, S. B. Krupanidhi, and J. Dougherty, "Excimer Laser Ablated Laser Lead Zirconate Titanate Thin Films," *Journal of Applied Physics*, vol. 69, p1, 1991
65. M. Hendrickson, T. Su, S. Trolier-McKinstry, B. J. Rod, and R. J. Zeto, "Processing of PZT Piezoelectric Thin Films for Microelectromechanical Systems," *10th IEEE International Symposium on Applications of Ferroelectrics*, Part 2, vol. 2, pp. 683-686, 1996
66. Q. Zhou, F. Hong, R. Wolf, and S. Trolier-McKinstry, "Dielectric and Piezoelectric Properties of PZT 52/48 Thick Films with (100) and Random Crystallographic Orientation," *Material Research Society Symposium Proceedings*, 2000 Fall Meeting (in press)
67. H. D. Chen, K. R. Udayakumar, L. E. Cross, J. J. Bernstein, and L. C. Niles, "Development and Electrical Characterization of Lead Zirconate Titanate Thick Films on Silicon Substrates," *IEEE International Symposium on Applications of Ferroelectrics*, pp. 495-498, 1994

68. S. Trolier-McKinstry, P. Aungkavattana, F. Chu, J. Lacey, J.-P. Maria, J. F. Shepard, Jr., T. Su, and F. Xu, "Impact of Domains on the Dielectric and Electromechanical Properties of Ferroelectric Thin Films," *Material Research Society Symposium Proceedings Ferroelectric Thin Films VI*, vol. 493, pp. 59-68, 1998
69. K. Saito, J. H. Choi, T. Fukuda, and M. Ohue, "Reactive Ion Etching of Sputtered $\text{PbZr}_{1-x}\text{Ti}_x\text{O}_3$," *Japanese Journal of Applied Physics*, vol. 31, pp. 1260-1262, 1992
70. D. P. Vijay, S. B. Desu, and W. Pei, "Reactive Ion Etching of $\text{PbZr}_x\text{Ti}_{1-x}\text{O}_3$ and RuO_2 Thin Films," *Materials Research Society Symposium Proceedings*, vol. 310, pp.133-138, 1993
71. C. J. Kim, J. K. Lee, C. W. Chung, and I. Chung, "Etching Effects to PZT Capacitors With RuO_2/Pt Electrode by Using Inductively Coupled Plasma," *Integrated Ferroelectrics Proceedings of Technology*, vol. 16, no. 1-4, pp. 149-157, 1997
72. S. Yokoyama, Y. Ito, K. Ishihara, K. Hamada, S. Ohnishi, J. Kudo, and K. Sakityama, "High-temperature Etching of PZT/Pt/TiN Structure by High-Density ECR Plasma," *Japanese Journal of Applied Physics*, vol. 34, 1995
73. J. J. Van Glabbeek, G. A. C. M. Spierings, M. J. E. Ulenaers, G. J. M. Dormans, and P. K. Larsen, "Reactive Ion Etching of $\text{Pt}/\text{PbZr}_x\text{Ti}_{1-x}\text{O}_3/\text{Pt}$ Integrated

- Ferroelectric Capacitors," *Materials Research Society Symposium Proceedings*, vol. 310, p127-132, 1993
74. S. Wolf and R. N. Tuber, *Silicon Processing for the VLSI Era, Volume 1-Process Technology*, Lattice Press, Sunset Beach, CA, 1986
75. R. H. Collins and F. T. Deverse, *US Patent No. 3549368*, 1970
76. S. E. Trolrier, "Use of Photolithography and Chemical Etching in the Preparation of Miniature Piezoelectric Devices from Lead Zirconate Titanate (PZT) Ceramics," *M.S. Thesis, The Pennsylvania University*, 1987
77. J. F. Shepard, P. J. Moses, and S. Trolrier-McKinstry, "The Wafer Flexure Technique For the Determination of the Transverse Piezoelectric Coefficient (d_{31}) of PZT Thin Films," *Sensors and Actuators*, vol. A71, pp. 133-138, 1998
78. J.-P. Maria, "Epitaxial $\text{Pb}(\text{Mg}_{1/3}\text{Nb}_{2/3})\text{O}_3\text{-PbTiO}_3$ Thin Films," *Ph. D. Thesis, The Pennsylvania University*, 1998
79. W. T. Thomson, *Theory of Vibration with Applications, 5th editions*, Prentice-Hall, Inc., Upper Saddle River, NJ, 1998
80. J. L. Humar, *Dynamics of Structures*, Prentice-Hall, Inc., Englewood Cliffs, NJ, 1990

81. A. A. Ayon, R. Braff, C. C. Lin, H. H. Sawin, and M. A. Schmidt, "Characterization of a Time Multiplexed Inductively Coupled Plasma Etcher," *Journal of The Electrochemical Society*, vol. 146, no. 1, p. 339-349, 1999
82. M. A. Lieberman and A. J. Lichtenberg, *Principles of Plasma Discharges and Materials Processing*, John Wiley and Sons, New York, NY, 1994
83. D. L. Smith, *Thin-film Deposition: Principles and Practice*, McGraw-Hill, Inc., New York, NY, 1995
84. K. Lefki and G. J. M. Dormans, "Measurement of Piezoelectric Coefficients of Ferroelectric Thin Films," *Journal of Applied Physics*, vol. 76, no. 3, pp. 1764-1767, 1994
85. Ph. Luginbuhl, S. D. Collins, G.-A. Racine, M.-A. Gretillat, and N. F. de Rooij, "Flexural-Plate-Wave Actuators Based on PZT Thin Film," *Proceedings of the IEEE Micro Electro Mechanical Systems (MEMS)*, pp. 327-332, 1997

VITA

Li-Peng Wang was born in 1969 in Taipei, Taiwan. He graduated from the Chung-Yuan Christian University of Mechanical Engineering in 1992 with a B.S. degree. He received his M.S. in Mechanical Engineering from The Pennsylvania State University in 1997 and began his PhD study in Engineering Science and Mechanics in 1997. His research is mainly on Microelectromechanical Systems (MEMS).